ACS Energy LETTERS

http://pubs.acs.org/journal/aelccp

REVIEW

Photoelectrochemical Conversion of Carbon Dioxide (CO_2) into Fuels and Value-Added Products

Vignesh Kumaravel,* John Bartlett, and Suresh C. Pillai*

Cite This: *ACS Energy Lett.* 2020, 5, 486−519

Read Online

ACCESS | Metrics & More | Article Recommendations | Supporting Information

ABSTRACT: The conversion of carbon dioxide (CO_2) into fuels and value-added products is one of the most significant inventions to address the global warming and energy needs. Photoelectrochemical (PEC) CO_2 conversion can be considered as an artificial photosynthesis technique that produces formate, formaldehyde, formic acid, methane, methanol, ethanol, etc. Recent advances in electrode materials, mechanisms, kinetics, thermodynamics, and reactor designs of PEC CO_2 conversion have been comprehensively reviewed in this article. The adsorption and activation of CO_2/intermediates at the electrode surface are the key steps for improving the kinetics of CO_2 conversion. PEC efficiency could be upgraded through the utilization of 2D/3D materials, plasmonic metals, carbon-based catalysts, porous nanostructures, metal−organic frameworks, molecular catalysts, and biological molecules. The defect engineered (by cation/anion vacancy, crystal distortion, pits, and creation of oxygen vacancies) 2D/3D materials, Z-scheme heterojunctions, bioelectrodes, and tandem photovoltaic−PEC reactors are suitable options to enhance the efficiency at low external bias.

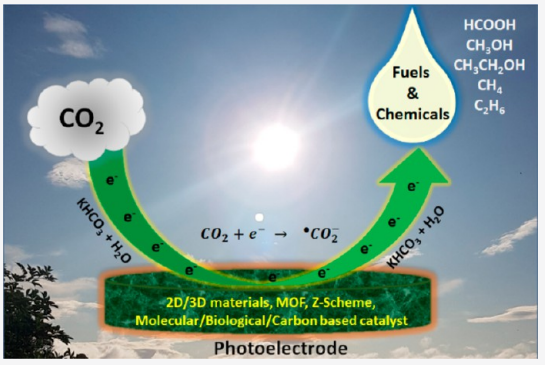

Global warming, which results mainly from increased levels of atmospheric carbon dioxide (CO_2), is one of the critical problems to emerge in recent years.[1−4] A large amount of CO_2 is released into the atmosphere every day in various ways, especially from the burning of fossil fuels. Dependence on fossil fuels not only intensifies the overuse of natural resources but also interrupts the carbon cycle.[5−7] Plants convert CO_2 into carbohydrates to maintain the carbon cycle by a process called photosynthesis, but this is significantly affected by the excess use of fossil fuels, deforestation, industrialization, and urbanization.[8−10] According to some projections, anthropogenic CO_2 levels could reach ∼590 ppm by the year 2100, leading to an increase in the global temperature of 1.9 °C.[11] Most significantly, the temperature increase in the polar regions would be 3 times greater than that in other parts;[7] this could severely impact the survival of all living beings on earth. The Paris agreement, which emerged from studies produced by the Intergovernmental Panel on Climate Change (IPCC), is intended to abate the net atmospheric CO_2 levels by 2050.[12−14] To address this, most countries have been taking numerous actions to develop renewable and sustainable energy production technologies.[15] CO_2 capture and utilization is a prime focus of research for the scientific community in recent years.[16−21] Various research efforts have been established for capturing and sequestration of excess CO_2.[22−25] The possibility of CO_2 leakage, high energy input, and complicated designs are major practical constraints of these methods.[7] Consequently, the recycling or conversion of CO_2 into fuels and other value-added products is an attractive option to address the global warming and energy crisis without impeding development and urbanization.[26−37]

Conversion of CO_2 is scientifically a challenging task, but it has significant benefits. Photoelectrochemical (PEC),[38−42] photocatalysis,[43−48] electrocatalysis,[49−55] thermocatalysis,[56−61] radiolysis,[62−64] and biochemical[65−71] techniques have previously been utilized for CO_2 conversion. Among them, PEC is identified as the ideal method to convert CO_2 into selective gaseous (e.g., methane, ethane, etc.) and liquid products (e.g., formate, methanol, ethanol, etc.) under solar light irradiation, especially for liquid products at ambient temperature and pressure.[72−80] This technology is also called artificial photosynthesis because it mimics nature's energy cycle.[81−86] PEC

Received: November 27, 2019
Accepted: January 8, 2020
Published: January 8, 2020

https://dx.doi.org/10.1021/acsenergylett.9b02585
ACS Energy Lett. 2020, 5, 486−519

has some key benefits such as economic feasibility, control of product selectivity, and environmental compatibility along with the use of renewable solar energy.[87−91] CO_2 is a linear and chemically stable molecule with poor electron affinity, and its conversion reaction is determined by the nucleophilic attacks at the carbon atom.[87] The dissociation energy for breaking the C═O bond is higher than 750 kJ/mol.[92] It is thermodynamically an uphill reaction, and therefore, a higher energy input is necessary to overcome the resistance loss and overvoltage potential, to break the C═O bond, and to form band bending (required process for the separation of photogenerated electron hole pairs).[93] In natural photosynthesis, energy is captured from sunlight by the photosensitizers (e.g., chlorophyll) to perform the endothermic reactions. In the case of PEC CO_2 conversion, the endothermic reactions are driven by electricity and light irradiation. For feasible CO_2 conversion, the energy level of photogenerated electrons and holes should be higher than the overpotential of H_2O/O_2 (0.82 V vs NHE at pH 7) and lower than the overpotential of CO_2/HCOOH (−0.61 V vs NHE at pH 7), respectively.[72,94,95] Photocatalysts with wide-band-gap energy of at least 2.88 eV are essential to perform redox reactions such as water oxidation and CO_2 reduction.[96] The product yield of CO_2 conversion is governed by the choice of electrode materials and electrolytes.[97] The schematic of PEC CO_2 conversion using inexhaustible solar energy is depicted in Figure 1.[98]

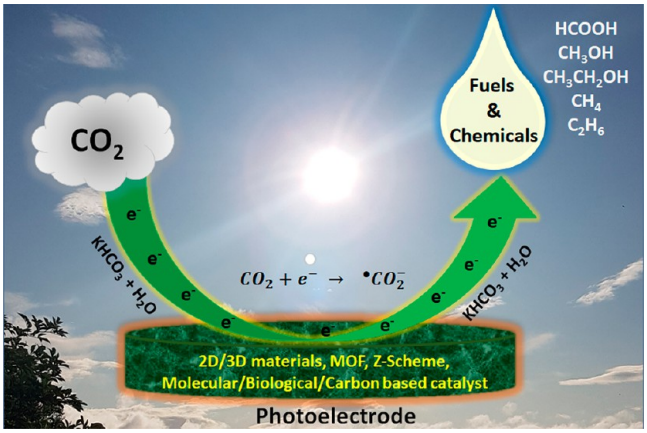

Figure 1. Schematic of the PEC CO_2 conversion into fuels and value-added products under solar light irradiation.

The significance of CO_2 conversion was previously reviewed from various perspectives such as theoretical insights,[90] molecular catalysts,[99−102] layered double hydroxide (LDH) materials,[103] dye-sensitized PEC reactors,[104] electrolyte/electrode/reactor design,[92,97,105−108] surface reactions at the catalyst,[109] methanol production,[93,110] the role of nanomaterials,[111,112] commercialized processes,[113] mechanisms,[114] metal-based catalysts,[115] metal complex/semiconductor hybrids,[116,117] development of organic mediators (ionic liquids, esters, nitriles, etc.),[118] plasmonic nanoparticles,[119,120] 2D materials,[121,122] and silicon materials.[123] Nevertheless, there are no detailed reports on the kinetics of CO_2 conversion. This Review discusses all of the prime features of this technology, such as the mechanism, efficiency calculation, kinetics, reactor design, recent advances, applications of 2D/3D materials, and future challenges. The main intent is to review the key progress of this technology in recent years to support future development of CO_2 conversion.

Mechanism: The important reactions that occur in natural and artificial photosynthesis of CO_2 conversion are schematically shown in Figure 2.[124]

The electrode material immerses into the electrolyte solution during the PEC CO_2 conversion. The electron transfer reactions occur when the Fermi level (E_F) of the electrode material or semiconductor is not equal to that of the electrolyte.[90,107] The reactions transpire at the electrode/electrolyte interface to reduce the E_F difference between the electrode and the electrolyte, suggesting changes in the band diagram or band bending. E_F of an electrolyte is governed by its concentration. The electron transfer occurs at the interface until the E_F levels are equal. For the PEC reactions, p-type semiconductors perform as photocathodes, whereas n-type semiconductors function as anodes. Under light irradiation, electrons and holes are created in the semiconductor at the conduction band (CB) and valence band (VB), respectively. Electrons and holes are the majority carriers for n-type (E_F is located near the CB) and p-type (E_F is situated just above the VB), respectively. Thus, upward and downward band bending could occur at the interface for n-type and p-type, respectively. The band bending phenomenon is essential to separate the photogenerated electrons and holes at the electrode−electrolyte interface to enhance the CO_2 conversion efficiency. The band bending phenomena in a p-type semiconductor for electrocatalytic and PEC CO_2 conversion are shown in Figure 3.[107]

PEC CO_2 conversion in water proceeds through the following reactions (e^-/H^+ transfer, C−O bond breaking, and C−H bond formation).

$$2H_2O_{(l)} \rightarrow O_{2(g)} + 4H^+_{(aq)} + 4e^- \qquad E^\circ_{OX} = -1.23\ V \tag{1}$$

$$CO_{2(aq)} + e^- \rightarrow CO^-_{2(aq)} \qquad E^\circ_{red} = -1.65\ V \tag{2}$$

Reaction of water with holes:

$$H_2O + h^+ \rightarrow {}^\bullet OH + H^+ \tag{3}$$

$$2H_2O + 2h^+ \rightarrow H_2O_2 + 2H^+ \tag{4}$$

$$2H_2O + 4h^+ \rightarrow 4H^+ + O_2 \tag{5}$$

Hydrogen radical formation:

$$H^+ + e^- \rightarrow {}^\bullet H \tag{6}$$

CO_2 anion radical formation:

$$CO_2 + e^- \rightarrow {}^\bullet CO_2^- \qquad E^\circ = -1.9\ V \tag{7}$$

CH_4 formation:

$$CO_2 + 8H^+ + 8e^- \rightarrow CH_4 + 2H_2O \qquad E^\circ = -0.24\ V \tag{8}$$

CH_3OH formation:

$$CO_2 + 6H^+ + 6e^- \rightarrow CH_3OH + H_2O \qquad E^\circ = -0.38\ V \tag{9}$$

https://dx.doi.org/10.1021/acsenergylett.9b02585
ACS Energy Lett. 2020, 5, 486−519

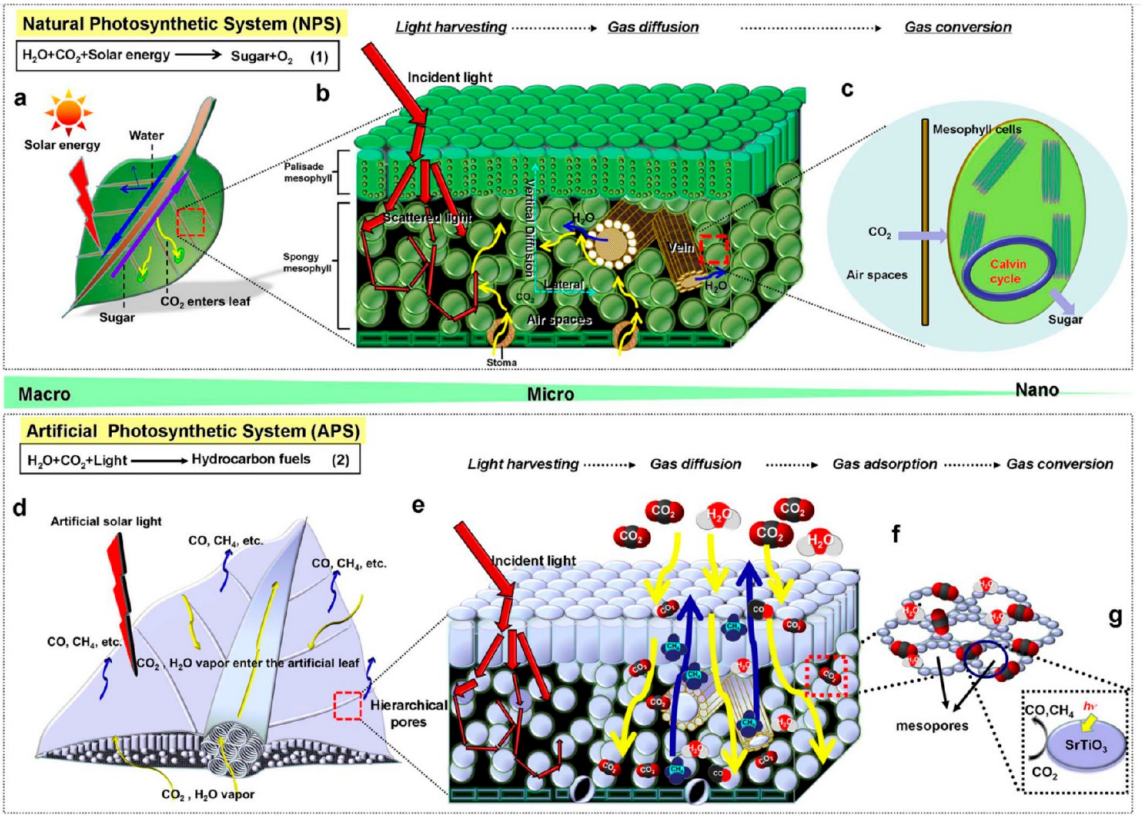

Figure 2. Schematic representation of the crucial reactions involved in CO_2 conversion, natural photosynthesis and artificial photosynthesis: (a,d) basic principle at the macroscale; (b,e) light absorption and gas diffusion phenomena at the microscale; (f) CO_2 adsorption at nanoscale only in the artificial photosynthesis; and (c,g) conversion of CO_2 at the nanoscale.[124] Reproduced with permission from ref 124. Copyright (2013), Springer Nature.

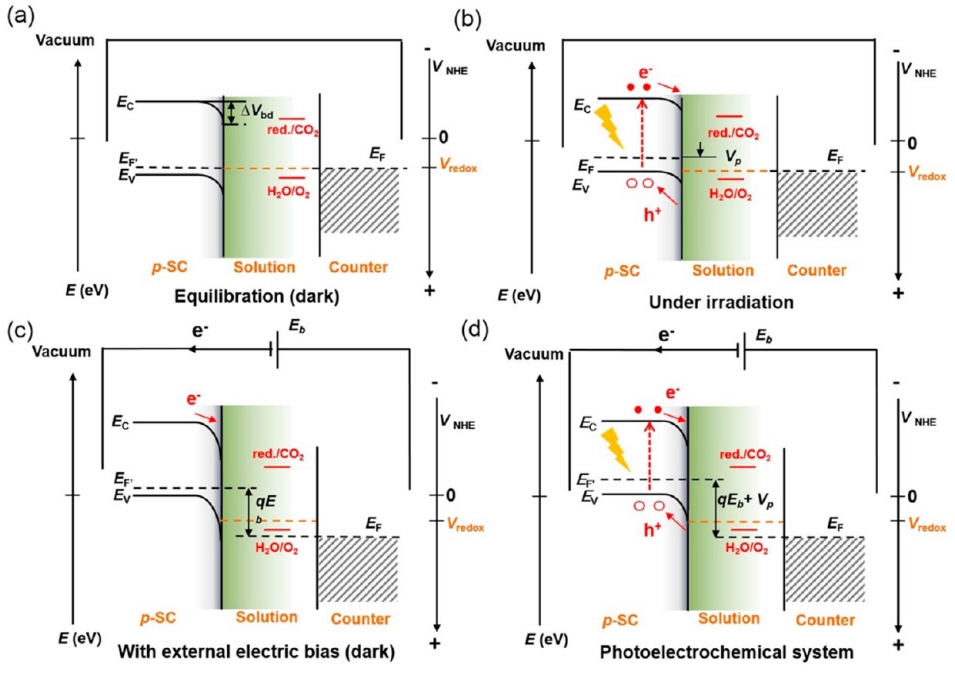

Figure 3. Schematic of band bending phenomena and electron transfer reactions in a p-type semiconductor (p-SC) for CO_2 conversion: (a) at equilibrium in the dark, (b) under light irradiation, (c) electrocatalysis, and (d) PEC.[107] Reproduced with permission from ref 107. Copyright (2018), John Wiley and Sons.

https://dx.doi.org/10.1021/acsenergylett.9b02585
ACS Energy Lett. 2020, 5, 486−519

CO formation:

$$CO_2 + 2H^+ + 2e^- \rightarrow CO + H_2O \qquad E^\circ = -0.53\ V \tag{10}$$

HCOOH formation:

$$CO_2 + 2H^+ + 2e^- \rightarrow HCOOH \qquad E^\circ = -0.61\ V \tag{11}$$

HCHO formation:

$$CO_2 + 4H^+ + 4e^- \rightarrow HCHO + H_2O \qquad E^\circ = -0.48\ V \tag{12}$$

CH_3CH_2OH formation:

$$2CO_2 + 12H^+ + 12e^- \rightarrow CH_3CH_2OH + 3H_2O \qquad E^\circ = 0.08\ V \tag{13}$$

The electrochemical (EC) reduction potential values (E°) are associated with the standard hydrogen electrode (SHE) at pH 7.[90,97] Equations 8−eq 13 clearly show that both protons and electrons are involved in chemical reactions to form various products from the $CO_2^{\bullet-}$ intermediate. This is called proton coupled electron transfer reactions.[97] During the PEC process, CO_2 could be converted into carbon monoxide (CO), formaldehyde (HCHO), formic acid (HCOOH), methanol (CH_3OH), ethanol (CH_3CH_2OH), isopropanol ($CH_3CH(OH)CH_3$), methane (CH_4), etc. through the proton coupled electron transfer pathways. CO_2 conversion could be influenced by the effect of temperature. The efficiency of CH_4, CH_3OH, and CH_3CH_2OH production decreases with the increase of temperature.[114] At the same time, the increase of temperature has a positive effect on the production of HCHO and HCOOH.[114]

$$\Delta G^\theta = -RT \ln K_f^\theta \tag{14}$$

$$\left(\frac{\partial \ln K_f^\theta}{\partial T}\right)_P = \frac{\Delta H^\theta}{RT^2} \tag{15}$$

The conversion of CO_2 to CO or formate is kinetically feasible when compared to other products because only two electrons are required for this reaction.[102] More electrons and protons are required to overcome the energy barriers for the complex products[102] (eqs 8−13). Moreover, the adsorption behavior of CO_2 on the photocatalyst surface could influence the CO_2 conversion efficiency. Tu et al.[125] proposed various models of CO_2 adsorption on the photocatalyst surface (Figure 4), such as liner adsorption via an O atom (Figure 4a), adsorption through a C atom to form a monodentate carbonate species (Figure 4b), adsorption via an O and C atom to create bidentate carbonate species (Figure 4c), and bridged carbonate geometry (C atom pointing downward (Figure 4d and upward (Figure 4e) through the bonding of two O atoms of CO_2 with metal−oxygen−metal (M−O−M).

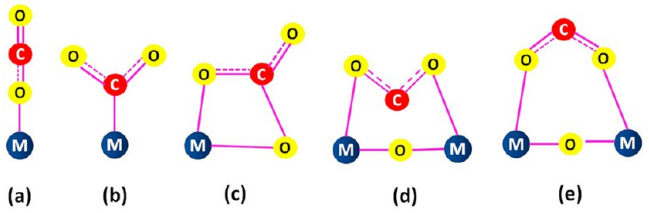

Figure 4. Proposed models of CO_2 adsorption on a photocatalyst surface.[125] Modified and reproduced with permission from ref 125. Copyright (2014), John Wiley and Sons.

The PEC activity and product formation are strongly impacted by the lifetime of charge carriers and light absorption capability of the electrode material. The time scale of surface reactions (picoseconds to microseconds) for CO_2 conversion is higher as compared to the lifetime (femtoseconds to picoseconds) of charge carriers.[126] The kinetic barriers for proton coupled electron transfer reactions could be overwhelmed with the help of suitable photoelectrode materials and co-catalysts that are capable of breaking a C−O bond and favor C−H bond formation.[94,126] The fabrication of electrodes with required surface features and band edge positions is crucial to improve the CO_2 conversion efficiency. PEC efficiency of semiconductors could also be improved by band gap engineering (e.g., doping) or incorporating a co-catalyst (e.g., plasmonic metals (Au, Cu), noble metals (Pt, Pd), non-noble metals (Cu, Sn, and Fe), or nonmetals (conductive polymers, organic molecular complex with ammonium and pyridinium ions). It was also reported that the PEC efficiency can be improved using biological systems (enzymes), changing structural features/morphology, construction of a Schottky junction, solid electrolytes, and deposition of an electron transport layer (e.g., molecular catalysts).[126] Kim et al.[127] suggested that HCHO and HCOOH productions were facilitated through sp^2 hybrid carbon atoms at low reduction potentials. The formation of alcohols was enabled via sp^3 hybrid carbon atoms at high reduction potentials. The reduction potential, product formation, and selectivity of CO_2 conversion using a Cu cathode and $BiVO_4$ anode are shown schematically in Figure 5.[127] The poor solubility of CO_2 (0.33 mol/L at 25 °C and 1 atm pressure) is the main kinetic barrier for the mass transfer limitations toward product selectivity.[126] The efficiency of this technique could also be influenced by the concentration and characteristics of co-catalysts. The light absorption process could be maximized by controlling the morphology, and plasmonic effect of the co-catalyst.[126] The charge carrier separation could be surpassed through the construction of Schottky junctions and coating of

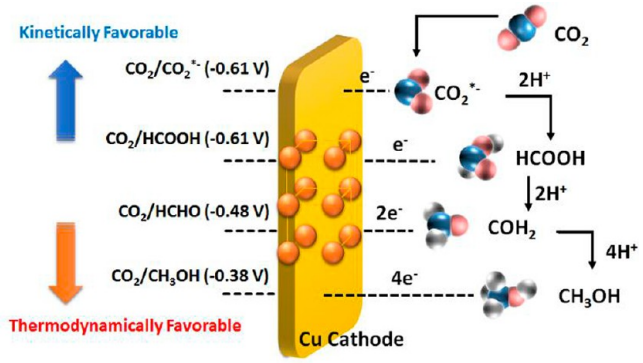

Figure 5. Reduction potential, product formation, and selectivity of CO_2 conversion using a Cu cathode, $BiVO_4$ anode, and NaCl electrolyte.[127] Reproduced with permission from ref 127. Copyright (2018), American Chemical Society.

https://dx.doi.org/10.1021/acsenergylett.9b02585
ACS Energy Lett. 2020, 5, 486−519

the electron transfer channel layer (e.g., Re(*t*-Bu-bipy-$(CO)_3Cl$)) at the electrode−catalyst interface.[126]

Determination of Efficiency: The efficiency of PEC CO_2 conversion can be expressed in various terms as follows:[128]

Solar-to-Fuel Conversion Efficiency (STF):

$$\mathrm{STF} = \frac{r_{\mathrm{fuel}}\ (\mathrm{mmole\ of\ fuel/s}) \times \Delta G^{\circ}\ (\mathrm{kJ/mol})}{P_{\mathrm{solar}\ (\mathrm{mW/cm^2})} \times \mathrm{Area}\ (\mathrm{cm^2})} \tag{16}$$

where r_{fuel} is the quantity of fuel produced per second, ΔG° is the Gibbs free energy, P_{solar} is the power density of light (AM 1.5G), and Area is the photoelectrode area under light irradiation. STF can also be defined in terms of photocurrent density (J_{sc}) as follows

$$\mathrm{STF} = \frac{J_{\mathrm{sc}}\ (\mathrm{mA/cm^2}) \times \Delta E^{\circ}\ (\mathrm{V}) \times \mathrm{FE}}{P_{\mathrm{solar}}\ (\mathrm{mW/cm^2})} \tag{17}$$

where ΔE° is the thermodynamic energy stored in the PEC reactor and FE is the Faradaic efficiency. FE can be calculated from the current input and output of CO_2 conversion as follows

$$\mathrm{FE}\ (\%) = \frac{e_{\mathrm{output}}}{e_{\mathrm{input}}} \times 100 = \frac{n\ (\mathrm{mol}) \times y}{\frac{Q\ (\mathrm{Coulomb})}{F\ (\mathrm{Coulomb/mol})}} \times 100 \tag{18}$$

In the above equation, n is the moles of product, y is the number of electrons needed to convert CO_2 into a particular product, Q is the calculated electric charge, and F is the Faraday constant (96485 C/mol).

Applied Bias Photon-to-Current Efficiency (ABPE): ABPE is used to measure the efficiency when an external voltage (V_{bias}) is applied between the counter and working electrodes.

$$\mathrm{ABPE} = \frac{J_{\mathrm{ph}}\ (\mathrm{mA/cm^2}) \times [\Delta E^{\circ}\ (V) - V_{\mathrm{bias}}\ (V)] \times \mathrm{FE}}{P_{\mathrm{solar}}\ (\mathrm{mW/cm^2})} \tag{19}$$

where J_{ph} is the photocurrent detected under the external voltage.

Incident Photon-to-Current Efficiency (IPCE): IPCE is a widely used tool to measure the efficiency of a photoelectrode. The conversion of incident photons to photocurrent as a function of irradiation wavelength can be measured in terms of IPCE. It can be determined in the presence or absence of an external voltage.

$$\mathrm{IPCE} = \frac{hc}{e}\frac{J_{\mathrm{ph}}}{P_{\mathrm{mono}} \times \lambda} = \frac{J_{\mathrm{ph}}\ (\mathrm{mA/cm^2}) \times [1239.8\ (\mathrm{V \times nm})]}{P_{\mathrm{mono}(\mathrm{mW/cm^2})} \times \lambda(\mathrm{nm})} \tag{20}$$

In this equation, h is Planck's constant, c is the speed of light, and e is the charge of electrons. P_{mono} and λ are the power density and wavelength of monochromatic light, respectively.

Absorbed Photon-to-Current Efficiency (APCE): The APCE tool can be used by considering only the absorption of light ($A(\lambda)$). It can be calculated as follows

$$\mathrm{APCE}(\lambda) = \frac{\mathrm{IPCE}(\lambda)}{A(\lambda)} = \frac{\mathrm{IPCE}(\lambda)}{1 - R - T} \tag{21}$$

where R and T are the reflectance and transmittance of monochromatic light.

STF, FE, ABPE, IPCE, and APCE could be used to determine the efficiency of a photoelectrode material for CO_2 conversion. Nevertheless, the FE has been commonly used in most of the studies to highlight the PEC CO_2 conversion efficiency. FEs of the recent electrode materials are compared and shown in Table S1. The 3D cobalt phosphate/bismuth vanadate/tin oxide (Co−Pi/$BiVO_4$/SnO_2) photoanode showed 90% FE toward CO selectivity using an H-shaped PEC reactor (cathode: C−Au/carbon polymer plate; anolyte: potassium phosphate buffer solution; catholyte: potassium bicarbonate ($KHCO_3$) solution; applied voltage: 1.1 V; IPCE: 50%).[129]

Recently, Kalamaras et al.[130] reported the thermodynamic analysis of PEC CO_2 conversion into CH_3CH_2OH using single- and double-junction photoabsorbers under the same conditions. Web-based model software was used to study the PEC efficiency. It was suggested that the PEC CO_2 conversion is only feasible when the potential supplied by the photocatalyst is similar to or higher than the thermodynamic potential (E_{Therm}) with any other losses.

$$\sum_{1}^{n} E_{\mathrm{PV}}(j) \geq E_{\mathrm{Therm}} + \eta_{\mathrm{Red}}(j) + \eta_{\mathrm{ox}}(j) + E_{\mathrm{Ionic,Res}}(j) + E_{\mathrm{Elec,Res}}(j) - E_{\mathrm{Bias}}(j) \tag{22}$$

where n signifies the number of light-absorbing materials (photocatalyst) and j represents the current density (A/cm^2). η_{Red} and η_{ox} are the reduction and oxidation overpotentials (V), respectively. E_{Ionic} and E_{Elec} are the losses as a result of ionic and electric resistance, correspondingly. E_{Bias} is the external bias used. The current density (j) could be calculated from the following equations.

$$j = j_{\mathrm{Limit}} - j_0 \times \exp\left(\frac{q(V + j\Omega_{\mathrm{Series}})}{kT} - 1\right) - \frac{(V + j\Omega_{\mathrm{Series}})}{\Omega_{\mathrm{Shunt}}} \tag{23}$$

$$j_0 = M_{\mathrm{user}} \times qA\frac{2kT}{h^3c^2} \times ({E_{\mathrm{g}}}^2 + 2kTE_{\mathrm{g}} + (kT)^2) \times \exp\left(\frac{-E_{\mathrm{g}}}{kT}\right) \tag{24}$$

Here, j_{Limit} denotes the maximum theoretical photocurrent density at a given number of absorbed photons. j_0, q, V, and Ω are the dark saturation current density, charge, photovoltage, and resistance, respectively. A represents the emitted surface of a material, and M_{user} denotes the minimum theoretical saturation current. E_g, k, T, h, and c are the band gap energy, Boltzmann's constant, temperature, Planck's constant, and speed of light, respectively. STF efficiency was finally calculated from the current density, E_{Therm}, FE, and incident solar power (P_{in}) by the following equation.

$$\mathrm{STF}(E_{\mathrm{g}}) = \frac{j \times E_{\mathrm{Therm}} \times \mathrm{FE}}{P_{\mathrm{in}}} \times 100\% \tag{25}$$

Reactor Designs: The PEC reactor configuration is very significant in relation to product selectivity.[131,132] In most cases, an H-type reactor has been used for the PEC CO_2 conversion.[133−139] The mass transfer and reaction kinetics are governed by the reactor design.[140] Factors such as light source,

https://dx.doi.org/10.1021/acsenergylett.9b02585
ACS Energy Lett. 2020, 5, 486−519

membrane characteristics, fabrication material, wall thickness, mode of operation (e.g., batch, flow, continuous, etc.), heat exchange, requirement of phases (e.g., gas−solid, liquid−solid, and gas−liquid−solid), solubility of CO_2, and mixing or flow features should be considered for the PEC reactor design.[140] The recycling of unreacted CO_2 must also be taken into consideration for an effective PEC reactor design. The light irradiation should be homogeneously dispersed on the photoactive electrode surface.[141] Xenon (Xe) arc lamps with suitable filters have been commonly employed as the light irradiation source to mimic the solar light.[7,116,142−150] The absorption of photons could be enriched by tuning the optical path length of light inside of the reactor.[140] Quartz and Pyrex glasses are commonly utilized for the fabrication of PEC reactors. The heat produced by the lamp under prolonged irradiation could be avoided with the help of a water bath.[151] The proper mixing of reactants by a magnetic stirrer is beneficial to improve the contact among photons, CO_2, electrolyte, and electrode active sites.[140] PEC reactors with two compartments setup are more convenient in comparison to a single-compartment reactor. The separation of products in a single-compartment reactor is a complicated and expensive process.[152] The schematic of an H-type PEC reactor for CO_2 conversion is shown in Figure 6.

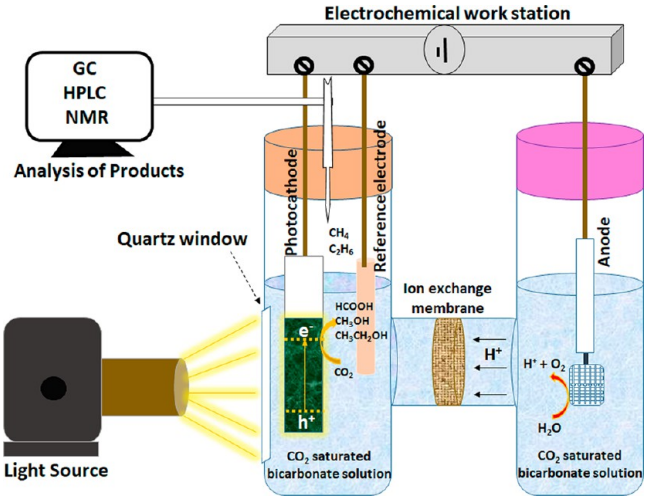

Figure 6. Schematic of an H-type PEC reactor for CO_2 conversion into various fuels and value-added products.

Factors such as the light source, membrane characteristics, fabrication material, wall thickness, mode of operation (e.g., batch, flow, continuous, etc.), heat exchange, requirement of phases (e.g., gas−solid, liquid−solid, and gas−liquid−solid), solubility of CO_2, and mixing or flow features should be considered for PEC reactor design.

The anode and cathode compartments are separated via a proton exchange membrane (PEM; e.g. Nafion). PEM is commonly preferred when compared to anion exchange membrane (AEM). The probable reactions occur in the PEM and AEM based PEC reactors are given below:[140]

PEC Reactors with PEM:

Anode:

$$2H_2O \leftrightarrow O_2 + 4H^+ + 4e^- \quad (26)$$

Cathode:

$$CO_2 + 2H^+ + 2e^- \rightarrow CO + H_2O \quad (27)$$

$$2H^+ + 2e^- \leftrightarrow H_2 \quad (28)$$

PEC Reactors with AEM:

Anode:

$$2HCO_3^- \leftrightarrow 0.5O_2 + H_2O + 2CO_2 \quad (29)$$

Cathode:

$$3CO_2 + H_2O + 2e^- \leftrightarrow CO + 2HCO_3^- \quad (30)$$

$$2CO_2 + 2H_2O + 2e^- \leftrightarrow H_2 + 2HCO_3^- \quad (31)$$

Bipolar membranes with cation and anion exchange characteristics have gained much interest in recent years, owing to their high sensitivity to pH and the selective transport of ions to the cathode and anode compartments.[153−157] The semiconductor could be utilized in any form of photoelectrode such as cathode (p-type), anode (n-type), and anode−cathode (p- and n-type, Z-scheme system). At the photoanode, water is oxidized into O_2 by photogenerated holes (h^+). CO_2 is reduced into value-added products at the photocathode with the help of photogenerated electrons. The reactions may be carried out in the presence or absence of a co-catalyst. CO_2 solubility restrictions could be avoided using gas diffusion electrodes (GDEs) and gas-phase operation at the cathode compartment.[105,108,158−165] The utilization of GDEs could also enhance the CO_2 conversion efficiency via promoting mass transport.[157,166]

Irtem et al.[167] investigated the PEC conversion of CO_2 to fuel using a filter press flow reactor design. The schematic and images of the PEC flow reactor design are shown in Figure 7. This kind of setup is advantageous in minimizing the ohmic drop of the EC cell, and it contributes to the complete irradiation of the photoelectrode film. The reactor was constructed from polytetrafluoroethylene. It was comprised of back-illuminated TiO_2 nanorods/FTO as the photoanode and Sn-deposited GDE as the cathode. The anode and cathode compartments were separated though a Nafion 117 membrane. Sodium hydroxide (NaOH, 0.5 M) and sodium bicarbonate ($NaHCO_3$, 0.5 M) were employed as anolyte and catholyte solutions, respectively. The solutions were continuously flowed via a dual peristaltic pump to collect the liquid products. There were three inputs (anolyte, cathotyle, and CO_2) and two outputs (anolyte and cathotyle with CO_2) in the PEC reactor. CO_2 gas flow was kept constant at 10 mL/min using a mass flow controller with a volumetric digital flow meter. A 300 W Xe arc lamp with an AM 1.5G filter was used as a light irradiation source. The energy efficiency (EE) of the flow reactor was calculated as follows

https://dx.doi.org/10.1021/acsenergylett.9b02585
ACS Energy Lett. 2020, 5, 486−519

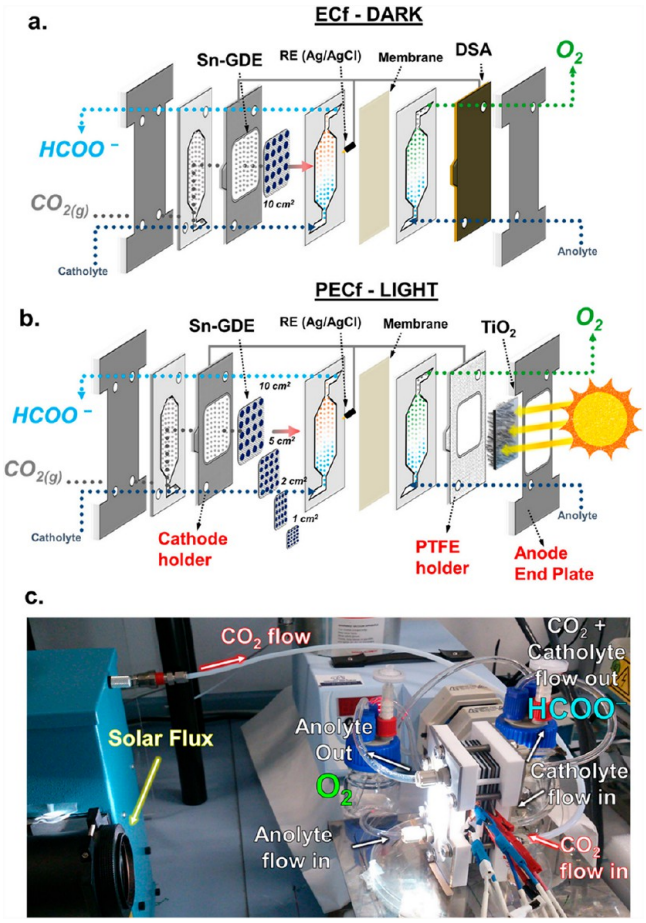

Figure 7. (a) Electrochemical flow reactor in the dark (EC_f-dark) with a dimensionally stable anode (DSA). (b) PEC flow reactor with light irradiation (PEC_f-light) and a TiO_2 photoanode. (c) Photograph of the PEC flow reactor setup.[167] Reproduced with permission from ref 167. Copyright (2017), Elsevier.

$$\mathrm{EE}\ (\%) = \frac{\text{Productivity (mol/s)}\cdot\Delta H^0_{\mathrm{comb}}\ (\mathrm{J/mol})}{I_{\mathrm{cell}}\ (\mathrm{A})\cdot E_{\mathrm{cell}}\ (\mathrm{V})}100 = \mathrm{FE}\ (\%)\frac{E_{\mathrm{therm}}\ (\mathrm{V})}{E_{\mathrm{cell}}\ (\mathrm{V})} \quad (32)$$

The photon flux and photoanode-to-cathode area are the main parameters to influence the efficiency of the PEC reactor. At an applied bias voltage of 1.2 V, a FE of 53% was achieved with 58% EE and 0.24 STF (for formate production) at 200 mW/cm^2 of light irradiance and a 2 cm^2 cathode area.

Zhou and Xiang analyzed the STF conversion efficiency of CO_2 reduction using two different photovoltaic (PV)−EC reactor configurations (Reactor I: a direct one-step CO_2 reduction; Reactor II: a two-step cascade CO_2 reduction).[168] The configurations of the two reactors are shown in Figure 8. A DC-to-DC convertor was used to accomplish the power among the EC reactor, PV unit, fuel-producing component, and power-creating unit.

STF conversion efficiency ($\eta_{\mathrm{STF\_discrete}}$) of the discrete reactor configuration was defined as follows

$$\eta_{\mathrm{STF\_discrete}} = \eta_{\mathrm{PV}}\cdot\eta_{\mathrm{ETF}}\cdot\eta_{\mathrm{DC-DC\ converter}} \quad (33)$$

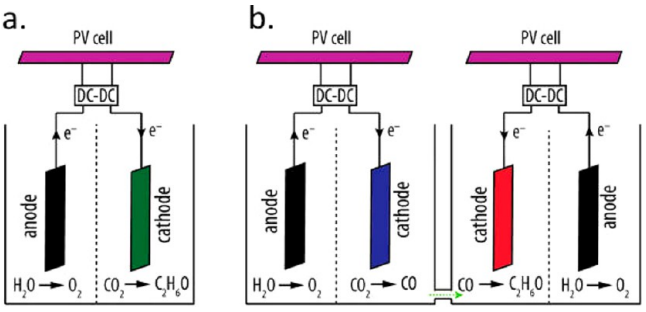

Figure 8. Schematic illustration of the PV−EC reactor configuration: (a) one step reactor (b) two step reactor.[168] Reproduced with permission from ref 168. Copyright (2018), American Chemical Society.

where η_{PV} and η_{ETF} represent the solar-to-electric conversion efficiency of the PV cell and the electric-to-fuel (ETF) conversion efficiency of the EC cell, respectively.

$$\eta_{\mathrm{ETF\_one\_Step}} = \frac{E_{\mathrm{CO_2\ to\ C_2H_6O}}}{V_{\mathrm{CO_2\ to\ C_2H_6O}}}\mathrm{FE}_{\mathrm{CO_2\ to\ C_2H_6O}} \quad (34)$$

$$\eta_{\mathrm{ETF\_two\_Step}} = \frac{\frac{3}{2}E_{\mathrm{CO_2\ to\ C_2H_6O}}\cdot\mathrm{FE}_{\mathrm{CO\ to\ C_2H_6O}}}{\frac{\mathrm{FE}_{\mathrm{CO\ to\ C_2H_6O}}}{2\mathrm{FE}_{\mathrm{CO_2\ to\ CO}}}V_{\mathrm{CO_2\ to\ CO}} + V_{\mathrm{CO\ to\ C_2H_6O}}} \quad (35)$$

Here, E is the thermodynamic voltage and V is the total voltage. V could be calculated as follows

$$V_{\mathrm{CO_2\,to\,C_2H_6O}} = E_{\mathrm{CO_2\,to\,C_2H_6O}} + V_{\mathrm{anode\ loss}} + V_{\mathrm{cathode\ loss\ CO_2\,to\,C_2H_6O}} + V_{\mathrm{transport\ loss}} \quad (36)$$

$$V_{\mathrm{CO_2\,to\,CO}} = E_{\mathrm{CO_2\,to\,CO}} + V_{\mathrm{anode\ loss}} + V_{\mathrm{cathode\ loss\ CO_2\,to\,CO}} + V_{\mathrm{transport\ loss}} \quad (37)$$

$$V_{\mathrm{CO\,to\,C_2H_6O}} = E_{\mathrm{CO\,to\,C_2H_6O}} + V_{\mathrm{anode\ loss}} + V_{\mathrm{cathode\ loss\ CO\,to\,C_2H_6O}} + V_{\mathrm{transport\ loss}} \quad (38)$$

where $V_{\mathrm{anode\ loss}}$ is the anodic voltage loss for water oxidation, $V_{\mathrm{cathode\ loss}}$ is the cathodic voltage loss for CO_2 reduction, and $V_{\mathrm{transport\ loss}}$ is the transport voltage loss from the electrolyte and membranes.

As the wireless photoelectrodes were used in the two reactors, the STF could be elucidated as follows

$$\eta_{\mathrm{STF\_integrated\_one\_Step}} = \frac{J_{\mathrm{CO_2\ to\ C_2H_6O}}E_{\mathrm{CO_2\ to\ C_2H_6O}}\mathrm{FE}_{\mathrm{CO_2\ to\ C_2H_6O}}}{P_{\mathrm{in}}} \quad (39)$$

$$\eta_{\mathrm{STF\_integrated\_two\_Step}} = \frac{3E_{\mathrm{CO_2\ to\ C_2H_6O}}\mathrm{FE}_{\mathrm{CO\ to\ C_2H_6O}}}{P_{\mathrm{in}}\left(\frac{1}{J_{\mathrm{CO_2\ to\ CO}}\mathrm{FE}_{\mathrm{CO_2\ to\ CO}}} + \frac{2}{J_{\mathrm{CO\ to\ C_2H_6O}}\mathrm{FE}_{\mathrm{CO\ to\ C_2H_6O}}}\right)} \quad (40)$$

where J and P_{in} are the operating current intensity and incident illumination intensity, respectively. The results suggested that the STF conversion efficiency of the reactor configuration with two steps was higher than that for the reactor with one step in

https://dx.doi.org/10.1021/acsenergylett.9b02585
ACS Energy Lett. 2020, 5, 486−519

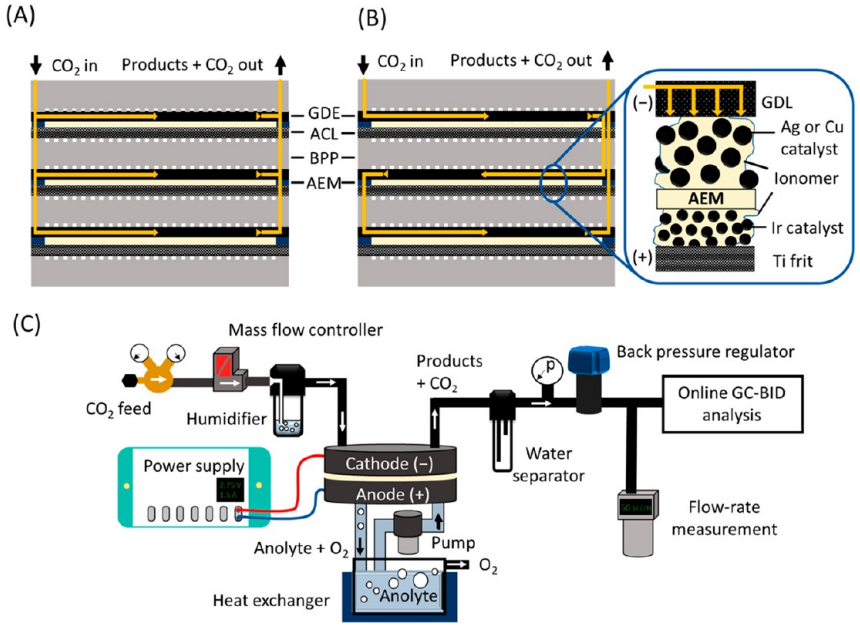

Figure 9. Schematic of the three-layer electrolyzer stack with CO_2 gas flow: (A) parallel connection, (B) series connection. (C) Flowchart of the experimental setup.[169] Reproduced with permission from ref 169. Copyright (2019), American Chemical Society.

all cases. The two-step reactor configuration is highly beneficial for the selective reduction of CO_2 with high efficiency.

In a recent study, an innovative multilayer electrolyzer stack (zero-gap membrane electrolyzers) without any catholyte was used to convert CO_2 into gaseous products at high efficiency.[169] The pressurized CO_2 gas could be directly fed into the cathode through zero-gap membrane electrolyzers. The schematic of the electrolyzer stack and flowchart of the experimental setup are shown in Figure 9. The important features of this setup are (i) a low cell voltage (−3.0 V) with high conversion efficiency (up to 40%); (ii) a catholyte and any liquid circulation loop are not required; (iii) CO_2 dissolution issues could be minimized; (iv) the inlet could be easily pressurized (up to 10 bar); and (v) a high product selectivity. The multilayer stack has a GDE, gas diffusion layer (GDL), bipolar plate (BPL), anode catalyst layer (ACL), and AEM. The cells can be connected in parallel or series for the CO_2 gas flow. In the parallel cells setup, the CO_2 gas was circulated into each cathode with equal distribution (Figure 9a). For the series cells connection, the total CO_2 gas flux was entered into the first layer, and the remnant gas with product was continuously flowed into the next layer, leading to high CO_2 conversion efficiency. In both cases, the same amount of current was passed. Ag nanoparticles and electrodeposited Cu nanocubes on a GDL were separately used as the electrocatalyst for the CO_2 conversion. The results showed that CO, CH_4, ethane (C_2H_4), and H_2 were produced for the Cu catalyst, while CO and H_2 were formed for the Ag catalyst. The operational parameters were optimized using a Ag catalyst. The current density of CO formation was almost the same for the single cell and the stack in the parallel setup. For the series setup, the CO_2 conversion efficiency of the stack was higher (with 95% of FE) as compared to the single cell. A higher efficiency was achieved even at a low CO_2 gas flow rate. The efficiency was also examined at various CO_2 pressures. The CO formation current density was increased from 250 to 300 mA/cm^2 when increasing the CO_2 inlet pressure. It was proposed that the use of a multilayer stack in series mode would decrease the capital investment cost and support its implementation in industry.

In another study, an artificial photosynthetic reactor was utilized for syngas (CO/H_2) production from CO_2 and H_2O.[170] The schematic and mechanism of the PV coupled photosynthetic reactor are shown in Figure 10. The reactor

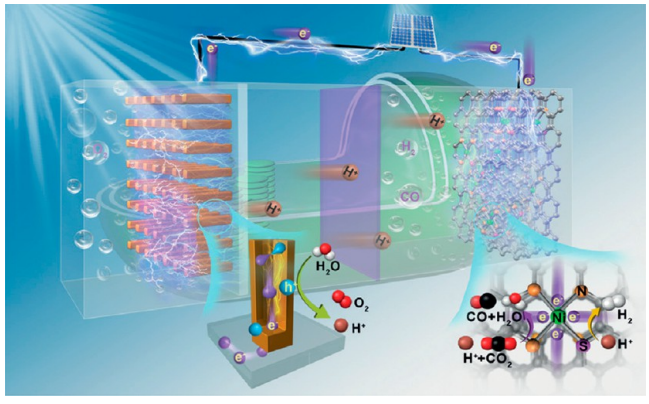

Figure 10. Schematic and mechanism of CO_2 reduction to syngas using an artificial photosynthetic reactor with semiconductor nanorod arrays as the photoanode and S and N codoped graphene with atomically dispersed Ni active sites as the cathode.[170] Reproduced with permission from ref 170. Copyright (2019), John Wiley and Sons.

was composed of two compartments with a semiconductor photoanode (nanorod arrays), CO_2 reduction catalyst (S and N codoped graphene with atomically dispersed Ni active sites), and a Nafion membrane. The light-induced water oxidation reaction (photosystem II) and the multielectron CO_2 reduction in the dark are the fundamentals of this reactor setup. The light compartment was filled with 60 mL of an Ar gas-saturated 0.1 M NaOH solution, whereas the dark was supplied with 60 mL of a CO_2 gas-saturated 0.1 M $NaHCO_3$ solution. A high CO_2 conversion rate of 154.9 mmol/h for CO

https://dx.doi.org/10.1021/acsenergylett.9b02585
ACS Energy Lett. 2020, 5, 486−519

formation was achieved under solar light irradiation with 13.6% solar-to-syngas conversion efficiency. Moreover, the syngas production was tunable with a wide range between 1:2 and 5:1 of CO:H_2. The experiments were performed with various photoanode materials (N−TiO_2, Sn−$BiVO_4$, and Sn−Fe_2O_3) to test the reactor efficiency. More than 80% of FE was achieved for the three photoanode materials involved in CO formation. Among them, N−TiO_2 nanorod arrays showed the highest efficiency (TOF of 529.5 h^{-1}) with 20 h stability. The multielectron CO_2 reduction reaction was kinetically favored through the localization of electrons on the Ni single atoms in the reduction catalyst.

A continuous-flow microfluidic PEC reactor was operated for the conversion of CO_2 into liquid fuels by an iron oxide/cupric oxide (α-Fe_2O_3/CuO) photocathode.[171] The microfluidic PEC reactor was used to promote the transfer of reactants and intermediates from the active sites of the electrode for product formation. The electrodes were prepared through an electrodeposition technique on an FTO plate. A CO_2-saturated 0.2 M $NaHCO_3$ aqueous solution was used as an electrolyte. The schematic of the sandwich-type microfluidic PEC reactor is displayed in Figure 11. The total volume of the

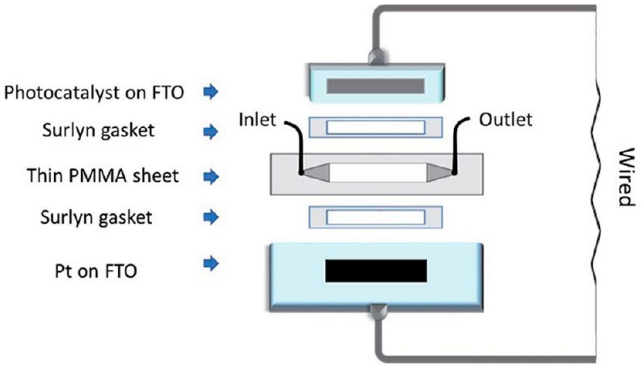

Figure 11. Schematic of the microfluidic PEC reactor for CO_2 conversion.[171] Reproduced with permission from ref 171. Copyright (2019), Royal Society of Chemistry.

chamber was 50 μL. The reactor was designed using low-cost materials without an ion exchange membrane. A poly(methyl methacrylate) (PMMA) sheet of 100 μm thickness was placed between the photocathode (CuO on FTO) and counter electrode (Pt on FTO). The reactor was sealed by placing a thermoplastic film (Surlyn gasket of 30 μm) between the PMMA sheet and electrode. A solar simulator with an AM 1.5G filter was utilized as the light irradiation source. The electrolyte was purged though a syringe pump at various flow rates such as 40, 80, 120, and 200 μL min^{-1}. The efficiency of the microfluidic PEC reactor was higher at a flow rate of 80 μL min^{-1}. The poor efficiency at low flow rates was ascribed to a small fluidic drag force by the formation of O_2 bubbles in the microchamber. The drag force was larger at high flow rates, and this could affect the diffusion of products across the electrodes. The small interelectrode distance was favorable to reduce the current gradient and promote the transfer of intermediates. The α-Fe_2O_3/CuO photocathode showed a STF efficiency of 0.48% with high photocurrent density (−1 mA/cm^2) at 0.3 V.

Electrolytes: The choice of electrolyte is very important in PEC CO_2 conversion, and it could directly or indirectly affect the product selectivity. The long-term stability of electrolytes is

The choice of electrolyte is very important in PEC CO_2 conversion, and it could directly or indirectly affect the product selectivity.

ruled by its pH, ionic strength, and concentration.[92,108] CO_2 gas-saturated aqueous solutions of $NaHCO_3$[172−176] or potassium bicarbonate ($KHCO_3$)[129,154,177−180] are most commonly utilized as the electrolyte for the PEC CO_2 conversion experiments. A higher concentration of bicarbonate could screen the electric field and support the H_2 evolution reaction compared to CO_2 conversion.[181] Consequently, the aqueous solution of bicarbonate with a concentration range of 0.1−0.5 M is commonly preferred. Organic solvents (e.g., dimethyl sulfoxide,[182] dimethylformamide,[183] acetonitrile,[184,185] etc.),[186] ionic liquids (e.g., 1-ethyl-3-methylimidazolium tetrafluoroborate,[187] 1-butyl-3-methylimidazolium salts,[188] etc.),[189,190] and solid oxide (e.g., Ba-$CeO_{0.5}Zr_{0.3}Y_{0.16}Zn_{0.04}O_{3-\delta}$) are also employed as electrolytes in some recent studies to improve the solubility of CO_2.[87,191−193] Organic solvent electrolytes are employed to suppress the H_2 evolution reaction and improve the CO_2 conversion efficiency. However, CO is the main product from CO_2 conversion as aprotic organic solvents are used as the electrolyte. Organic solvents require a small concentration of proton source (e.g., water) to form products such as CH_4, CH_3OH, etc.[184] The effect of water content on the product selectivity of the Cu electrode was evaluated in acetonitrile solvent with supporting electrolytes (tetraethylammonium tetrafluoroborate, tetraethylammonium trifluoromethanesulfonate, and sodium trifluoromethanesulfonate).[184] In situ Fourier transform infrared spectroscopy (FTIR) and surface-enhanced Raman spectroscopy were used to analyze the products and reaction intermediates. The results showed that the mechanism of the CO_2 conversion reaction in acetonitrile was highly influenced by the water content. Acetonitrile was decomposed into acetamide in the presence of water. Moreover, bicarbonates were formed as the product in addition to CO. This was ascribed to the reaction between CO_2 and electrogenerated hydroxyl groups. In a similar study, the electrocatalytic CO_2 conversion efficiency of TiO_2 was tested in the presence of acetonitrile solvent and tetrabutylammonium perchlorate (TBAP) as the supporting electrolyte.[194] At −1.8 V, CH_3OH was detected as the main product with 60% FE in the presence of 0.1 M acetonitrile/TBAP and 0.5 M water. The onset cathodic current of TiO_2 electrodes was shifted to negative potential in the presence of water. This was ascribed to the establishment of equilibrium between CO_2 and water. Like organic solvents, ionic liquids are one of the promising electrolytes for PEC CO_2 conversion. Ionic liquids could create unique coordination with CO_2 molecules, and it could promote the CO_2 conversion by reducing the energy barrier to produce a $CO_2^{\bullet-}$ intermediate.[92]

Analytical techniques such as gas chromatography (GC),[73,74,77,129,195−197] high-performance liquid chromatography (HPLC),[198−203] and nuclear magnetic resonance (NMR)[204−207] are commonly used to measure the gaseous and liquid products formed during the PEC CO_2 conversion.

Kinetics: There are only a very few studies available on the kinetics of PEC CO_2 conversion. The surface reactions occurring at the electrode are the rate-determining steps

https://dx.doi.org/10.1021/acsenergylett.9b02585
ACS Energy Lett. 2020, 5, 486−519

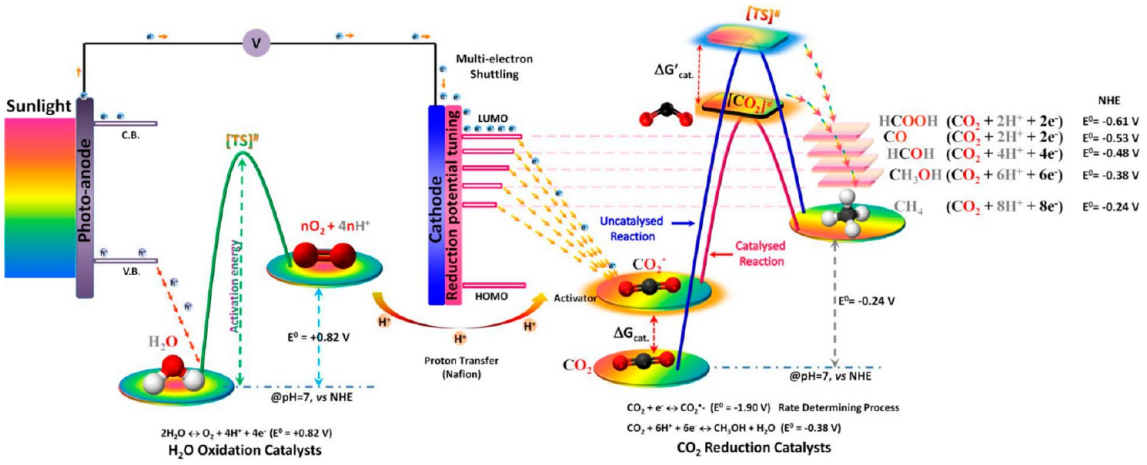

Figure 12. Thermodynamic energy level diagram of PEC CO_2 conversion and water splitting in the presence and absence of catalyst.[97] Reproduced with permission from ref 97. Copyright (2019), American Chemical Society.

owing to the thermodynamic and kinetic barriers for CO_2 conversion.[126] The standard Gibbs free energies of formation for CO, HCHO, HCOOH, and CH_4 are −137.2, −109.9, −361.4, and −51 kJ/mol, respectively. The conversion of CO_2 into $CO_2^{\bullet-}$ intermediate is generally considered the main rate-limiting step.[92] The thermodynamic energy level diagram of PEC CO_2 conversion and water splitting in the presence and absence of catalyst is shown in Figure 12.[97]

The equilibrium potential for the formation of $CO_2^{\bullet-}$ intermediate is −1.9 V vs NHE.[208] The redox potentials of CO, HCHO, HCOOH, CH_3OH, and CH_4 formation vs NHE at pH 7 are −0.53, −0.48, −0.61, −0.38, and −0.24 V, respectively.[208] The activation energy (ΔG^*) of CO_2 conversion reaction intermediates at the transition state could be reduced with the help of suitable photoelectrode materials. An activated complex of CO_2 is formed in the reactant state ($[CO_2^*]$) in the presence of catalyst or electrode material (Figure 12). Moreover, the electrode material could reduce the thermodynamic energy level and activation energy to produce the transition state complex ($[CO_2]^{\#}$) via electron transfer.[97] The adsorbed $CO_2^{\bullet-}$ intermediate on the electrode surface is stabilized through the electron transfer from the d orbital of catalyst to π^* antibonding orbital of the $CO_2^{\bullet-}$ intermediate, suggesting the band bending reaction and decrease of activation energy for the proton coupled electron transfer reactions.[97,209] The formation of products from the $CO_2^{\bullet-}$ intermediate relies on the number of protons and electrons that transfer (eqs 8−13). For example, CO and HCOOH are produced by the transfer of two electrons and protons. CH_3OH and CH_4 formations require six and eight protons and electrons to transfer, respectively. Twelve proton−electron transfers are needed for the $CO_2^{\bullet-}$ intermediate to produce CH_3CH_2OH. The C_1 product formation mechanism is facilitated through the establishment of *CHO or *COH species.[97] In the case of C_2 products, $*C_2O_2^-$ species are necessary for the C−C bond-making reaction.[97] The rate-determining steps of these products are governed by the electron or proton transfer mechanism.[97,210] The CB edge of most photoelectrode materials is positioned below the redox potential of the $CO_2^{\bullet-}$ intermediate, indicating that the conversion is thermodynamically an uphill reaction. This could be rectified by an external electrical bias. The photoinduced charge transfer kinetics is determined from the energy levels of electrode materials and redox reagents. The rate of the reaction is dependent on the photocurrent density of the electrode material.

The reaction kinetics is maneuvered via the polarization of CO_2, the nature of nucleophiles or electron-donating groups, the concentration of available protons, and the coordination of CO_2 molecules with metal catalyst.[114] The equilibrium, concentration of reactants, adsorption of intermediates, reaction pathways, and product formation are strongly influenced by the electrolyte pH.[211] Neutral or alkaline pH solutions are preferred to improve the kinetics of CO_2 conversion and to avoid the H_2 evolution reaction.[92] The effect of pH on the product selectivity of the Cu/Cu_2O photoelectrode for CO_2 conversion was investigated using a sodium carbonate/bicarbonate buffer solution as the supporting electrolyte.[211] The reactions were carried out in the pH range of 8−11 at an applied potential of 0.2 V. CH_3OH production was in the following order: pH 8 > pH 9 > pH 10 > pH 11. This was attributed to the changes in CO_2/intermediate adsorption and the concentration of hydrogen radicals responsible for CH_3OH production. At pH 8, the hydroxyl radicals ($^{\bullet}OH$) were effectively scavenged by the bicarbonate ions (HCO_3^-).[211] Therefore, the concentration of hydrogen radicals was sufficient for CH_3OH production.[211] At high electrolyte pH, carbonate ions (CO_3^{2-}) were the dominant species in the electrolyte, which could scavenge the hydrogen radicals and suppress the CH_3OH production.[211] The role of HCO_3^- was further studied in detail for the EC reduction of CO_2 into CO at the Au electrode surface by the integration of isotopic labeling and spectroscopic (in situ attenuated total reflectance surface-enhanced infrared absorption spectroscopy (ATR-SEIRAS) and mass spectroscopy) techniques.[212] The high CO_2 conversion efficiency was ascribed to the rapid equilibrium between HCO_3^- and dissolved CO_2 ($CO_{2(aq)}$) in the electrolyte solution. It was proposed that the carbon source for CO production was mainly supplied by HCO_3^- via its quick equilibrium with $CO_{2(aq)}$. The effective or reducible $CO_{2(aq)}$ concentration near the electrode surface was intensified by the rapid equilibrium exchange between HCO_3^- and $CO_{2(aq)}$ species. HCO_3^- could enhance the rate of the reaction via enabling the transportation of $CO_{2(aq)}$. The main role of gaseous CO_2 ($CO_{2(g)}$) was to maintain the equilibrium concentration of $CO_{2(aq)}$. Similar

https://dx.doi.org/10.1021/acsenergylett.9b02585
ACS Energy Lett. 2020, 5, 486−519

results were also observed for other metal electrodes such as Zn and Ag.[212]

Recently, Luo et al.[213] reported a 2D numerical model (COSMOL multiphysics) for CO_2 utilization and HCOOH production. PEC experiments were carried out in a continuous flow reactor with the GDE. The computational fluid dynamics with EC kinetics and photocatalysis were used in this model. The half-cell reactions for HCOOH production are given below

At the cathode:

$$CO_2 + H_2O + 2e^- \rightarrow HCOO^- + OH^- \quad (41)$$

$$2H_2O + 2e^- \rightarrow H_2 + 2OH^- \quad (42)$$

At the anode:

$$2OH^- \rightarrow 0.5O_2 + H_2O + 2e^- \quad (43)$$

The current voltage behavior of the photoelectrode was calculated from the Shockley–Queisser model fitted with the ideal diode relationship

$$i = i_I - i_d\left\{\exp\left[\frac{q(V + iR_s)}{kT}\right] - 1\right\} \quad (44)$$

Here, i_I and i_d are the current generated by light and dark conditions, respectively. R_s is the series resistance. The light scattering by bubbles was neglected. Ohm's law was used to describe the transport of electrons and holes.

$$i_s = -\sigma_s \nabla \varnothing_s \quad (45)$$

where σ_s and i_s are the electrical conductivity and current density, respectively. $\varnothing_s$ is the electric potential. The Butler–Volmer equation was employed to model the electrocatalytic reactions at the electrode–electrolyte interface.

$$i = i_0\left[\exp\left(\frac{\propto_a F\eta}{RT}\right) - \exp\left(-\frac{\alpha_c F\eta}{RT}\right)\right] \quad (46)$$

Here, α_a and α_c denote the anodic and cathodic charge transfer coefficients, respectively. The overpotential (η) was calculated from the electric ($\varnothing_s$), electrolyte ($\varnothing_1$), and equilibrium potentials ($\varnothing_0$) as follows

$$\eta = \varnothing_s - \varnothing_1 - \varnothing_0 \quad (47)$$

According to the Nernst–Planck theory of dilute solutions

$$N_i = -D_i \nabla c_i - z_i \mu_i F c_i \nabla \varnothing_1 + v c_i \quad (48)$$

Here, N_i, D_i, c_i, z_i, μ_i, and v represent the molar flux of the species, diffusion coefficient, concentration, charge number, mobility of ions, and velocity, respectively. The velocity was calculated by solving the mass and laminar flow conservation equation

$$\frac{\rho}{\varepsilon} u \cdot \nabla \frac{u}{\varepsilon} = -\nabla p + \frac{\mu}{\varepsilon}\nabla u - \frac{\mu}{K} u \quad (49)$$

$$\nabla u = 0 \quad (50)$$

where ρ is the density, ε is the porosity, p is the pressure, μ is the viscosity, and K is the permeability. Darcy's law and volume-average treatment were utilized for the GDE with parameters such as porosity (γ), tortuosity (λ), and K.

$$\nabla(\rho\gamma u) = S_m \quad (51)$$

$$\nabla(\rho\gamma u u) = -\gamma \nabla p + \nabla\gamma\tau + \rho g - \left(\frac{\mu u}{K}\right) \quad (52)$$

$$\nabla(\rho\gamma u Y_i) - \nabla\left(\rho\frac{\gamma}{\lambda} D_i \nabla Y_i\right) = 0 \quad (53)$$

COSMOL multiphysics was used to solve the equations with different boundary conditions. The model was validated through a comparison of the current density at various overpotentials. It was established that the flow rate of CO_2 was the main parameter influencing the PEC cell efficiency. The current density was increased with respect to the CO_2 flow rate, and at the same time, the CO_2 conversion efficiency was decreased.

In another study, the Langmuir–Hinshelwood kinetic model was proposed for the photocatalytic conversion of CO_2.[214] The experiments were performed using TiO_2 @ hard macrocellular silica foams (Si(HIPE)).

The main semireactions of CO_2 conversion are

$$e^- + H^+ + \frac{1}{2}CO_2 \xrightarrow{k_1'} \frac{1}{2}CO + \frac{1}{2}H_2O \quad (54)$$

$$e^- + H^+ + \frac{1}{8}CO_2 \xrightarrow{k_1''} \frac{1}{8}CH_4 + \frac{1}{4}H_2O \quad (55)$$

$$e^- + H^+ + \frac{1}{7}CO_2 \xrightarrow{k_1'''} \frac{1}{14}C_2H_6 + \frac{2}{7}H_2O \quad (56)$$

$$h^+ + \frac{1}{2}H_2O \xrightarrow{k_2} H^+ + \frac{1}{4}O_2 \quad (57)$$

The main reverse semireactions are

$$h^+ + \frac{1}{2}CO + \frac{1}{2}H_2O \xrightarrow{k_{-1}'} H^+ + \frac{1}{2}CO_2 \quad (58)$$

$$h^+ + \frac{1}{8}CH_4 + \frac{1}{4}H_2O \xrightarrow{k_{-1}''} H^+ + \frac{1}{8}CO_2 \quad (59)$$

$$h^+ + \frac{1}{14}C_2H_6 + \frac{2}{7}H_2O \xrightarrow{k_{-1}'''} H^+ + \frac{1}{7}CO_2 \quad (60)$$

$$e^- + H^+ + \frac{1}{4}O_2 \xrightarrow{k_{-2}} \frac{1}{2}H_2O \quad (61)$$

The rate of the reactions can be expressed as a function of h (TiO_2 bed thickness)

$$r_{e^-}^{h\nu}(h) = k_0 E(h) \cdot C_s^{irr}(h) \quad (62)$$

$$r_{e^-}^{CO}(h) = k_1' n_{H^+}^{surf^1} \cdot n_{e^-}^{surf^1} \cdot n_{CO_2}^{surf^0} = K_1' \theta_{H^+} \cdot \theta_e \cdot C_s^{irr}(h)^2 \quad (63)$$

$$r_{e^-}^{CH_4}(h) = k_1'' n_{H^+}^{surf^1} \cdot n_{e^-}^{surf^1} \cdot n_{CO_2}^{surf^0} = K_1'' \theta_{H^+} \cdot \theta_e \cdot C_s^{irr}(h)^2 \quad (64)$$

$$r_{e^-}^{C_2H_6}(h) = k_1''' n_{H^+}^{surf^1} \cdot n_{e^-}^{surf^1} \cdot n_{CO_2}^{surf^0} = K_1''' \theta_{H^+} \cdot \theta_e \cdot C_s^{irr}(h)^2 \quad (65)$$

$$r_{e^-}^{O_2}(h) = k_{-2} n_{H^+}^{surf^1} \cdot n_{e^-}^{surf^1} \cdot n_{O_2}^{surf^{1/4}} = K_{-2} \theta_{H^+} \cdot \theta_e \cdot \theta_{O_2}^{1/4} \cdot C_s^{irr}(h)^{9/4} \quad (66)$$

Here, k, K, n_x^{surf}, and θ_x are the kinetic constant, apparent kinetic constant, amount of x species on the catalyst surface, and the surface coverage of x species on the catalyst surface.

https://dx.doi.org/10.1021/acsenergylett.9b02585
ACS Energy Lett. 2020, 5, 486–519

$$r_{e^-}(h) = \frac{k_0 E(h) C_s^{irr}(h)}{S^{irr}} \times \frac{K}{(K + E(h)^4)} \quad (67)$$

$E(h)$ was determined according to Beer–Lambert's law

$$E(h) = E^0 \times \int_0^h e^{-\alpha z} \cdot dz = E^0 \times \frac{(1 - e^{-\alpha h})}{\alpha} \quad (68)$$

The molar quantity of irradiated photocatalyst surface sites ($C_s^{irr}(h)$) was calculated as follows

$$C_s^{irr}(h) = C_s \times \int_0^h e^{-\alpha z} \cdot dz = C_s \times \frac{(1 - e^{-\alpha h})}{\alpha} \quad (69)$$

A microkinetic model was used to study the CO_2 EC reduction over Ag catalyst with the most active facet (110).[181] The adsorption/desorption of reactants and products on the catalyst surface were considered to develop the microkinetic model. The reduction of CO_2 on the Ag surface occurred through the following steps: (i) adsorption of CO_2 ($*CO_2$) and bonding of a carbon atom on the Ag(110) facet; (ii) activation of $*CO_2$ to create $*CO_2^-$; and (iii) reaction of $*CO_2^-$ with a hydrogen atom. Transition state theory was used to model the rate of surface reactions. The important cathode reactions for the CO_2 reduction on the Ag(110) facet are given below

$$CO_2 \xrightarrow{\text{Bulk diffusion \& Migration}} CO_2 \xrightarrow{\text{Boundry layer diffusion}} CO_2 \xrightarrow{\text{Adsorption}} *CO_2 \xrightarrow{\delta e^-} *CO_2^{\delta-} \xrightarrow{*(1-\delta)e^-} **COOH + OH^- \quad (70)$$

$$**COOH \xrightarrow{e^-,-*} *CO + H_2O + OH^- \quad (71)$$

$$*CO \xrightarrow{\text{Desorption}} CO \xrightarrow{\text{Boundry layer diffusion}} CO \quad (72)$$

$$H_2O \xrightarrow{\text{Bulk diffusion \& Migration}} H_2O \xrightarrow{\text{Boundry layer diffusion}} H_2O \xrightarrow{\text{Adsorption}} **H_2O \xrightarrow{e^-,-*} *H + OH^- \quad (73)$$

$$*H \xrightarrow{e^-} *H_2 + OH^- \xrightarrow{\text{Desorption},-*} H_2 \xrightarrow{\text{Boundry layer diffusion}} H_2 \quad (74)$$

$$OH^- \xrightarrow{\text{Boundry layer diffusion}} OH^- \xrightarrow{\text{Bulk diffusion \& Migration}} OH^- \quad (75)$$

Here, * and ** represent adsorption and two-fold coordination on the catalyst surface, respectively. Three different reaction mechanisms (I, II, and III) were considered on the basis of hydrogen donor groups such as *H, $*H_2O$, and free H_2O.

Reaction mechanism I: involvement of *H

$$*CO_2 + *H \underset{k_1}{\overset{k_{-1}}{\leftrightarrows}} **COOH \quad (76)$$

$$**COOH + *H \underset{k_2}{\overset{k_{-2}}{\leftrightarrows}} *CO + **H_2O \quad (77)$$

The rate of the above reactions (r) is expressed as follows

$$r_1 = k_1\left[\theta_{*CO_2}\theta_{*H} - \frac{1}{K_1}\theta_{**COOH}\right] \quad (78)$$

$$r_2 = k_2\left[\theta_{**COOH}\theta_{*H} - \frac{1}{K_2}\theta_{*CO}\theta_{**H_2O}\right] \quad (79)$$

where k and K are the rate constant and equilibrium constant, respectively. θ_x is the fractional coverage of x species on the catalyst surface.

Reaction mechanism II: involvement of $**H_2O$

$$*CO_2 + **H_2O + e^- \underset{k_1}{\overset{k_{-1}}{\leftrightarrows}} **COOH + * + OH^- \quad (80)$$

$$**COOH + **H_2O + e^- \underset{k_2}{\overset{k_{-2}}{\leftrightarrows}} *CO + **H_2O + * + OH^- \quad (81)$$

The rate of the above reactions (r) is expressed as follows

$$r_1 = k_1\left[\theta_{*CO_2}\theta_{**H_2O} - \frac{1}{K_1}\theta_{**COOH}\theta_*\chi_{OH^-}\right] \quad (82)$$

$$r_2 = k_2\left[\theta_{**COOH}\theta_{**H_2O} - \frac{1}{K_2}\theta_{*CO}\theta_{**H_2O}\theta_*\chi_{OH^-}\right] \quad (83)$$

Here, χ_{OH^-} denotes the mole fraction of OH^- at the cathode interface.

Reaction mechanism III: involvement of H_2O

$$*CO_2 + \delta e^- \underset{k_0}{\overset{k_{-0}}{\leftrightarrows}} *CO_2^{-\delta} \quad (84)$$

$$*CO_2^{-\delta} + * + H_2O + (1 - \delta)e^- \underset{k_1}{\overset{k_{-1}}{\leftrightarrows}} **COOH + OH^- \quad (85)$$

$$**COOH + H_2O + e^- \underset{k_2}{\overset{k_{-2}}{\leftrightarrows}} *CO + H_2O + * + OH^- \quad (86)$$

The rate of the above reactions (r) is expressed as follows

$$r_0 = k_0\left[\theta_{*CO_2} - \frac{1}{K_0}\theta_{*CO_2^{-\delta}}\right] \quad (87)$$

$$r_1 = k_1\left[\theta_{*CO_2^{-\delta}}\theta_* - \frac{1}{K_1}\theta_{**COOH}\chi_{OH^-}\right] \quad (88)$$

$$r_2 = k_2\left[\theta_{**COOH} - \frac{1}{K_2}\theta_{*CO}\theta_*\chi_{OH^-}\right] \quad (89)$$

The hydrogenation of $*CO_2$ into **COOH was the rate-determining step for CO production in all of the above cases. The energy barrier of **COOH formation was increased in the following order: RM-1 < RM-2 < RM-3. Species such as $*CO_2^{-\delta}$ and *H were mainly involved in the rate-limiting steps for CO and H_2 formation. At low negative potentials, $*CO_2^{-\delta}$ and **COOH were the dominating species. The reaction kinetics of CO formation were influenced by the electrolyte pH and the initial CO_2 concentration. The coverage of $*CO_2^{-\delta}$ species were nonlinearly increased with respect to the CO_2 concentration. The solubility of CO_2 and the local orientation of H_2O near the cathode were affected by the electrolyte pH.[215] The rate of the reaction was not significantly influenced

https://dx.doi.org/10.1021/acsenergylett.9b02585
ACS Energy Lett. 2020, 5, 486−519

at neutral pH. The efficiency of CO_2 reduction could be increased through the stabilization of $*CO_2^{-\delta}$ species at the grain boundaries.[216]

The thermodynamic/kinetic barriers and the successful utilization of photogenerated charge carriers are governed by the surface features of electrode material.

Recent Electrode Materials: Various materials such as semiconductor nanoparticles (e.g., TiO_2, ZnO, g-C_3N_4), metal−organic frameworks (MOFs), quantum dots, heterojunctions, supramolecular catalysts, Cu-based metals, and biological catalysts have been utilized for PEC CO_2 conversion. The successful utilization of photogenerated charge carriers is governed by the surface features of the electrode material. The adsorption and binding energy (BE) of reaction intermediates on the electrode surface is controlled by the particle size.[113] The efficiency and product selectivity of recent electrode materials for the PEC CO_2 conversion are shown in Table S1. The recent research works mainly focus on the design of the photoelectrode to produce a particular product from CO_2. Cu and carbon-based materials have gained much attention to replace the expensive noble metals. In most of the studies, PEC experiments have been conducted using a CO_2 gas ($CO_{2(g)}$)-saturated aqueous solution of bicarbonate. Several strategies have been employed to engineer the light-active electrode materials with unique electronic and structural properties to achieve high CO_2 conversion efficiency. The insights of some important electrode materials for the PEC CO_2 conversion into various products are briefly presented in this section.

CH_3CH_2OH Production: PEC CO_2 conversion to CH_3CH_2OH was studied using a type-II graphitic carbon nitride/zinc telluride (g-C_3N_4/ZnTe) heterojunction under simulated solar light irradiation.[217] The nanocomposite was synthesized by the hydrothermal method. The photocathode was fabricated on an ITO glass plate, and the CO_2 conversion experiments were performed using $CO_{2(g)}$-saturated 0.1 M $KHCO_3$. CH_3CH_2OH formation was monitored using NMR spectroscopy. Photocurrent measurements showed that the electron−hole separation was maximum on g-C_3N_4/ZnTe as compared to that on pure g-C_3N_4 and ZnTe. This was attributed to the formation of a p−n heterojunction in the nanocomposite. This was further confirmed by a peak shift in Raman spectroscopy. g-C_3N_4/ZnTe with 1:2 ratio displayed the highest CH_3CH_2OH yield (17.1 μmol cm^{-2} h^{-1} with 79.3% FE at −1.1 V) as compared to other electrode materials. There was no CH_3CH_2OH production on pure g-C_3N_4 and ZnTe. Scanning electrochemical microscopy (SECM) was utilized to investigate the charge transfer kinetics at the nanocomposite interface. According to the Butler−Volmer model

$$\ln(\kappa_{eff}) = -\ln k_e^0 - \alpha n f \eta \quad (90)$$

$$\kappa_{eff} = \kappa D_{diffusion}/r_T \quad (91)$$

$$f = nF/RT \quad (92)$$

Here, k_{eff} and k are the effective and apparent heterogeneous charge transfer rate constants, respectively. The charge transfer coefficient is represented as α, the number of electrons transferred at the interface is labeled as n, the diffusion coefficient of the redox probe is denoted as $D_{diffusion}$, r_T is the radius of the Pt electrode, η is the applied overpotential on the photoelectrode, F is the Faraday constant; R is the gas constant, and T is the temperature. The apparent rate constants of g-C_3N_4/ZnTe and ZnTe were determined to be 26.68×10^{-3} and 7.75×10^{-3} cm s^{-1}, respectively. The results showed that the charge transfer rate constant at the heterojunction is higher as compared to that for pure ZnTe. The adsorption energies of CO_2 on g-C_3N_4/ZnTe, pure g-C_3N_4, and pure ZnTe were studied by density functional theory (DFT) calculations. The adsorption configuration of CO and CO_2 on various materials are shown in Figure 13. The

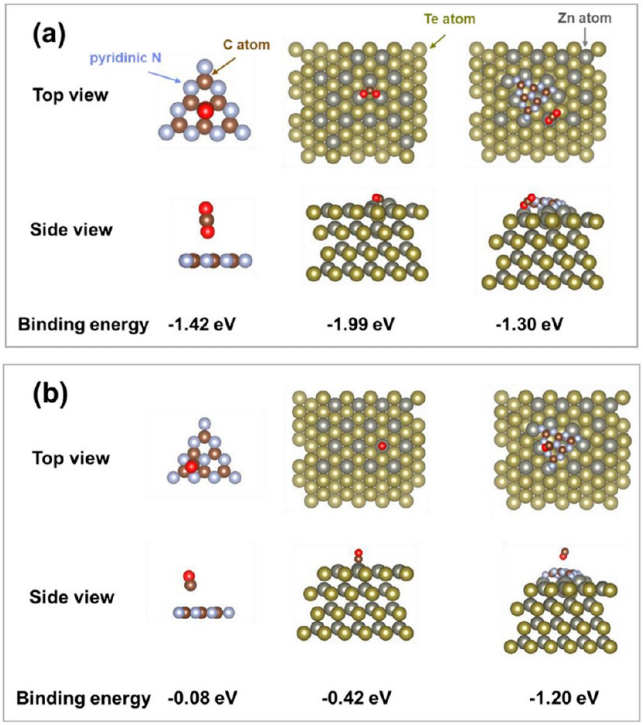

Figure 13. Adsorption models of (a) CO_2 and (b) CO on g-C_3N_4, ZnTe, and g-C_3N_4/ZnTe.[217] Reproduced with permission from ref 217. Copyright (2019), Elsevier.

results showed that the CO_2 adsorption BE on ZnTe was higher than that on the other materials. At the same time, the CO adsorption BE was maximum on g-C_3N_4 because of the pyridinic N sites. Consequently, ZnTe and g-C_3N_4 are the most suitable adsorption sites of CO_2 and CO at the nanocomposite. PEC CH_3CH_2OH production from CO_2 necessities the C−C coupling reaction. The mechanism proceeds through the following steps: (i) adsorption of CO_2 and on ZnTe; (ii) formation and transfer of CO from ZnTe; (iii) adsorption of CO on pyridinic N sites of g-C_3N_4; and (iv) C−C coupling reaction on g-C_3N_4 leading to the formation of CH_3CH_2OH via proton coupled electron transfer.

CH_3OH Production: PEC CO_2 conversion to CH_3OH was examined by a Zn phthalocyanine/g-C_3N_4 (ZnPc/g-C_3N_4) nanosheet heterojunction under visible light irradiation.[218] ZnPc/g-C_3N_4 was prepared by an evaporation−calcination technique in tetrahydrofuran solvent, and the working electrode was fabricated on an FTO glass plate. PEC experiments were carried out using $CO_{2(g)}$-saturated 0.1

https://dx.doi.org/10.1021/acsenergylett.9b02585
ACS Energy Lett. 2020, 5, 486−519

mol/L $KHCO_3$ in a two-compartment cell. Linear sweep voltammetry (LSV) measurements showed that the nanosheets with a ratio of 0.1% created the highest current. UV-diffuse reflectance spectroscopy (UV-DRS) results showed that the light absorption capacity of g-C_3N_4 was enhanced by the addition of ZnPc. Photoluminescence (PL) results demonstrated that the electron−hole recombination process in g-C_3N_4 was significantly minimized after coupling with ZnPc.

The observed current intensity of ZnPc/g-C_3N_4 (0.11×10^{-3} mA/cm^2) was much higher than that of pure ZnPc and g-C_3N_4. This was attributed to the high lifetime and quantity of photoinduced charge carriers at the heterojunction. The energy band of ZnPc matches well with that of g-C_3N_4, indicating faster electron transfer. Moreover, the PEC CO_2 conversion efficiency of ZnPc/g-C_3N_4 was 2.6 and 5.9 times higher as compared to its electrocatalytic and photocatalytic efficiency, respectively. The highest CH_3OH yield of 13 μmol/cm^2 was observed at −1.0 V in 8 h. The six-electron transfer process for the PEC CO_2 conversion to CH_3OH using ZnPc/g-C_3N_4 is shown in Figure 14. The active center of the heterojunction for CO_2 adsorption was the Zn(II) metal ion. The various products formed during the proton coupled electron transfer reactions were represented as P1, P2, P3, P4, P5, and P6. At first, CO_2^- was selectively adsorbed on ZnPc through the Zn−O bond (denoted as P1). The high electron cloud density of the carbon atom in the −C−O−Zn bond is favorable for the reaction with H^+.

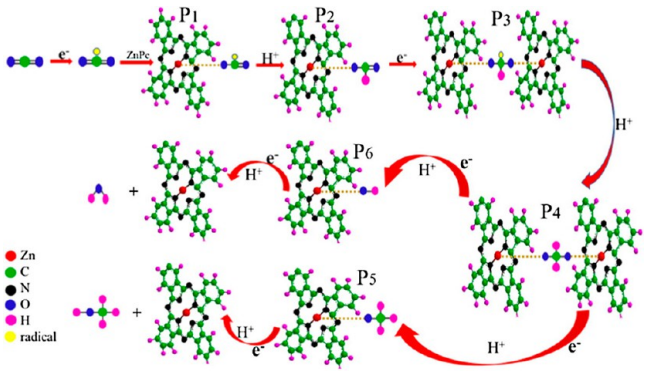

Figure 14. Mechanism for the six-electron transfer process for the PEC CO_2 conversion to CH_3OH using ZnPc/g-C_3N_4.[218] Reproduced with permission from ref 218. Copyright (2019), Elsevier.

In another study, PEC CO_2 conversion to CH_3OH was studied using a Cu^+ incorporated TiO_2 layer on a copper oxide nanowire (Cu_2O/TiO_2−Cu^+) photocathode on an FTO glass plate.[219] The experiments were carried out using a $CO_{2(g)}$-saturated 0.3 M $KHCO_3$ solution in a three-electrode system. The fabrication process, scanning electron microscopy (SEM), and transmission electron microscopy (TEM) images of the Cu_2O/TiO_2−Cu^+ photocathode are shown in Figure 15.

At first, Cu_2O nanowires were synthesized via thermal annealing, and then, TiO_2 was coated through the dip coating method. Finally, Cu^+ was incorporated by immersing preannealed Cu_2O/TiO_2 nanowires in a mixture of copper chloride, sodium hydroxide, and CH_3CH_2OH solution. The results revealed that the shape of the Cu_2O nanowires was not modified after coating with TiO_2 and incorporation of Cu^+. The photocurrent density of pure Cu_2O (p-type semiconductor) was dropped from 2.8 to 0.045 mA/cm^2 after 30 min of light chopped irradiation. This was ascribed to the

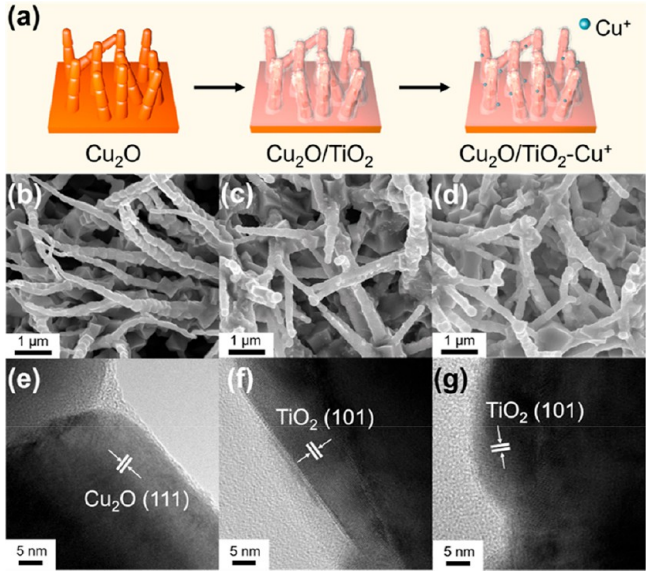

Figure 15. (a) Schematic of the fabrication process Cu_2O/TiO_2−Cu^+, (b) SEM of Cu_2O, (c) SEM of Cu_2O/TiO_2, and (d) SEM of Cu_2O/TiO_2−Cu^+. (e) TEM of Cu_2O, (f) TEM of Cu_2O/TiO_2, and (g) TEM of the Cu_2O/TiO_2−Cu^+ photocathode.[219] Reproduced with permission from ref 219. Copyright (2018), Elsevier.

photocorrosion of Cu_2O. It could be minimized by coating with a n-type semiconductor (TiO_2). The selectivity of the photocathode for CH_3OH production was enhanced by Cu^+ incorporation. TiO_2 would also play a significant role in increasing the band bending in Cu_2O. The operation potential for CH_3OH production was fixed at 0.3 V to improve the product selectivity and FE. The CH_3OH production efficiencies of Cu_2O and Cu_2O/TiO_2−Cu^+ were 0.14 and 0.26 μmol during 30 min of light irradiation. CH_3OH production was increased with respect to the irradiation time for Cu_2O/TiO_2−Cu^+. In the case of Cu_2O, there was no remarkable increase in CH_3OH production under prolonged light irradiation. The FEs of Cu_2O and Cu_2O/TiO_2−Cu^+ after 2 h at 0.3 V were 23.6 and 56.5%, respectively.

An octahedral metal MOF cathode was investigated for the selective conversion of CO_2 to alcohols.[220] Cu-BTC was used as a MOF, and it was synthesized through the hydrothermal method. The samples were further doped with palladium (Pd) and carbonized under a N_2 atmosphere. The cathodes were fabricated on a Cu foam using the drop-dry method. Platinum-doped TiO_2 (Pt−TiO_2) nanotubes were used as the photoanode. Sulfuric acid (0.5 M) and $NaHCO_3$ (0.5 M) were used as the anolyte and catholyte, respectively. The product yield was calculated as follows

$$\text{Carbon atom conversion rate} = \frac{M_p \times n_p}{t \times A} \tag{93}$$

where M_p is the Moore amount of the product, n_p is the number of carbon atoms in one molecule of product, t is the reaction time, and A is the area of the working electrode. The average size of Pd/Cu-BTC (~500 nm) was reduced after carbonization (size of C−Pd/Cu-BTC ~ 250 nm). The octahedral morphology was beneficial in improving the current density and product yield.[221] Fractal dimension analysis revealed that C−Pd/Cu-BTC has more pores on its surface compared to Pd/Cu-BTC. The porous structure was advantageous to promote mass transfer during the PEC reaction.

https://dx.doi.org/10.1021/acsenergylett.9b02585
ACS Energy Lett. 2020, 5, 486−519

The reaction pathways of CH_3OH and HCOOH formation were investigated through DFT calculations. The adsorption of CO_2 on the catalyst surface at various positions (hole, top, and bridge) was considered for the BE calculations. The BE of CO_2 adsorption on the Pd/Cu-BTC surface is displayed in Figure 16. The BE of CO_2 adsorption (BE_{CO2}) for the C-hole

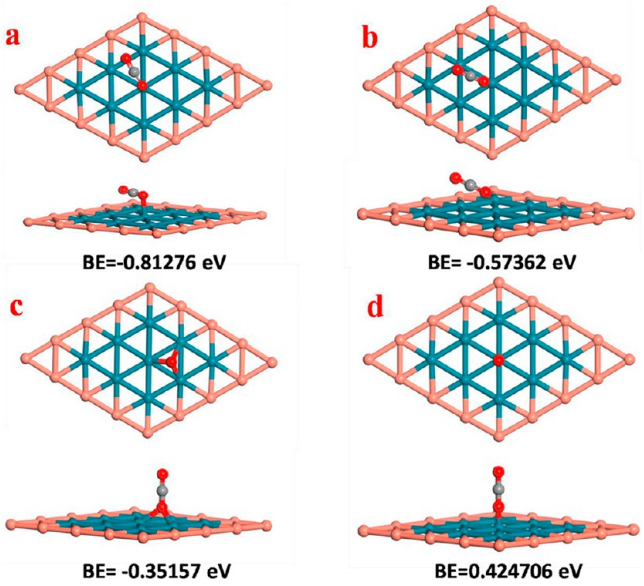

Figure 16. BE values of CO_2 adsorption at the (a) C-hole position, (b) C-bridge position, (c) O-hole position, and (d) O-top position on the catalyst surface.[220] Reproduced with permission from ref 220. Copyright (2019), Elsevier.

position, C-bridge position, O-hole position, and O-top position configurations was determined as follows

$$BE_{CO_2} = E_{slab+CO_2} - E_{slab} - E_{CO_2} \quad (94)$$

where E_{slab} and E_{CO_2} are the total energy of the optimized slab and optimized CO_2, respectively. BE values of CO_2 adsorption at the C-hole position, C-bridge position, O-hole position, and O-top position configurations were −0.81276, −0.57362, −0.35157, and 0.424706 eV, respectively. The relative free energies for the production of COOH*, HCOOH, CO*, CHO*, COH*, OCH_2*, HCOH*, CH_2OH*, and CH_3OH were −72.8, −155.4, −174.9, −225.5, −230, −303.6 eV, −307.5, −395, and −491.8 eV, respectively. The conversion of COOH* to HCOOH and CO* was the key step to produce acid and alcohol. The energy required to produce HCOOH was lower than that of CO*. Consequently, the product selectivity of C−Pd/Cu-BTC was higher for alcohol compared to that for HCOOH. PEC experiments revealed that the carbon conversion rate of C−Pd/Cu-BTC reached 2380 nmol/h/cm^2 with 93.2% liquid product selectivity. The yield of alcohol products was 2217.8 nmol/h/cm^2 including CH_3OH, CH_3CH_2OH, and $CH_3CH_2CH_2OH$.

CO Production: PEC CO_2 conversion was examined using porous zinc oxide/zinc selenide (ZnO@ZnSe) nanosheet arrays.[222] $NaHCO_3$ (0.5 M) was used as the electrolyte, and the experiments were carried out under visible light irradiation. The nanosheet was fabricated on an FTO glass plate via the dissolution−recrystallization technique. The schematic representation of ZnO@ZnSe nanosheet array fabrication on the FTO plate is displayed in Figure 17. ZnO was the seed layer,

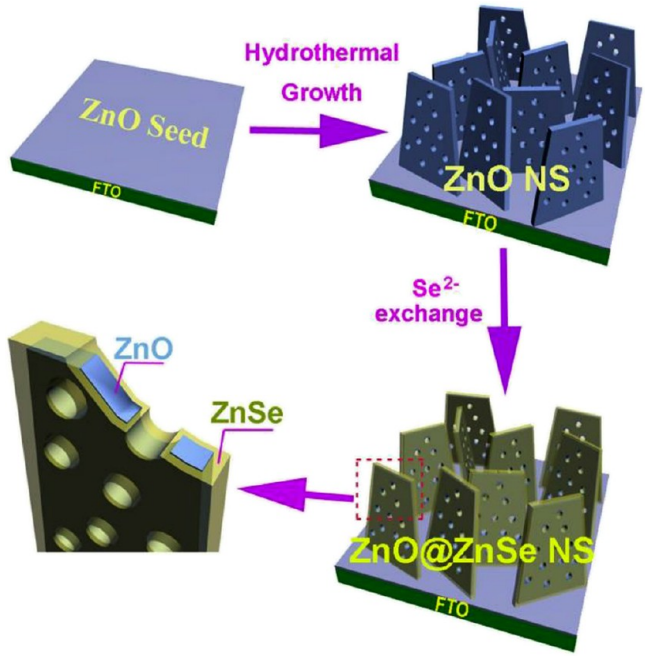

Figure 17. Schematic representation of the preparation of ZnO@ZnSe nanosheet arrays on FTO.[222] Reproduced with permission from ref 222. Copyright (2018), Elsevier.

and it was used as the template for ZnSe growth through the anion exchange method. The samples were prepared at various growth times of ZnO, such as 5, 10, and 20 h (the anion exchange time was kept constant at 3 h). There were no remarkable changes in the height of nanosheet arrays after 5 h. The nanosheet arrays were grown perpendicularly with a height of ∼20 μm.

The chopped LSV was measured in $NaHCO_3$ electrolyte saturated with $CO_{2(g)}/N_{2(g)}$. The observed onset potential of the ZnO@ZnSe photocathode (0.39 V (vs RHE)) was higher than that of ZnO (0.013 V (vs RHE)) in $CO_{2(g)}$-saturated electrolyte. Nevertheless, the current density was slightly lower as compared to $N_{2(g)}$-saturated electrolyte. This was attributed to the competition between CO_2 conversion and H_2 evolution reactions. Generally, N_2 purging was kinetically and thermodynamically more suitable for H_2 evolution reaction. Moreover, the reaction kinetics of CO_2 reduction is slower than that of H_2 evolution. The photocurrent density of ZnO@ZnSe was gradually increased with the increase of applied potential during light on/off cycles (Figure 18a). The photocurrent densities of ZnO-5@ZnSe, ZnO-10@ZnSe, and ZnO-15@ZnSe samples at −0.11 V were 0.48, 1.17, and 1.12 mA/cm^2, respectively (Figure 18b). The photocurrent density was also increased with respect to the anion exchange time (Figure 18c) from 1 h (0.85 mA/cm^2) to 3 h (1.17 mA/cm^2), and it was slightly decreased during 6 h (1.10 mA/cm^2). This was attributed to the formation of recombination centers from surface defects at high ZnSe concentration. On the basis of the photocurrent measurement, PEC CO_2 conversion was evaluated for the best sample (ZnO-10@ZnSe). The results for PEC activity of ZnO-10@ZnSe are shown in Figure 18d.

CO production was increased when the applied voltage was more negative. H_2 was the main product at the positive voltage. The FE of CO production was increased from 4.2 to 52.9% as the applied potential was varied from 0.2 to −0.4 V. CH_4 yield was not remarkable as compared to CO yield. This was

https://dx.doi.org/10.1021/acsenergylett.9b02585
ACS Energy Lett. 2020, 5, 486−519

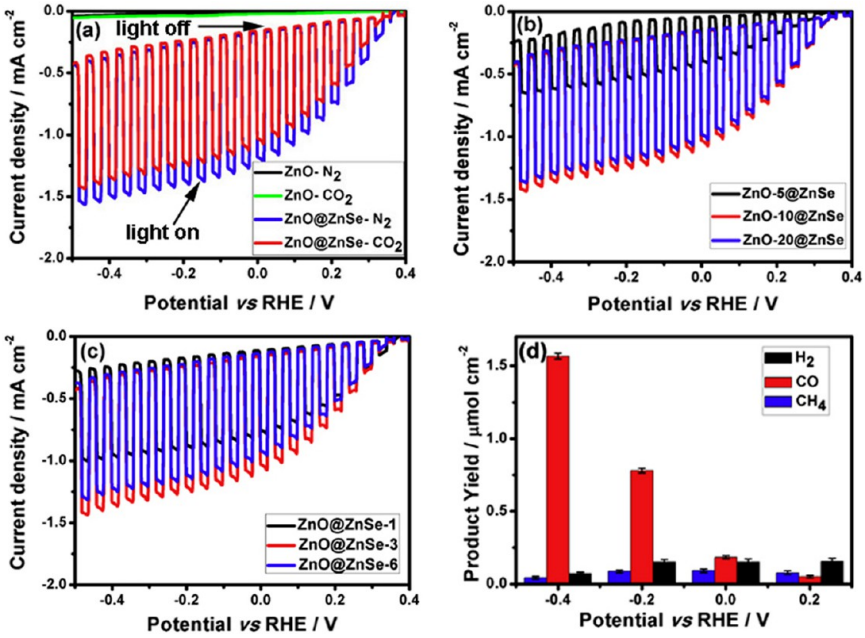

Figure 18. (a) Chopped LSV responses of ZnO and ZnO@ZnSe in $NaHCO_3$ electrolyte saturated with $CO_{2(g)}/N_{2(g)}$. (b) Photocurrent measurements of ZnO-5@ZnSe, ZnO-10@ZnSe, and ZnO-20@ZnSe. (c) Photocurrent measurements of ZnO@ZnSe-1, ZnO@ZnSe-3, and ZnO@ZnSe-6. (d) PEC CO_2 conversion efficiency of ZnO-10@ZnSe-3 at various applied potentials for 1 h.[222] Reproduced with permission from ref 222. Copyright (2018), Elsevier.

ascribed to the selectivity of CO_2 adsorption on the photoelectrode, competitive H_2 evolution reaction, and slow kinetics of the multiple electron transfer process. Moreover, the stability and efficiency of the photoelectrode was further improved by doping with a co-catalyst. The photocurrent response of Au-doped ZnO@ZnSe was 1.29 mA/cm^2 at −0.11 V.

In a similar study, PEC product selectivity of CO_2 conversion was investigated using a nickel oxide (NiO) photocathode with cadmium selenide (CdSe) quantum dots (QDs).[223] The electron transfer kinetics of CO_2 conversion was controlled by the size-tunable CdSe QDs. The photocathode was prepared by coating NiO on FTO glass plates via the doctor blade method. CdSe QDs were deposited through the electrophoretic deposition technique. Oleic acid (OA) and mercaptopropionic acid (MPA) were used as surface ligands between NiO and CdSe QDs. PEC experiments were performed using $CO_{2(g)}$-saturated 0.1 M $KHCO_3$ electrolyte in a three-electrode system. The number of absorbed photons was increased with respect to the size of QDs. Moreover, the photocurrent density was also influenced by the size of QDs.

The product selectivity was determined as follows

$$\text{Product selectivity} = \frac{\text{Amount of electrons required for a particular product}}{\text{Total amount of electrons consumed for } CO_2 \text{ reduction}} \quad (95)$$

The selectivity of CH_4 and CO formation was increased when the sizes of the QDs were increased. Consequently, the electron transfer kinetics play a key role in the product selectivity. An Auger-assisted model was used to investigate the electron transfer rate from QDs to the electrolyte.[224]

$$k_{AET}(R) = C|\psi_{1Se}(R)_0|^2 R^2 \int_{E_h=0}^{\infty} dE_h\, E_h \frac{2\pi}{\hbar} \frac{1}{\sqrt{4\pi\lambda k_B T}} \exp\left[-\frac{(\lambda + \Delta G(R) + E_h)^2}{4\lambda k_B T}\right] \quad (96)$$

$$k'_{AET}(\Delta G) = \frac{k_{AET}(R)}{C|\psi_{1Se}(R)_0|^2 R^2} = \int_{\infty}^{E_h=0} dE_h\, E_h \frac{2\pi}{\hbar} \frac{1}{\sqrt{4\pi\lambda k_B T}} \exp\left[-\frac{(\lambda + \Delta G(R) + E_h)^2}{4\lambda k_B T}\right] \quad (97)$$

The above equations demonstrate that the thermodynamic driving force of electrons (ΔG) rules the electron transfer rate constant. ΔG was calculated from the CB level and redox potential of products. The results showed that as the size of QDs increases the ΔG value decreases. This was ascribed to the variations in the photocurrent response.

A supramolecular catalyst (RuReP/NiO and RuReP/$CuGaO_2$ photocathode) was examined for CO_2 conversion under visible light irradiation.[225] CoO_x/TaON was used as the photoanode. The Ru(II)−Re(I) supramolecular catalyst was immobilized on the NiO electrode by anchoring of methyl phosphonic acid (P) and EC polymerization of vinyl groups (Figure 19). EC polymerization (poly) is favorable to adsorb a more electroactive metal complex on the cathode surface. PEC experiments were carried out in $CO_{2(g)}$-saturated 50 mM $NaHCO_3$. A schematic of the electron transfer mechanism and the PEC CO_2 conversion on the supramolecular photocatalyst are shown in Figure 20. The Z-scheme mechanism was involved in the photogenerated electron transfer. CO and O_2 were produced at the photocathode and photoanode, respectively, via a systematic photon absorption process. The photocurrent response of poly-RuRe/NiO (having both

https://dx.doi.org/10.1021/acsenergylett.9b02585
ACS Energy Lett. 2020, 5, 486−519

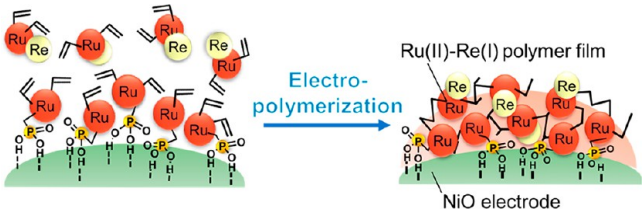

Figure 19. Schematic of supramolecular photoelectrode preparation through electropolymerization.[225] Reproduced with permission from ref 225. Copyright (2019), American Chemical Society.

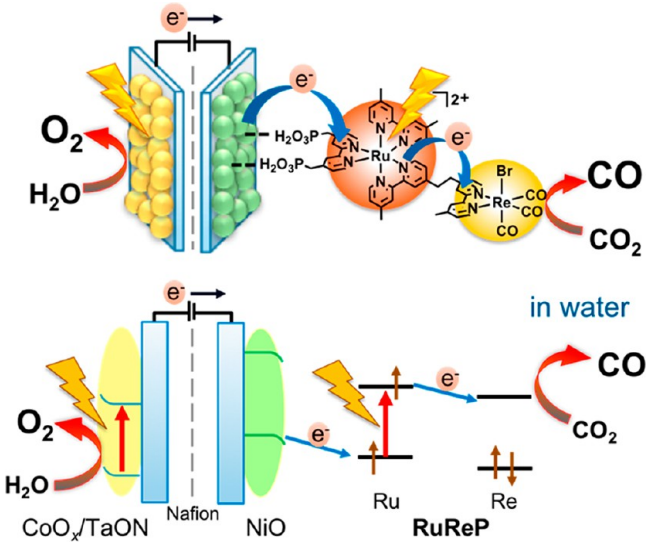

Figure 20. Schematic of the electron transfer mechanism involved in the PEC CO_2 conversion to CO on the supramolecular catalyst.[225] Reproduced with permission from ref 225. Copyright (2019), American Chemical Society.

polymer and phosphonic acid) was around 2 times higher than that of RuReP/NiO (having only phosphonic acid).

CO (507 nmol) was detected with HCOOH and H_2 byproducts during 5 h of PEC reaction using poly-RuRe/NiO. The CO formation efficiency of poly-RuRe/NiO was higher than that of RuReP/NiO (210 nmol). The FE of poly-RuRe/NiO and RuReP/NiO was 85 and 57%, respectively. The improvement in efficiency of poly-RuRe/NiO was ascribed to the increase of the active electrode surface area and the strong adherence of photoactive metal complexes on the electrode surface. CO was not produced using bare NiO, poly-Ru/NiO, and poly-Re/NiO. Therefore, both the Ru and Re complexes are necessary for the PEC CO_2 conversion.

Biocathode: The application of microbes or enzymes with electrode material for CO_2 conversion is attracting a lot of attention in recent days.[226] The combination of electrodes with suitable biological molecules could minimize the requirement of a high overpotential.[227] The reactions could be carried out at very low overpotential or without an external bias.[227,228] In a recent study, a solar light-driven hybrid microbial PEC system was tested for the selective conversion of CO_2 into CH_4 without any byproducts.[226] The working principle of a solar light-driven hybrid microbial PEC system is schematically illustrated in Figure 21. The reactor was made up of PMMA, and the reactions were carried out under simulated solar light (a 300 W Xe lamp with an AM 1.5G filter). The anode (450 mL of 0.2 mol/L potassium hydroxide) and cathode

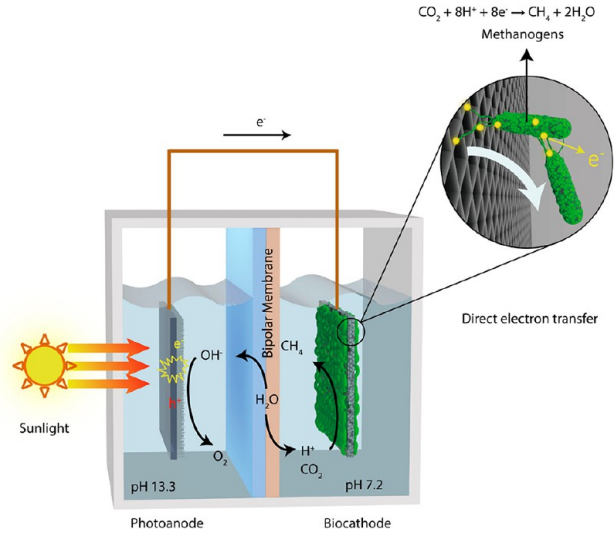

Figure 21. Schematic of the working principle of a solar light-driven hybrid microbial PEC system.[226] Reproduced with permission from ref 226. Copyright (2018), Elsevier.

compartments (450 mL of presterilized anaerobic medium) were separated via a bipolar membrane. The headspace (~150 mL) of the system was replenished with pure CO_2 gas. A TiO_2 nanowire array was used as the photoanode. The biocathode was cultivated in an electromethanogenesis reactor using anaerobic activated sludge collected from a municipal wastewater treatment plant.

A thick biofilm was formed on the cathode surface after microbial cultivation. Phylogenetic analysis revealed that the archaeal population was mostly predominated by an operational taxonomic unit (OTU) associated with a *methanobacteriaceae* family microbe (a hydrogenotrophic methanogen). Furthermore, *actinobacteria* (*coriobacteriaceae*) was identified as the most abundant species. The average rate of CH_4 production in the solar light-driven hybrid microbial PEC system was 192 ± 3.6 μL/day/cm^2 with an average FE of 95.2 ± 1.8%. Besides, the performance of the electrodes was sustained well after 90 h of operation cycles. The stability of the biocathode was also examined for 252 days at a fixed potential (−0.5 V vs SHE). A stable current was produced in the range of −0.6 to −1.2 mA, indicating the long-term stability of the biocathode. STF could be further intensified by developing new visible light-active photoanode materials.

In another study, 3D titanium nitride with *clostridium ljungdahlii* (3D TiN−ClFDH) enzyme was used as the biocathode for the electroenzymatic conversion of CO_2 into formate through the direct electron transfer (DET) process.[227] The experiments were conducted in a Z-scheme-inspired tandem PEC reactor using $CO_{2(g)}$-saturated sodium phosphate buffer solution under visible light irradiation. The schematic representation the of 3D TiN−CIFDH nanoshell morphology and the bias-free PEC reactor design are displayed in Figure 22. 3D TiN was used as a scaffold to provide high electrical conductance (6.72×10^4 S m^{-1}), stability, and an electroactive surface area.

TiN was coated on the template by the atomic layer deposition (ALD) technique. The porous nanoshell morphology was highly favorable for the maximum loading of enzymes, the facile transportation of chemicals, and the immobilization of enzyme via electrostatic interaction. ClFDH was coated on

https://dx.doi.org/10.1021/acsenergylett.9b02585
ACS Energy Lett. 2020, 5, 486−519

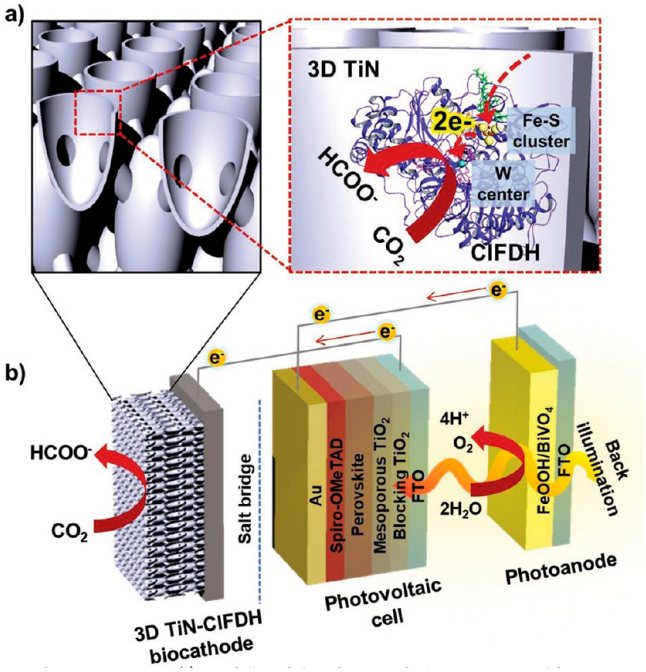

Figure 22. Schematic representation: (a) nanoshell morphology of 3D TiN with ClFDH conjugation and the DET process from 3D TiN to ClFDH for the conversion of CO_2 into formate; (b) design of the tandem PEC reactor with a photoanode, PV cell, and biocathode.[227] Reproduced with permission from ref 227. Copyright (2019), John and Wiley Sons.

3D TiN by the drop-casting method. The pores were interconnected to contribute a continuous electron transfer network from 3D TiN to the enzyme. The wall thickness and porosity of the 3D TiN nanoshell were tuned by changing the number of ALD cycles. The porosity was decreased (92.1 to 54.1%) and the wall thickness (30.3 to 131 nm) was increased as the ALD cycles increased from 300 to 1300. CO_2 intermediates were stabilized by the enzyme amine groups at the active sites of the catalyst. The DET process in ClFDH was confirmed by the protein film cyclic voltammeter. The number of electrons involved in the electroenzymatic conversion of CO_2 into formate was found to be 1.85, which was much closer to the theoretical value of 2, confirming the DET. The 3D TiN−ClFDH biocathode with a thickness of 30 nm showed the highest current density of 0.31 mA/cm^2 at −0.86 V. The surface coverage of the 3D TiN−ClFDH biocathode was increased with an increase of wall thickness, whereas the corresponding TOF was decreased. This was ascribed to the changes in distance between the active sites of the enzyme and electrode surface. The charge transfer coefficient (α), kinetic rate constant (k_s), and electron transfer rate (K_{et}) were calculated as follows

$$\alpha = \frac{-2.3RT}{bnF} \tag{98}$$

$$k_s = \frac{\alpha F \nu^{0.5} D^{0.5}}{RT} e^{[-(RT/\alpha F)(E^\circ - E_{pc}) + 0.78]} \tag{99}$$

$$K_{et} = \frac{j_0}{nFc} \tag{100}$$

Here, n, F, b, and c represent the number of electrons transferred, the Faraday constant, the Tafel slope, and the concentration of CO_2, respectively. ν denotes the scan rate. D indicates the diffusion coefficient of CO_2 in water. E° and E_{pc} are the standard electrode potential and cathode peak potential, respectively. The k_s value of 3D TiN−ClFDH was higher than that of pure 3D TiN. The K_{et} value of 3D TiN−ClFDH was 25.7 times higher as compared to that of flat TiN−ClFDH. The formate production rates of 3D TiN, 3D TiN−ClFDH, flat TiN−ClFDH, and TiN−ClFDH (nanotubes) were 0.11, 1.74, 0.03, and 0.62 μmol/h/cm^2, respectively. The high efficiency was attributed to the porous nanoshell morphology of TiN and the DET process between the enzyme and TiN. Moreover, 3D TiN−ClFDH showed an average formate production rate of 0.78 μmol/h/cm^2 (FE 77.3%) using the PEC tandem cell without an external bias.

2D Materials: Several efforts have been made to improve the efficiency of materials for PEC/electrocatalytic CO_2 conversion.[229−232] In this regard, 2D materials (e.g., nanosheets, nanoflakes) have attracted much attention in recent years, owing to their tunable electronic properties, large number of surface active sites, and dangling bonds.[87,121,229,233−236] Interestingly, some metals have been particularly investigated for formate (e.g., Sn, Pb, In),[237,238] carbon monoxide (e.g., Pd, Au, Zn, Ag),[239−241] and hydrocarbon (e.g., Cu) products.[229,242] The exposed surface atoms of the nanosheets could form vacancy-type defects.[208] The atomic and surface defect engineering (e.g., cation/anion vacancy, pits, crystal distortion, and creation of oxygen vacancies) of nanomaterials with finite dimensions (2D and 3D) directly influences their optical, structural, and electronic properties.[243] The defects can act as active sites during photocatalysis reaction; they can also optimize the adsorption and activation of molecules.[243] According to DFT calculations, the oxygen vacancy defects are responsible for n-type conductivity (shallow donors). Metal vacancy defects contribute to p-type conductivity (shallow acceptors). The surface defects in 2D/3D materials could improve the photocatalytic activity when compared to bulk defects.[243] The exposed active sites could promote the chemisorption of reactants and interfacial charge transfer, leading to an increase in activity.[87,244] There are various 2D materials such as metal oxides,[245−247] LDHs,[248−250] perovskites,[42,251−253] metal dichalcogenides,[254−257] MXenes,[258,259] nonmetals (e.g., carbon- and graphene-based materials),[200,260−262] MOFs,[263−266] and metals[267−273] that have been utilized as electrodes for electrocatalytic/PEC CO_2 conversion.[274,275] The performance of 2D materials could be improved through various ways, like band gap alterations, surface engineering (such as defects, high-index crystal facets, morphology, doping, interlayer architectonics, size or thickness control, and formation), and heterostructure fabrication.[121] These techniques are favorable to amplify the number of active sites, adsorption energy, and conductivity of 2D materials.[121,229] The key findings of some important 2D materials for the CO_2 conversion are briefly listed in this section.

The electrocatalytic reduction of CO_2 using 2D metal-doped hexagonal boron nitride monolayers (such as *h*-BN/Cu, *h*-BN/Ni, and *h*-BN/Co) was examined by DFT calculations.[276] The calculations were performed by the Vienna ab initio simulation package. The electrical conductivity of *h*-BN monolayers could be improved by transition metal doping. The geometry, electronic structure, and BEs of key intermediates were investigated in detail. The top and side views of the optimized structures of metal-doped *h*-BN are shown in Figure 23. DFT-PBE-D3 geometry optimizations revealed that the most

https://dx.doi.org/10.1021/acsenergylett.9b02585
ACS Energy Lett. 2020, 5, 486−519

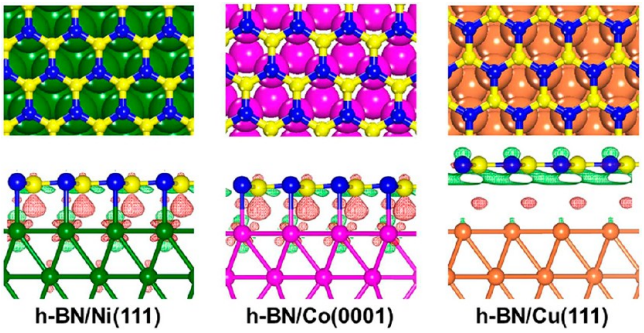

Figure 23. Top and side views of the optimized structures of metal-doped *h*-BN.[276] Reproduced with permission from ref 276. Copyright (2018), American Chemical Society.

appropriate configuration of *h*-BN on the metal surfaces was the N atom on the top site and B on the fcc hollow site.[277,278] The distances between the *h*-BN monolayer and the first layer of metal were 3.02 Å (*h*-BN/Cu), 2.18 Å (*h*-BN/Ni), and 2.14 Å (*h*-BN/Co). The product selectivity was governed by the adsorption of intermediates such as H, HCOO, and HCOOH on the *h*-BN/metal interface. The electrons at the interface between *h*-BN and the metal layer played a key role in the electrocatalysis. The interfacial BE of Cu per BN unit (−0.16 eV) was weakest when compared to Ni (−0.25 eV) and Co (−0.34 eV). Consequently, the adsorption of H and COOH on *h*-BN/Cu was quite unfavorable. Nevertheless, the adsorption of HCOO on *h*-BN/Cu was favorable but not strong as compared to that of *h*-BN/Ni and *h*-BN/Co. As compared to *h*-BN/Cu, the efficiency of *h*-BN/Ni and *h*-BN/Co would be higher for the electrocatalytic reduction of CO_2 to HCOOH.

Cu catalyst (metallic Cu, CuO, and Cu_2S) nanoparticles dispersed on a graphene nanoflake (GNF) electrocatalyst were designed for the selective conversion of CO_2 to formate.[279] GNFs were synthesized through the thermal plasma method. The chemical precipitation method followed by pyrolysis was utilized to disperse the Cu catalyst on GNFs. The electrocatalyst was prepared with various weight percentages of Cu (20, 30, 40, and 50 wt %; the samples are labeled as Cu-GNF1, Cu-GNF2, Cu-GNF3, and Cu-GNF4). The structure was typically composed of 5−20 atomic layers of stacked graphene with around 100 nm of lateral dimensions. Electrocatalytic experiments were carried out using a $CO_{2(g)}$-saturated 0.1 M $KHCO_3$ aqueous solution. Formate and *n*-propanol were identified as the main products during CO_2 electrocatalytic reduction using Cu-GNFs. The strong interaction of CuO with GNFs was the key rationale for the selectivity of *n*-propanol.[280] The formation of products and performance of Cu-GNFs during the electrocatalytic CO_2 conversion are illustrated in Figure 24. The results suggested that the efficiency of catalysts was not dependent on the amount of Cu catalyst. A high FE of 40% toward formate production was demonstrated by Cu-GNF2 at a potential of −0.6 V vs RHE. The high efficiency of Cu-GNF2 was accredited to the existence of Cu_2S nanoparticles. Nevertheless, the efficiency was decreased at a high concentration of Cu_2S in the electrocatalyst.

2D Fe- and N-codoped sandwich-like porous carbon nanosheets were studied for the electrocatalytic reduction of CO_2 to CO.[281] The electrocatalyst was synthesized using a MOF (such as Fe/Zn bimetallic zeolitic imidazolate framework-8 (ZIF)), polymer mediator (such as polyvinylpyrrolidone (PVP) or poly(ether imide) (PEI)), and graphene oxide (GO). The carbonization of GO-PVP-ZIF (rGO-PVP-ZIFc) was carried out at 950 °C under an Ar atmosphere. The synthetic procedure, SEM, TEM, and high-angle annular dark-field imaging (HAADF) scanning transmission electron microscopy (STEM) images of rGO-PVP-ZIFc are displayed in Figure 25. The morphology and size of rGO-PVP-ZIF were verified by SEM and TEM analysis. ZIF was homogeneously dispersed on the GO surface. The carbonization process did not disrupt the morphology of GO-PVP-ZIF. The size of ZIF was slightly decreased, and macro/mesopores were created during the carbonization. The amide groups of PVP on the surface of GO were supportive to coordinate the Zn ions of ZIF. For PEI, tubular and quasi-spherical nanostructures were observed after the calcination process. The surface area of

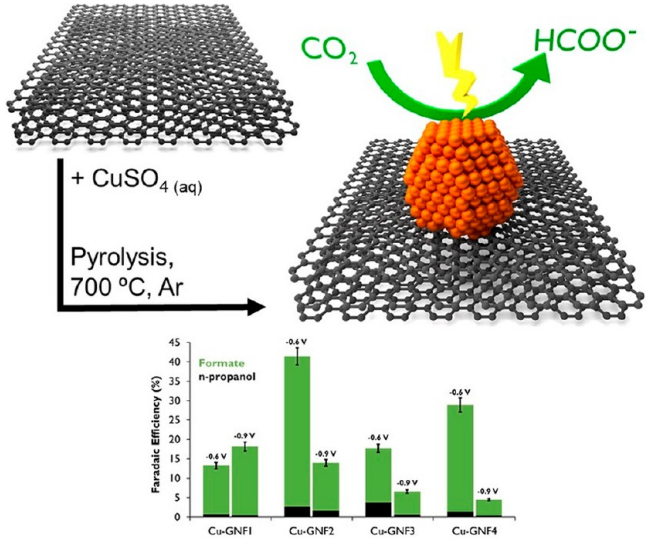

Figure 24. FE of Cu-GNFs toward formate and *n*-propanol formation during CO_2 electroreduction.[279] Reproduced with permission from ref 279. Copyright (2019), Elsevier.

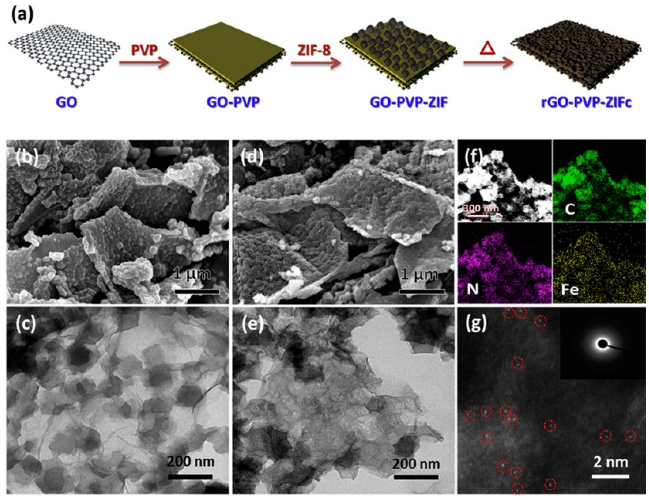

Figure 25. (a) Schematic representation of rGO-PVP-ZIF-derived carbon synthesis. (b) SEM of GO-PVP-ZIF. (c) TEM of GO-PVP-ZIF. (d) SEM of rGO-PVP-ZIFc. (e) TEM of rGO-PVP-ZIFc. (f) HAADF-STEM and elemental mapping of rGO-PVP-ZIFc. (g) Magnified HAADF-STEM of rGO-PVP-ZIFc.[281] Reproduced with permission from ref 281. Copyright (2019), Elsevier.

https://dx.doi.org/10.1021/acsenergylett.9b02585
ACS Energy Lett. 2020, 5, 486−519

rGO-PVP-ZIFc (678.2 m^2 g^{-1}) was higher than that of rGO-PEI-ZIFc (580.5 m^2 g^{-1}).

The electroreduction experiments were executed using a $CO_{2(g)}$-saturated 0.5 M $KHCO_3$ aqueous solution. The observed CO current density of rGO-PVP-ZIFc at −0.72 V was 20 and 5 times higher as compared to those of rGO-ZIFc and rGO-PEI-ZIFc, respectively. The FEs of rGO-PVP-ZIFc, rGO-PEI-ZIFc, and rGO-ZIFc for CO formation at −0.62 V vs RHE were noted as 98.6, 78.5, and 49.8%, respectively. The maximum efficiency of rGO-PVP-ZIFc was ascribed to the hierarchical porous morphology, high specific capacitance, a greater number of exposed Fe−N active sites, and the strong interaction among PVP, rGO, and Fe−N sites. A slight decay in the FE (98%) was observed for rGO-PVP-ZIFc during 8 h of electrolysis experiment.

In a recent study, a layered hybrid heterojunction of in situ-grown TiO_2 on 2D titanium carbide (Ti_3C_2) nanosheets (TiO_2/Ti_3C_2) was employed as the photocathode for the CO_2 conversion.[282] The TiO_2/Ti_3C_2 heterojunction was functionalized with imine ligands and Pd nanoparticles on an FTO glass plate ($Pd/N-TiO_2/Ti_3C_2/FTO$) to enhance efficiency. The role of the NADP and CO_2 absorber in the Calvin cycle of plant photosynthesis was mimicked by Pd nanoparticles and imine ligands. The schematic representation of $Pd/N-TiO_2/Ti_3C_2/FTO$ electrode synthesis is illustrated in Figure 26.

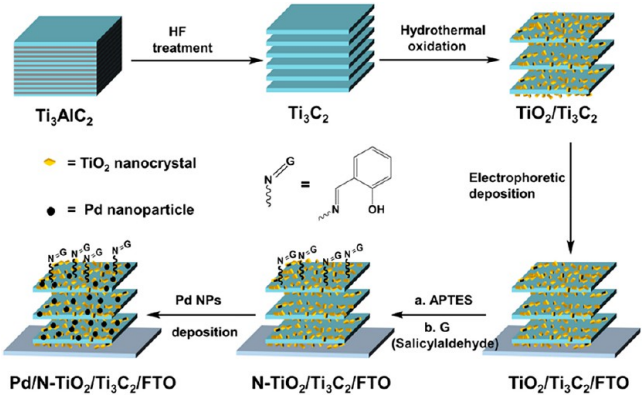

Figure 26. Schematic representation of $Pd/N-TiO_2/Ti_3C_2/FTO$ photocathode synthesis.[282] Reproduced with permission from ref 282. Copyright (2018), Elsevier.

The hydrothermal oxidation, electrophoretic deposition, amine functionalization, and pulse electrodeposition techniques were involved in the fabrication of electrodes. SEM and TEM images of Ti_3C_2 and TiO_2/Ti_3C_2 are shown in Figure 27. A typical laminate morphology was noticed for Ti_3C_2. The distance between the Ti_3C_2 layers was expanded by in situ-grown TiO_2 nanocrystals during the hydrothermal oxidation. The heterojunction formation was clearly perceived from the HRTEM images. An interface was spotted between the (101) plane of TiO_2 and (002) plane of Ti_3C_2. The layered morphology of Ti_3C_2 was not influenced by the hydrothermal oxidation and electrophoretic deposition. The surface area of TiO_2/Ti_3C_2 was 10-fold higher than that of Ti_3C_2, indicating that the heterojunction was beneficial for CO_2 adsorption.

PEC CO_2 conversion experiments were performed with a $CO_{2(g)}$-saturated 0.1 M $KHCO_3$ aqueous solution under 300 W Xe lamp irradiation. $Pd/N-TiO_2/Ti_3C_2/FTO$, bismuth vanadate, and Ad/AgCl were used as the photocathode, photoanode, and reference electrodes, respectively. A Si solar

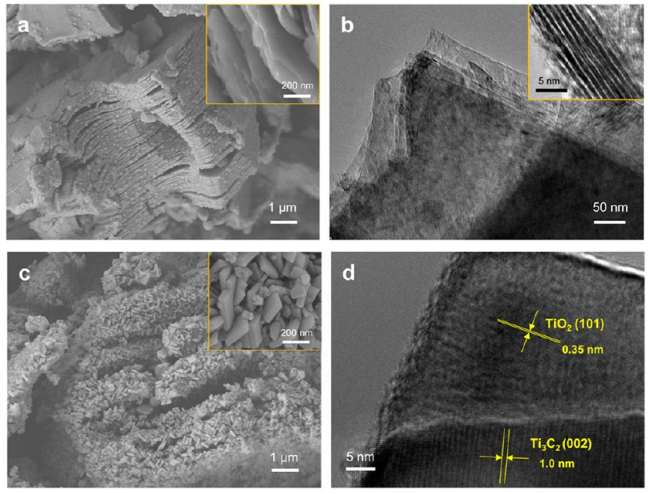

Figure 27. Ti_3C_2: (a) SEM, (b) TEM. TiO_2/Ti_3C_2 fabricated at 160 °C: (c) SEM, (d) HRTEM.[282] Reproduced with permission from ref 282. Copyright (2018), Elsevier.

cell was utilized to supply the external voltage to the EC cell. The photocurrent density of $Pd/N-TiO_2/Ti_3C_2/FTO$ fabricated at 160 °C was 2 times higher as compared to that of $Pd/Ti_3C_2/FTO$. The evolution of products such as total hydrocarbon, $HCOO^-$, CH_3OH (MeOH), and CH_3CH_2OH (EtOH) from PEC CO_2 conversion on various photocathodes at −0.8 V vs SCE is shown in Figure 28. The total hydrocarbon

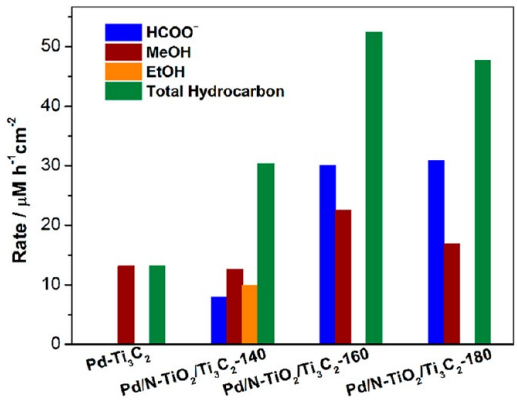

Figure 28. Evolution of products such as total hydrocarbon, $HCOO^-$, MeOH, and EtOH from PEC CO_2 conversion on various photocathodes at −0.8 V vs SCE.[282] Reproduced with permission from ref 282. Copyright (2018), Elsevier.

formation of $Pd/N-TiO_2/Ti_3C_2/FTO$ fabricated at 160 °C was ∼5 times higher than that of $Pd/Ti_3C_2/FTO$. The electrode was stable for 16 h without a drop in its efficiency. The high efficiency of $Pd/N-TiO_2/Ti_3C_2/FTO$ was attributed to its special morphology, high surface area, more active sites, strong visible light absorption, and Plasmon resonance effect of Pd.

In another study, a cobalt-doped N-site-rich ($Co-N_5$) polymer (hallow N-doped porous carbon spheres (Co-HNPCSs)) was designed for the electroreduction of CO_2.[283] The high surface area and electrical conductivity were the important features of the catalyst. The CO_2 adsorption and selectivity of CO formation were governed by the active center of single-atom Co−N5. The schematic of synthesis, SEM, TEM, elemental mapping, and high angle annular dark field

https://dx.doi.org/10.1021/acsenergylett.9b02585
ACS Energy Lett. 2020, 5, 486−519

scanning TEM (HAADF-STEM) images of Co−N_5/HNPCSs are shown in Figure 29. The core−shell was initially fabricated

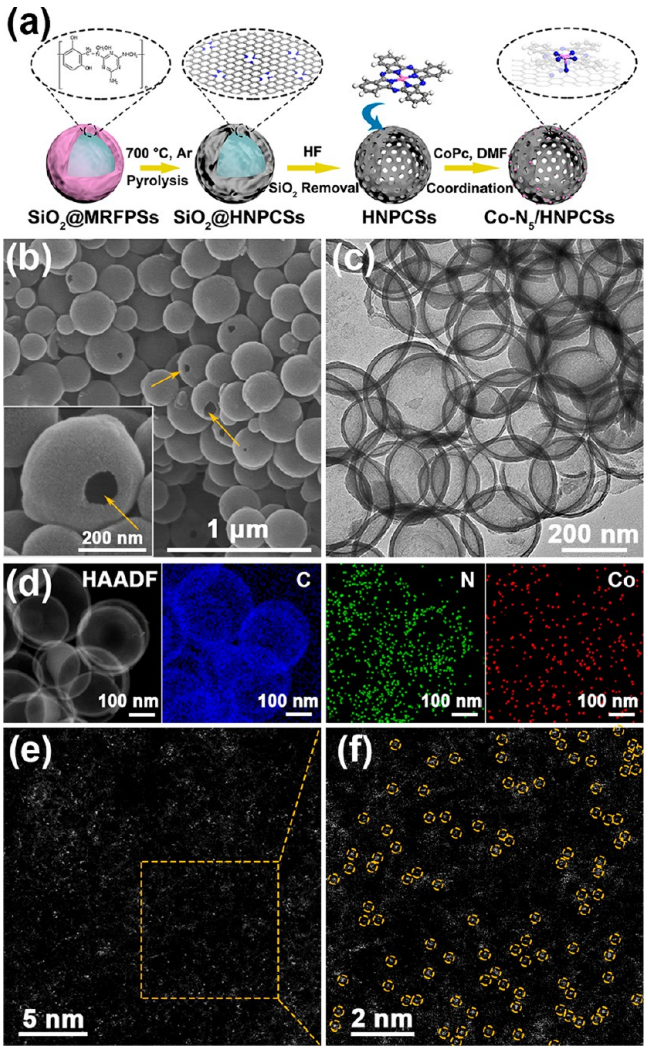

Figure 29. Co−N_5/HNPCSs: (a) schematic of the synthesis method, (b) SEM, (c) TEM, (d) HAADF-STEM with elemental mapping, and (e,f) aberration-corrected HAADF-STEM images.[283] Reproduced with permission from ref 283. Copyright (2018), American Chemical Society.

from the SiO_2 and melamine-resorcinol-formaldehyde polymer spheres (MRFPSs) by the Stober method.[284] It was further treated with Co phthalocyanine (CoPc) in dimethylformamide (DMF) solvent. SEM and TEM results showed that uniform spherical-shaped particles were successfully designed. The homogeneous distribution of elements was confirmed by elemental mapping. The existence of single Co atoms was seen as bright dots in the HAADF-STEM images.

DFT studies revealed that the N atom of the pyrrole ring could act as an anchor for Co with the polymer. The electroreduction experiments were performed in a $CO_{2(g)}$-saturated 0.2 M $NaHCO_3$ aqueous solution. The current density of Co−N_5/HNPCSs was around 15 times higher (6.2 mA/cm^2) than that of bare CoPc (0.4 mA/cm^2) at −0.73 V vs RHE. Moreover, the FE_{CO} of Co−N_5/HNPCSs was attained at 99.2% at −0.73 V vs RHE with a turnover frequency (TOF) of 480.2 h^{-1} and CO partial current density (4.5 mA/cm^2). The efficiency remained similar after 10 h of electrolyzing experiments. The reaction pathway of CO_2 reduction was investigated by DFT with the help of the H_2 electrode model (Figure 30a).[285] ΔG of CO_2 to COOH* for CoPc was very

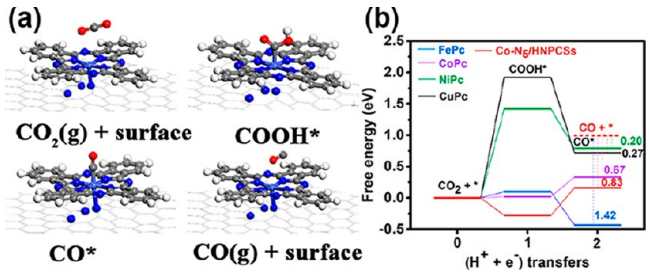

Figure 30. Reaction pathway of CO_2 reduction investigated by DFT with the help of the H_2 electrode model.[283] (a) Optimized structures of CO_2 and the intermediates and (b) calculated free energy of intermediates and products using various catalysts. Reproduced with permission from ref 283. Copyright (2018), American Chemical Society.

low compared to that of FePc, CuPc, and NiPc, suggesting the high efficiency of CoPc (Figure 30b). CO could easily desorb from CoPc when compared to another Pc's because of its low BE on CoPc (−0.68 eV). The high efficiency of Co−N_5/HNPCSs was ascribed to the strong bonding of the key intermediate (COOH*) and moderate bonding of the product (CO) on the Co center. A linear relationship was observed between the d band center of the catalyst and adsorption energy of the reactants.[286]

3D Materials: 3D materials with porous structures (e.g., foams, aerogels, sponges, etc.) have also gained much interest in recent years for the PEC/electrocatalytic CO_2 conversion.[287−294] 3D architectures with porous morphology could provide high specific surface area, maximum conductivity, stability, more surface active sites, and systematic mass transport reaction via the channels for electrode/electrolyte contact, promote light absorption, and improve the kinetics of CO_2 conversion.[292,295,296] Characteristics such as pore size, surface area, and porosity of 3D materials are key parameters to influence the CO_2 conversion efficiency.[297] The key findings of CO_2 conversion using 3D materials in recent years are highlighted in this section.

The electrocatalytic reduction of CO_2 to CO was examined by an unsaturated edge-anchored Ni single atom on N-doped microwave exfoliated porous GO (Ni−N-MEGO).[298] The infinite defects on the pore edge and enormous surface area of 3D MEGO are particularly favorable to anchor the Ni single atoms on its surface. Schematics of synthesis, TEM, STEM elemental mapping, aberration-corrected STEM, and atomic column intensity images of Ni−N-MEGO are shown in Figure 31. The surface area, pore volume, and average pore size of Ni−N-MEGO were evaluated to be 2380 m^2 g^{-1}, 1.68 m^3, and 2.6 nm, respectively. The surface features of Ni−N-MEGO were more comparable with that of pure MEGO. A 3D morphology with bamboo-like carbon nanotubes was observed from the TEM image of Ni−N-MEGO. Ni and N species were homogeneously dispersed on MEGO, which was identified from the aberration-corrected STEM images. The presence of Ni−N_x single-atom sites and local defects of the N atom were confirmed through atomic column intensity. The imperfect stacking structure of graphene layers was validated with the help of an aberration-corrected STEM images, which could

https://dx.doi.org/10.1021/acsenergylett.9b02585
ACS Energy Lett. 2020, 5, 486−519

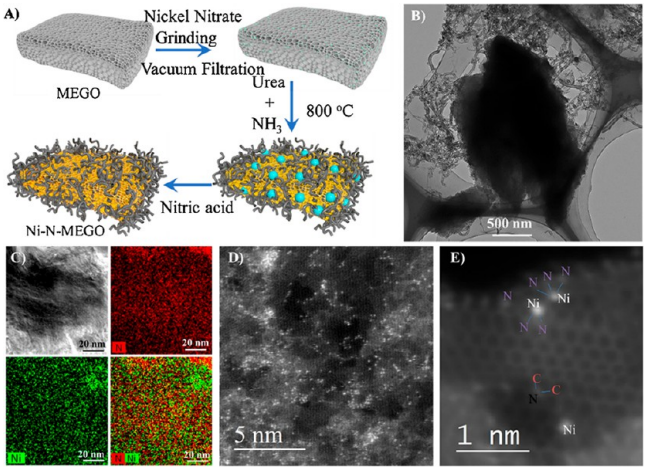

Figure 31. Ni−N-MEGO: (a) schematic representation of synthesis, (b) TEM, (c) STEM- elemental mapping, (d) aberration-corrected STEM, and (e) atomic column intensity to observe the presence of Ni−N_x single-atom sites and local defects of the N atom.[298] Reproduced with permission from ref 298. Copyright (2019), Elsevier.

create more grain boundaries to anchor the Ni single atoms. N-dopant was detected besides the Ni single atoms at the edges of the pore, indicating that the unsaturated Ni single atoms at the edge were anchored with N dopant. The cross section of Ni−N-MEGO was further analyzed through the focused ion beam SEM (FIB-SEM) technique. The results revealed that Ni and N atoms were uniformly dispersed over the highly patterned flake-like MEGO.

The bonding interactions in Ni−N-MEGO were interpreted via X-ray absorption spectroscopy (XAS). The results are displayed in Figure 32. The results showed that Ni atoms were

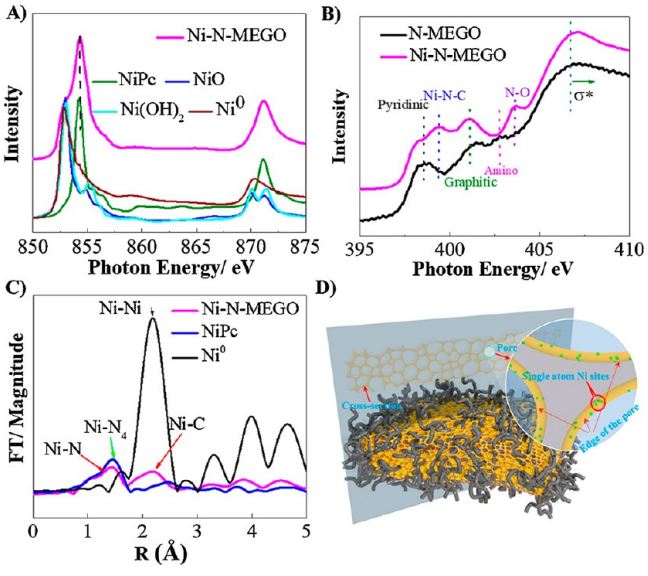

Figure 32. XAS: (A) Ni L-edge spectrum of Ni−N-MEGO, NiPc, NiO, $Ni(OH)_2$, and Ni^0, (B) extended X-ray absorption fine structure (EXAFS) of Ni−N-MEGO and N-MEGO, (C) Fourier transform EXAFS of Ni−N-MEGO, NiPc, and Ni^0, and (D) schematic for the dispersion of Ni single atoms at the edges of pore.[298] Reproduced with permission from ref 298. Copyright (2019), Elsevier.

mostly anchored with N dopant when compared to the possibilities or Ni−Ni, Ni−OH, or Ni−O bonds. The peak for Ni−N coordination was matched well with the Ni−N_4 peak of nickel phthalocyanine (NiPc). Although, the Ni−N peak intensity was lower than that of NiPc, suggesting the generation of unsaturated Ni−N_2 and Ni−N_3 in addition to the fine Ni−N_4 species. CO_2 electroreduction experiments were carried out using a $CO_{2(g)}$-saturated 0.5 $KHCO_3$ aqueous solution, Ni−N-MEGO as the working electrode, and iridium black as the counter electrode. The CO formation yield of Ni−N-MEGO was 4 times higher than that of N-MEGO at −0.55 V. The FE of Ni−N-MEGO was 92.1% at −0.55 V, and it was slightly lower at 89%, after 21 h of polarization.

The samples were also tested without acid treatment, but the FE was lower as compared to that of the acid-treated samples. The high performance of the catalyst is due to the presence of active sites such as Ni−N, N−C, Ni nanoparticles, and Ni−C coordination. Among them, Ni−N was the major active species responsible for high activity. DFT calculations also suggested that CO_2 electroreduction could mainly occur on the edge-anchored Ni−N coordination. The results showed that the CO_2 activation energy of in-plane Ni−N_4 was higher than that of edge Ni−N_4, indicating that the in-plane structures were less active for CO_2 reduction.[298]

In a similar study, a 3D core−shell porous Cu@Sn hybrid electrode (Cu at the core) was examined for the electrocatalytic conversion of CO_2 into formate.[299] The working electrode with 3D dendritic morphology was synthesized through a two-step electrodeposition technique. Sn was coated on the Cu substrate at various deposition times such as 0.5, 1, 2, 3, and 5 min. The dendritic corn-like morphology with macropores was identified by the SEM and TEM images. The schematic of synthesis, TEM, elemental mapping, and XRD of the 3D core−shell porous Cu@Sn hybrid electrode are shown in Figure 33.

The porosity and capacitance of electrodes were decreased with the increase of Sn deposition time. The thickness of the shell for $Cu@Sn_{(1)}$ (Cu@Sn with Sn deposition time of 1 min) was calculated to be ∼3 nm. The atomic radius of Sn is 0.162 nm, and therefore, nine layers of Sn could cover the Cu core. CO_2 conversion experiments were carried out using a $CO_{2(g)}$-saturated $KHCO_3$ solution. $Cu@Sn_{(1)}$ showed a current density of 55 mA/cm^2 at −1.33 V. The current density of Cu@Sn hybrid electrodes was reduced as the Sn deposition time was increased from 1 to 5 min. The highest current density of $Cu@Sn_{(1)}$ was ascribed to the high specific surface area with more active sites for CO_2 conversion. Besides, the $Cu@Sn_{(1)}$ electrode showed around 100% selectivity for the formate production (29.80 mmol/m^2/min) compared to other electrodes ($Cu@Sn_{(0.5)}$, $Cu@Sn_{(2)}$, $Cu@Sn_{(3)}$, and $Cu@Sn_{(5)}$) at −0.93 V vs RHE. This was ascribed to the special 3D morphology and porosity with the existence of metallic Sn on the surface of the $Cu@Sn_{(1)}$ electrode. A small amount of CH_4 and C_2H_4 was detected for $Cu@Sn_{(0.5)}$ and pure Cu electrodes. The selectivity of the $Cu@Sn_{(1)}$ electrode was superior compared to that for all other noble metals reported so far. The current density of the $Cu@Sn_{(1)}$ electrode was almost unchanged over 15 h of continuous electrolysis. The formate production rate was maintained well (26.89 mmol/m^2/min), with a small drop in FE from 100 to 96% during a 15 h experiment.

A macroporous 3D Co−Pi/$BiVO_4$/SnO_2 nanosheet array photoanode was investigated for PEC CO_2 conversion into

https://dx.doi.org/10.1021/acsenergylett.9b02585
ACS Energy Lett. 2020, 5, 486−519

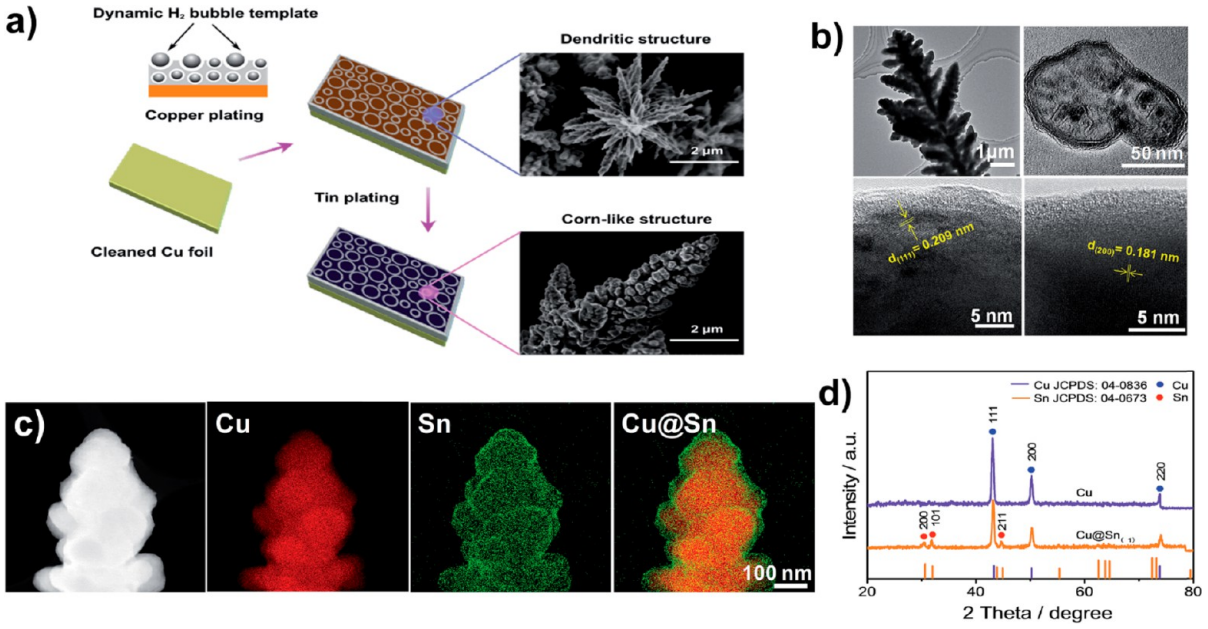

Figure 33. $Cu@Sn_{(1)}$ hybrid electrode: (a) schematic of synthesis, (b) TEM images, (c) elemental mapping, and (d) XRD pattern.[299] Reproduced with permission from ref 299. Copyright (2019), Royal Society of Chemistry.

CO.[129] $BiVO_4$ was anchored on a SnO_2 scaffold through the drop-casting method. Co−Pi co-catalyst was further deposited on $BiVO_4/SnO_2$ using the photoelectrodeposition technique. C−Au/CP (carbon-based Au nanoparticle on a carbon polymer plate) was utilized as the cathode. PEC experiments were performed with $CO_{2(g)}$-saturated 0.5 M $KHCO_3$ (catholyte) and $N_{2(g)}$-saturated 0.5 M potassium phosphate buffer (anolyte) solutions in an H-shaped cell. The design and working principle of the 3D Co−Pi/$BiVO_4/SnO_2$ photoanode are shown in Figure 34.

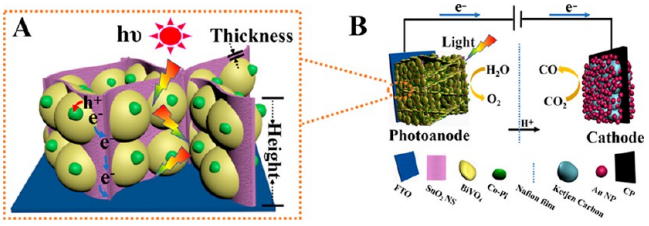

Figure 34. 3D Co−Pi/$BiVO_4/SnO_2$: (A) schematic of the photoanode design and (B) working principle of the photoanode for the PEC CO_2 conversion into CO.[129] Reproduced with permission from ref 129. Copyright (2019), American Chemical Society.

SEM, STEM-HAADF, and elemental mapping images of 3D Co−Pi/$BiVO_4/SnO_2$ are displayed in Figure 35. Thin SnO_2 nanosheet arrays with 10 ± 2.5 nm thickness and 1.2 μm height were vertically grown on the FTO glass plate. The macropores with 100−500 nm diameters were clearly observed from the top view of SEM images. The mesopores with 8−12 nm pore size were perceived from the TEM images. $BiVO_4$ was uniformly coated on SnO_2. The morphology of SnO_2 nanosheet arrays was not influenced by the deposition of $BiVO_4$ and Co−Pi. The photocurrent density of 3D Co−Pi/$BiVO_4/SnO_2$ was 20.2 times higher than that of pure $BiVO_4$. Likewise, the IPCE of 3D Co−Pi/$BiVO_4/SnO_2$ was 16.7 times higher as compared to that of pure $BiVO_4$, suggesting the

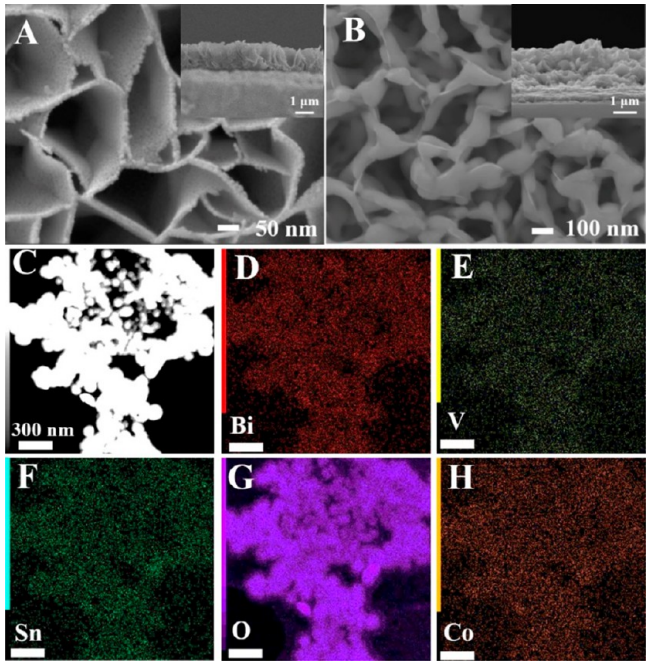

Figure 35. (A) SEM of SnO_2 nanosheet arrays, (B) SEM of $BiVO_4/SnO_2$ nanosheet arrays, (C) STEM-HAADF of Co−Pi/$BiVO_4/SnO_2$, and (D−H) elemental mapping images of Co−Pi/$BiVO_4/SnO_2$.[129] Reproduced with permission from ref 129. Copyright (2019), American Chemical Society.

strong light absorption capability of the 3D material. IPCE of the samples was in the following order: 3D Co−Pi/$BiVO_4/SnO_2$ > $BiVO_4/SnO_2$ > $BiVO_4$. The charge transfer resistance of 3D Co−Pi/$BiVO_4/SnO_2$ was much smaller as compared to that of pure $BiVO_4/SnO_2$ and 3D $BiVO_4$, indicating the formation of a heterojunction to endorse the charge carrier separation process.

3D Co−Pi/$BiVO_4/SnO_2$ showed a FE of 90% for CO formation at 1.1 V, and the material was stable for a 6000 s

https://dx.doi.org/10.1021/acsenergylett.9b02585
ACS Energy Lett. 2020, 5, 486−519

continuous PEC experiment. The electric energy-saving efficiency (η_s) of 3D Co−Pi/$BiVO_4$/SnO_2 was estimated from the applied voltages of the EC cell (V_{EC}) and PEC cell (V_{PEC}). The results showed that V_{PEC} of 3D Co−Pi/$BiVO_4$/SnO_2 was lower (1.1 V) as compared to V_{EC} (2.43 V) to produce the same current density. Therefore, the PEC cell using 3D Co−Pi/$BiVO_4$/SnO_2 could save more than 50% of electric energy as compared to the EC cell.

Challenges and Opportunities: Various efforts are required in the future to achieve the global goal to reduce the CO_2 emission. The commercial plants for CO_2 conversion into fuels and value-added products are located in a few countries including the U.S.A. (Liquid Light Incorporation, Exxon Mobil Corp., and Honeywell UOP), Iceland (George Olah), Germany (Bayer's Material Science Plant, and Audi AG), and Japan (Mitsubishi Heavy Industries).[113] Most of these industries convert CO_2 through the electrocatalysis technology. Various strategies should be taken to extend the commercialization of PEC CO_2 conversion at the industry level in developing countries to produce fuels from CO_2 and solve the energy requirements for the future. The following challenges need to be addressed for the large-scale production of value-added products from PEC CO_2 conversion. (i) *Stability*: Some electrode materials are inexpensive, but they are not stable under catalytic turnover cycles, and the scale up procedures are expensive. The efficiency of most electrode materials is affected by their photocorrosion behavior under prolonged usage in aqueous media. This could be surmounted by the use of Z-scheme heterojunction catalysts, room-temperature stable ionic liquids, and tandem PV−PEC cell designs. Cost-effective and simple synthesis methods are compulsory to fabricate the materials at a large scale with required surface features. (ii) *Light absorption*: Photoelectrodes with high visible light utilization are essential for their practical application under solar light irradiation. The strong light absorption capability of the photoelectrodes could reduce the necessity of high overpotential and improve the solar-to-chemical energy conversion. Utilization of plasmonic co-catalysts and suitable modifiers at the electrode surface could extend the light absorption capability. Expensive metals such as Au, Ru, Re, and Pt have been already replaced by Cu- and C-based materials in recent years. However, some additional studies are required to improve their product selectivity and efficiency. (iii) *Yield and selectivity*: The main issue from the thermodynamics and kinetics point of view is the bonding of CO_2 molecules at the electrode active sites and the bond-breaking/making reactions at the electrode−electrolyte interface. The structure−activity relationship between the photoelectrodes and co-catalysts should be studied thoroughly to maximize the performance. The product yield and selectivity could be improved through the utilization of molecular catalysts with adjustable active sites. Defect engineering and increasing of surface active sites could also enhance the efficiency of photoelectrodes.

Experimental evidence for the mechanism of PEC CO_2 conversion is still not clear. Many mechanistic studies should be performed at the molecular/atomic level to understand the reaction pathways in depth for high CO_2 conversion efficacy and product selectivity. DFT calculations and in situ time-resolved spectroscopy analysis should be employed to understand the reaction mechanism in detail. The application of in situ IR spectroscopy for the electrocatalytic CO_2 conversion was comprehensively reviewed in a recent study.[300] In situ IR spectroscopy is an outstanding tool to analyze the nature and binding interactions of various reaction intermediates (e.g., CO, COOH, etc.) at the electrode−electrolyte interface under operando conditions.[300] The efficiency, product selectivity, and stability of electrode materials could be optimized through the integration of electrochemistry with spectroscopic techniques.[300] The investigation of the adsorption of reaction intermediates at the catalyst surface would be highly valuable to certify the proposed mechanism of CO_2 conversion.[300] Especially, ATR-SEIRAS is more responsive toward the adsorbed intermediates as compared to the free species in the electrolyte solution. Oxygen vacancies and Ti^{3+} centers of TiO_2 could play a key role in its electrocatalytic CO_2 conversion activity. In situ UV−visible spectroscopy was combined with the EC cell to study the impact of CO_2 adsorption on the oxygen vacancies and Ti^{3+} centers of the TiO_2 electrode in a $CO_{2(g)}$-purged acetonitrile solution.[194] The results suggested that the adsorption of CO_2 on a TiO_2 surface could promote oxygen vacancy formation and stabilize the electron-rich Ti^{3+} centers.

Most of the characterization techniques including DFT explore the electrode materials only at the ground state. Studies are very limited to investigate the charge carrier dynamics and the light-induced excited-state reactions. Comprehensive investigations are essential to examine the formation of reaction intermediates, kinetics of CO_2 conversion, and active sites of the electrode. PEC CO_2 conversion reactions occur at the surface of the photoelectrode, and hence, the mass transfer of reactants and products should be upgraded. Ionic liquids are one of the promising electrolytes with high product selectivity, but they are very expensive. The guidelines should be framed to improve the stability of electrodes, cost-effective electrolytes, and ion-exchange membranes.

Techniques such as PEC, photocatalysis, thermocatalysis, and electrocatalysis could be used to convert the CO_2 into fuels and value-added products. Among them, electrocatalysis has been successfully commercialized. Technoeconomic analysis of a recent study suggested that the electrocatalytic CO_2 conversion is economically viable for various C1 and C2 products (CO, CH_3COH, CH_3CH_2OH, etc.).[301] The technical feasibility of electrocatalysis is owed to its high EE, compact design, continuous operation, and reasonable product yield. The source of electrons is the main ruling factor in PEC and electrocatalysis. Most of the existing PEC reactors are fundamental designs and applicable only at the laboratory scale. Hence, reactor designs should be upgraded for practical applications at the pilot scale. Techniques need to be developed to separate the products without affecting the yield. The cost of fabrication materials, complicated deigns, and the separation of products are the main factors for pilot-scale studies.[128] Economically, it is a challenging task for the researchers because the PEC device consumes more energy than it produces. The cost of electricity to power the electrolyzers in PEC is much higher as compared to the cost of methanol.[302] This could only be rectified through the use of renewable solar energy and improving the efficiency of photoelectrodes by several magnitudes. The efforts on the development of photoelectrodes for CO_2 conversion are not sufficient as compared to those for water splitting. The existing conversion efficiency of photoelectrode materials is low and unsuitable for the commercial scale. A minimum of 10% STF should be needed for commercialization.[303] PEC efficiency of

https://dx.doi.org/10.1021/acsenergylett.9b02585
ACS Energy Lett. 2020, 5, 486−519

materials has compared with electrocatalysis only in a few studies.[129] The recent reports suggested that biocathodes, Z-scheme heterojunctions, and tandem PV−PEC reactors are suitable options to carry out the CO_2 conversion without an external bias. However, these studies are still at the laboratory scale, and there are no detailed reports on the long-term stability. In the recent decade, more attention has been given to the development of photoelectrodes to achieve a high FE to produce CO, CH_3OH, and CH_4. Nevertheless, a good light-absorbing photoelectrode has not been established well yet. There are still reports on materials with low FE, but these materials are cheap and convenient to fabricate. Engineering innovations are very essential to design pilot-scale PEC reactors and produce stable CO_2 conversion efficiency at low capital costs. Standard experimental procedures and guidelines for PEC CO_2 conversion should be framed to attain the maximum efficiency like electrocatalysis. The design of an artificial leaf is one of the promising solutions to enrich the PEC efficiency. Worldwide research organizations should reinforce their interdisciplinary collaborations to design advanced materials to achieve higher solar energy conversion. There are several research groups working globally to gain benchmarking efficiency and commercialization of this technology with low energy input. The works are still under progress and in the preliminary stage.[304] Technologies should be developed to capture the concentrated CO_2 directly from the industries and convert it into liquid products. This could minimize the energy cost. A material with high thermal stability is required to directly convert the CO_2 before it is emitted into the atmosphere. The National Aeronautics and Space Administration (NASA) of the U.S.A. recently licensed a technology that could be used to convert CO_2 directly from industries into methane (Reference No. ARC-16461-1). A solar-powered TiO_2 thin film with the PEC setup has been utilized for this conversion. NASA is also interested in technologies for the conversion of CO_2 into sugars (such as glucose) from the Mars atmosphere.

Defect engineered 2D/3D materials, Z-scheme heterojunctions, bioelectrodes, and tandem photovoltaic−PEC reactors are suitable options to enhance the efficiency at low external bias.

Summary and Prospects. PEC CO_2 conversion is one of the most interesting technologies proposed to address climate change and the energy crisis using renewable solar energy. This Review article provides an overview of the state-of-the art of PEC CO_2 conversion technology and is intended for early stage researchers to inspire future research trends in this dynamic field. It also summarizes the great achievements in the past few years of CO_2 conversion into fuels and valuable chemical feedstocks. There are no comprehensive studies on the mechanism of PEC CO_2 conversion. An H-type PEC reactor with a suitable ion-exchange membrane has been utilized in most of the studies. Besides this, PEC reactor configurations such as continuous flow, microfluidic, and PV have gained much attention for their high performance in recent years. The efficiency of PEC CO_2 conversion can be expressed in terms of FE, STF, ABPE, IPCE, and APCE. The studies are very limited in relation to the kinetics of PEC CO_2 conversion. Models such as COSMOL multiphysics and microkinetics have been applied to investigate the kinetics of CO_2 conversion. The conversion of CO_2 into $CO_2^{\bullet-}$ intermediate is the main rate-determining step. The adsorption of intermediates on the electrode surface could be enhanced through the creation of hierarchical porous morphology. The electron migration process and the light absorption capability of nanomaterials could be improved by tuning their electronic properties. The CO_2 adsorption and conversion processes could be enhanced by the application of light irradiation with suitable wavelengths. The mechanism of CO_2 conversion could be investigated with the help of advanced analytical techniques such as secondary ion mass spectroscopy, low-energy ion scattering spectroscopy, X-ray computed tomography, in situ time-resolved spectroscopy, ambient-pressure XPS, environmental TEM, attenuated total reflection infrared spectroscopy, transient absorption spectroscopy, and variable-temperature scanning tunneling microscopy. The kinetic energy barriers of CO_2 conversion reaction could be investigated theoretically via DFT calculations and molecular dynamics. The excited-state reactions could be evaluated through time-dependent DFT studies. Most recent works emphasize the development of electrode materials. Carbon-based catalysts, MOFs, metal selenides, quantum dots, molecular catalysts, and biological enzymes have been investigated in recent studies. The requirement of high overpotentials for PEC CO_2 conversion could be minimized through the utilization of tandem PV−PEC reactors, Z-scheme photocatalysts, and biocathodes. The defect engineered 2D and 3D materials are the best candidates to scale-up this technology to the pilot or industry level. 2D and 3D materials will play an important role in the next few decades for renewable energy production (water splitting and CO_2 conversion), batteries, biomedical industries, and environment-related applications. PEC CO_2 conversion is one of the sustainable ways to control global warming. Further commercial developments are essential in this field to realize our dream of sustainable infrastructure and commence more industries producing nonpetroleum-derived fuels from CO_2.

■ ASSOCIATED CONTENT

Supporting Information

The Supporting Information is available free of charge at https://pubs.acs.org/doi/10.1021/acsenergylett.9b02585.

Efficiency and product selectivity of recent electrode materials for the PEC CO_2 conversion (PDF)

■ AUTHOR INFORMATION

Corresponding Authors

Vignesh Kumaravel − *Institute of Technology Sligo, Sligo, Ireland;* orcid.org/0000-0003-4755-189X;
Email: Kumaravel.Vignesh@itsligo.ie

Suresh C. Pillai − *Institute of Technology Sligo, Sligo, Ireland;* orcid.org/0000-0002-8901-9116;
Email: Pillai.Suresh@itsligo.ie

Other Author

John Bartlett − *Institute of Technology Sligo, Sligo, Ireland*

Complete contact information is available at: https://pubs.acs.org/10.1021/acsenergylett.9b02585

https://dx.doi.org/10.1021/acsenergylett.9b02585
ACS Energy Lett. 2020, 5, 486−519

Notes

The authors declare no competing financial interest.

Biographies

Dr. Vignesh Kumaravel is working at IT Sligo as a Senior Research Fellow in the Renewable Engine project. He obtained his Ph.D. from Madurai Kamaraj University, India in 2013. His research interests include the synthesis and utilization of various nanoparticles for clean energy, self-cleaning, food packaging polymers, and antimicrobial applications.

Dr. John Bartlett is Head of Research, founding Director of the Centre for Sustainability, and founder of the Contract Research Unit at IT, Sligo. His research includes ecotoxicology, environmental impact assessment, waste management technology, renewable energy technology, public access to environmental information, decision making and justice, and public services innovation.

Prof. Suresh C. Pillai is the head of the Nanotechnology and Bio-Engineering Research Group at the Institute of Technology, Sligo, Ireland. He obtained his Ph.D. from Trinity College Dublin and completed postdoctoral research at Caltech, U.S.A. His research interests include the synthesis of nanomaterials for energy and environmental applications.

■ ACKNOWLEDGMENTS

The authors are thankful to the Renewable Engine (RE) project funded by the European Union's INTERREG VA Programme, managed by the Special EU Programmes Body (SEUPB), with match funding provided by the Department for the Economy and Department of Jobs, Enterprise and Innovation in Ireland.

■ REFERENCES

(1) Reisinger, A.; Clark, H. How much do direct livestock emissions actually contribute to global warming? *Global change biology* **2018**, *24* (4), 1749−1761.
(2) Peter, S. C. Reduction of CO2 to Chemicals and Fuels: A Solution to Global Warming and Energy Crisis. *ACS Energy Letters* **2018**, *3* (7), 1557−1561.
(3) Wigley, T. The Paris warming targets: emissions requirements and sea level consequences. *Clim. Change* **2018**, *147* (1−2), 31−45.
(4) Goodwin, P.; Katavouta, A.; Roussenov, V. M.; Foster, G. L.; Rohling, E. J.; Williams, R. G. Pathways to 1.5 and 2 C warming based on observational and geological constraints. *Nat. Geosci.* **2018**, *11* (2), 102.
(5) Zachos, J. C.; Dickens, G. R.; Zeebe, R. E. An early Cenozoic perspective on greenhouse warming and carbon-cycle dynamics. *Nature* **2008**, *451* (7176), 279.
(6) Falkowski, P.; Scholes, R.; Boyle, E.; Canadell, J.; Canfield, D.; Elser, J.; Gruber, N.; Hibbard, K.; Högberg, P.; Linder, S. The global carbon cycle: a test of our knowledge of earth as a system. *Science* **2000**, *290* (5490), 291−296.
(7) Wu, H. L.; Li, X. B.; Tung, C. H.; Wu, L. Z. Semiconductor Quantum Dots: An Emerging Candidate for CO2 Photoreduction. *Adv. Mater.* **2019**, *31* (36), 1900709.
(8) Huang, C.-H.; Tan, C.-S. A review: CO2 utilization. *Aerosol Air Qual. Res.* **2014**, *14* (2), 480−499.
(9) Dong, F.; Wang, Y.; Su, B.; Hua, Y.; Zhang, Y. The process of peak CO2 emissions in developed economies: A perspective of industrialization and urbanization. *Resources, Conservation and Recycling* **2019**, *141*, 61−75.
(10) Mardani, A.; Streimikiene, D.; Cavallaro, F.; Loganathan, N.; Khoshnoudi, M. Carbon dioxide (CO2) emissions and economic growth: A systematic review of two decades of research from 1995 to 2017. *Sci. Total Environ.* **2019**, *649*, 31−49.
(11) Khalil, M.; Gunlazuardi, J.; Ivandini, T. A.; Umar, A. Photocatalytic conversion of CO2 using earth-abundant catalysts: A review on mechanism and catalytic performance. *Renewable Sustainable Energy Rev.* **2019**, *113*, 109246.
(12) Detz, R. J.; van der Zwaan, B. Transitioning towards negative CO2 emissions. *Energy Policy* **2019**, *133*, 110938.
(13) Wei, Y.; Li, Y.; Wu, M.; Li, Y. The decomposition of total-factor CO2 emission efficiency of 97 contracting countries in Paris Agreement. *Energy Economics* **2019**, *78*, 365−378.
(14) Kaya, Y.; Yamaguchi, M.; Geden, O. Towards net zero CO 2 emissions without relying on massive carbon dioxide removal. *Sustainability Science* **2019**, *14*, 1739−1743.
(15) Pelletier, C.; Rogaume, Y.; Dieckhoff, L.; Bardeau, G.; Pons, M.-N.; Dufour, A. Effect of combustion technology and biogenic CO2 impact factor on global warming potential of wood-to-heat chains. *Appl. Energy* **2019**, *235*, 1381−1388.
(16) Yu, K. M. K.; Curcic, I.; Gabriel, J.; Tsang, S. C. E. Recent advances in CO2 capture and utilization. *ChemSusChem* **2008**, *1* (11), 893−899.
(17) Li, L.; Zhao, N.; Wei, W.; Sun, Y. A review of research progress on CO2 capture, storage, and utilization in Chinese Academy of Sciences. *Fuel* **2013**, *108*, 112−130.
(18) Song, C.; Liu, Q.; Deng, S.; Li, H.; Kitamura, Y. Cryogenic-based CO2 capture technologies: State-of-the-art developments and current challenges. *Renewable Sustainable Energy Rev.* **2019**, *101*, 265−278.
(19) Pipes, R.; Bhargav, A.; Manthiram, A. Phenyl Disulfide Additive for Solution-Mediated Carbon Dioxide Utilization in Li−CO2 Batteries. *Adv. Energy Mater.* **2019**, *9* (21), 1900453.
(20) Arellano-Treviño, M. A.; Kanani, N.; Jeong-Potter, C. W.; Farrauto, R. J. Bimetallic catalysts for CO2 capture and hydrogenation at simulated flue gas conditions. *Chem. Eng. J.* **2019**, *375*, 121953.
(21) Kar, S.; Goeppert, A.; Prakash, G. S. Combined CO2 capture and hydrogenation to methanol: Amine immobilization enables easy recycling of active elements. *ChemSusChem* **2019**, *12* (13), 3172−3177.
(22) Jung, S.; Park, Y.-K.; Kwon, E. E. Strategic use of biochar for CO2 capture and sequestration. *Journal of CO2 Utilization* **2019**, *32*, 128−139.
(23) Pastero, L.; Curetti, N.; Ortenzi, M. A.; Schiavoni, M.; Destefanis, E.; Pavese, A. CO2 capture and sequestration in stable Ca-oxalate, via Ca-ascorbate promoted green reaction. *Sci. Total Environ.* **2019**, *666*, 1232−1244.
(24) Yang, H. J.; Yang, H.; Hong, Y. H.; Zhang, P. Y.; Wang, T.; Chen, L. N.; Zhang, F. Y.; Wu, Q. H.; Tian, N.; Zhou, Z. Y.; et al. Promoting ethylene selectivity from CO2 electroreduction on CuO supported onto CO2 capture materials. *ChemSusChem* **2018**, *11* (5), 881−887.
(25) He, B.; Sadiq, M. M.; Batten, M. P.; Suzuki, K.; Rubio-Martinez, M.; Gardiner, J.; Hill, M. Continuous Flow Synthesis of Zr Magnetic Framework Composite for Post-Combustion CO2 Capture. *Chem. - Eur. J.* **2019**, *25* (57), 13184−13188.
(26) Duan, Y. X.; Meng, F. L.; Liu, K. H.; Yi, S. S.; Li, S. J.; Yan, J. M.; Jiang, Q. Amorphizing of Cu nanoparticles toward highly efficient and robust electrocatalyst for CO2 reduction to liquid fuels with high faradaic efficiencies. *Adv. Mater.* **2018**, *30* (14), 1706194.
(27) Zain, M. M.; Mohamed, A. R. An overview on conversion technologies to produce value added products from CH4 and CO2 as major biogas constituents. *Renewable Sustainable Energy Rev.* **2018**, *98*, 56−63.
(28) Kar, S.; Goeppert, A.; Galvan, V.; Chowdhury, R.; Olah, J.; Prakash, G. S. A Carbon-Neutral CO2 Capture, Conversion, and Utilization Cycle with Low-Temperature Regeneration of Sodium Hydroxide. *J. Am. Chem. Soc.* **2018**, *140* (49), 16873−16876.
(29) Wu, X.; Li, Y.; Zhang, G.; Chen, H.; Li, J.; Wang, K.; Pan, Y.; Zhao, Y.; Sun, Y.; Xie, Y. Photocatalytic CO2 conversion of M0. 33WO3 directly from the air with high selectivity: Insight into full spectrum-induced reaction mechanism. *J. Am. Chem. Soc.* **2019**, *141* (13), 5267−5274.

https://dx.doi.org/10.1021/acsenergylett.9b02585
ACS Energy Lett. 2020, 5, 486−519

(30) Shi, Z.; Yang, H.; Gao, P.; Li, X.; Zhong, L.; Wang, H.; Liu, H.; Wei, W.; Sun, Y. Direct conversion of CO2 to long-chain hydrocarbon fuels over K−promoted CoCu/TiO2 catalysts. *Catal. Today* **2018**, *311*, 65−73.
(31) Moioli, E.; Mutschler, R.; Züttel, A. Renewable energy storage via CO2 and H2 conversion to methane and methanol: Assessment for small scale applications. *Renewable Sustainable Energy Rev.* **2019**, *107*, 497−506.
(32) Ma, W.; Wang, H.; Yu, W.; Wang, X.; Xu, Z.; Zong, X.; Li, C. Achieving Simultaneous CO2 and H2S Conversion via a Coupled Solar-Driven Electrochemical Approach on Non-Precious-Metal Catalysts. *Angew. Chem., Int. Ed.* **2018**, *57* (13), 3473−3477.
(33) Aljabour, A.; Coskun, H.; Apaydin, D. H.; Ozel, F.; Hassel, A. W.; Stadler, P.; Sariciftci, N. S.; Kus, M. Nanofibrous cobalt oxide for electrocatalysis of CO2 reduction to carbon monoxide and formate in an acetonitrile-water electrolyte solution. *Appl. Catal., B* **2018**, *229*, 163−170.
(34) Zheng, T.; Jiang, K.; Wang, H. Recent Advances in Electrochemical CO2-to-CO Conversion on Heterogeneous Catalysts. *Adv. Mater.* **2018**, *30* (48), 1802066.
(35) Krieg, T.; Sydow, A.; Faust, S.; Huth, I.; Holtmann, D. CO2 to Terpenes: Autotrophic and Electroautotrophic α-Humulene Production with Cupriavidus necator. *Angew. Chem., Int. Ed.* **2018**, *57* (7), 1879−1882.
(36) Kumar, A.; Semwal, S.; Choudhury, J. Catalytic Conversion of CO2 to Formate with Renewable Hydrogen Donors: An Ambient-Pressure and H2-Independent Strategy. *ACS Catal.* **2019**, *9* (3), 2164−2168.
(37) Trickett, C. A.; Helal, A.; Al-Maythalony, B. A.; Yamani, Z. H.; Cordova, K. E.; Yaghi, O. M. The chemistry of metal−organic frameworks for CO2 capture, regeneration and conversion. *Nature Reviews Materials* **2017**, *2* (8), 17045.
(38) Yang, D.; Yu, H.; He, T.; Zuo, S.; Liu, X.; Yang, H.; Ni, B.; Li, H.; Gu, L.; Wang, D.; et al. Visible-light-switched electron transfer over single porphyrin-metal atom center for highly selective electroreduction of carbon dioxide. *Nat. Commun.* **2019**, *10* (1), 1−10.
(39) Leung, J. J.; Warnan, J.; Ly, K. H.; Heidary, N.; Nam, D. H.; Kuehnel, M. F.; Reisner, E. Solar-driven reduction of aqueous CO 2 with a cobalt bis (terpyridine)-based photocathode. *Nature Catalysis* **2019**, *2* (4), 354.
(40) Kang, H.-Y.; Nam, D.-H.; Yang, K. D.; Joo, W.; Kwak, H.; Kim, H.-H.; Hong, S.-H.; Nam, K. T.; Joo, Y.-C. Synthetic Mechanism Discovery of Monophase Cuprous Oxide for Record High Photoelectrochemical Conversion of CO2 to Methanol in Water. *ACS Nano* **2018**, *12* (8), 8187−8196.
(41) Deng, X.; Li, R.; Wu, S.; Wang, L.; Hu, J.; Ma, J.; Jiang, W.; Zhang, N.; Zheng, X.; Gao, C.; et al. Metal-Organic Framework Coating Enhances the Performance of Cu2O in Photoelectrochemical CO2 Reduction. *J. Am. Chem. Soc.* **2019**, *141* (27), 10924−10929.
(42) Chen, J.; Yin, J.; Zheng, X.; Ait Ahsaine, H.; Zhou, Y.; Dong, C.; Mohammed, O. F.; Takanabe, K.; Bakr, O. M. Compositionally Screened Eutectic Catalytic Coatings on Halide Perovskite Photocathode for Photo-Assisted Selective CO2 Reduction. *ACS Energy Letters* **2019**, *4* (6), 1279−1286.
(43) Meng, A.; Zhang, L.; Cheng, B.; Yu, J. TiO2−MnO x−Pt Hybrid Multiheterojunction Film Photocatalyst with Enhanced Photocatalytic CO2-Reduction Activity. *ACS Appl. Mater. Interfaces* **2019**, *11* (6), 5581−5589.
(44) Kim, C.; Cho, K. M.; Al-Saggaf, A.; Gereige, I.; Jung, H.-T. Z-scheme photocatalytic CO2 conversion on three-dimensional BiVO4/carbon-coated Cu2O nanowire arrays under visible light. *ACS Catal.* **2018**, *8* (5), 4170−4177.
(45) Xia, T.; Long, R.; Gao, C.; Xiong, Y. Design of atomically dispersed catalytic sites for photocatalytic CO2 reduction. *Nanoscale* **2019**, *11*, 11064−11070.
(46) Cometto, C.; Kuriki, R.; Chen, L.; Maeda, K.; Lau, T.-C.; Ishitani, O.; Robert, M. A carbon nitride/Fe quaterpyridine catalytic system for photostimulated CO2-to-CO conversion with visible light. *J. Am. Chem. Soc.* **2018**, *140* (24), 7437−7440.
(47) Ran, J.; Jaroniec, M.; Qiao, S. Z. Cocatalysts in semiconductor-based photocatalytic CO2 reduction: achievements, challenges, and opportunities. *Adv. Mater.* **2018**, *30* (7), 1704649.
(48) Wang, S.; Xu, M.; Peng, T.; Zhang, C.; Li, T.; Hussain, I.; Wang, J.; Tan, B. Porous hypercrosslinked polymer-TiO2-graphene composite photocatalysts for visible-light-driven CO2 conversion. *Nat. Commun.* **2019**, *10* (1), 676.
(49) Huang, J.; Buonsanti, R. Colloidal nanocrystals as heterogeneous catalysts for electrochemical CO2 conversion. *Chem. Mater.* **2019**, *31* (1), 13−25.
(50) Guntern, Y. T.; Pankhurst, J. R.; Vávra, J.; Mensi, M.; Mantella, V.; Schouwink, P.; Buonsanti, R. Nanocrystal/Metal−Organic Framework Hybrids as Electrocatalytic Platforms for CO2 Conversion. *Angew. Chem., Int. Ed.* **2019**, *58* (36), 12632−12639.
(51) Ma, M.; Liu, K.; Shen, J.; Kas, R.; Smith, W. A. In Situ fabrication and reactivation of highly selective and stable Ag catalysts for electrochemical CO2 conversion. *ACS energy letters* **2018**, *3* (6), 1301−1306.
(52) Wang, J.; Ji, Y.; Shao, Q.; Yin, R.; Guo, J.; Li, Y.; Huang, X. Phase and structure modulating of bimetallic CuSn nanowires boosts electrocatalytic conversion of CO2. *Nano Energy* **2019**, *59*, 138−145.
(53) Nesbitt, N. T.; Ma, M.; Trześniewski, B. J.; Jaszewski, S.; Tafti, F.; Burns, M. J.; Smith, W. A.; Naughton, M. J. Au Dendrite Electrocatalysts for CO2 Electrolysis. *J. Phys. Chem. C* **2018**, *122* (18), 10006−10016.
(54) Diercks, C. S.; Liu, Y.; Cordova, K. E.; Yaghi, O. M. The role of reticular chemistry in the design of CO 2 reduction catalysts. *Nat. Mater.* **2018**, *17* (4), 301.
(55) Wang, Y.-R.; Huang, Q.; He, C.-T.; Chen, Y.; Liu, J.; Shen, F.-C.; Lan, Y.-Q. Oriented electron transmission in polyoxometalate-metalloporphyrin organic framework for highly selective electroreduction of CO 2. *Nat. Commun.* **2018**, *9* (1), 4466.
(56) Currie, R.; Mottaghi-Tabar, S.; Zhuang, Y.; Simakov, D. S. Design of an Air-Cooled Sabatier Reactor for Thermocatalytic Hydrogenation of CO2: Experimental Proof-of-Concept and Model-Based Feasibility Analysis. *Ind. Eng. Chem. Res.* **2019**, *58* (29), 12964−12980.
(57) Ferrah, D.; Haines, A. R.; Galhenage, R. P.; Bruce, J. P.; Babore, A. D.; Hunt, A.; Waluyo, I.; Hemminger, J. C. Wet Chemical Growth and Thermocatalytic Activity of Cu-Based Nanoparticles Supported on TiO2 Nanoparticles/HOPG: In Situ Ambient Pressure XPS Study of the CO2 Hydrogenation Reaction. *ACS Catal.* **2019**, *9* (8), 6783−6802.
(58) Takalkar, G.; Bhosale, R. R.; AlMomani, F.; Khraisheh, M. Thermocatalytic splitting of CO2 using sol-gel synthesized Co-ferrite redox materials. *Fuel* **2019**, *257*, 115965.
(59) Bai, Y.; Zhao, J.; Feng, S.; Liang, X.; Wang, C. Light-driven thermocatalytic CO 2 reduction over surface-passivated β-Mo 2 C nanowires: enhanced catalytic stability by light. *Chem. Commun.* **2019**, *55* (32), 4651−4654.
(60) Song, Y.; Zhang, X.; Xie, K.; Wang, G.; Bao, X. High-Temperature CO2 Electrolysis in Solid Oxide Electrolysis Cells: Developments, Challenges, and Prospects. *Adv. Mater.* **2019**, *31*, 1902033.
(61) Tackett, B. M.; Gomez, E.; Chen, J. G. Net reduction of CO 2 via its thermocatalytic and electrocatalytic transformation reactions in standard and hybrid processes. *Nature Catalysis* **2019**, *2*, 381−386.
(62) Lisovskaya, A.; Bartels, D. M. Reduction of CO2 by hydrated electrons in high temperature water. *Radiat. Phys. Chem.* **2019**, *158*, 61−63.
(63) Grills, D. C.; Farrington, J. A.; Layne, B. H.; Lymar, S. V.; Mello, B. A.; Preses, J. M.; Wishart, J. F. Mechanism of the formation of a Mn-based CO2 reduction catalyst revealed by pulse radiolysis with time-resolved infrared detection. *J. Am. Chem. Soc.* **2014**, *136* (15), 5563−5566.

(64) Grodkowski, J.; Neta, P. Copper-catalyzed radiolytic reduction of CO2 to CO in aqueous solutions. *J. Phys. Chem. B* **2001**, *105* (21), 4967−4972.
(65) Liu, X.; Kang, F.; Hu, C.; Wang, L.; Xu, Z.; Zheng, D.; Gong, W.; Lu, Y.; Ma, Y.; Wang, J. A genetically encoded photosensitizer protein facilitates the rational design of a miniature photocatalytic CO 2-reducing enzyme. *Nat. Chem.* **2018**, *10* (12), 1201.
(66) Cardias, B. B.; de Morais, M. G.; Costa, J. A. V. CO2 conversion by the integration of biological and chemical methods: Spirulina sp. LEB 18 cultivation with diethanolamine and potassium carbonate addition. *Bioresour. Technol.* **2018**, *267*, 77−83.
(67) Rittmann, S. K.-M.R.; Seifert, A. H.; Bernacchi, S. Kinetics, multivariate statistical modelling, and physiology of CO2-based biological methane production. *Appl. Energy* **2018**, *216*, 751−760.
(68) Yang, H.-Y.; Bao, B.-L.; Liu, J.; Qin, Y.; Wang, Y.-R.; Su, K.-Z.; Han, J.-C.; Mu, Y. Temperature dependence of bioelectrochemical CO2 conversion and methane production with a mixed-culture biocathode. *Bioelectrochemistry* **2018**, *119*, 180−188.
(69) Singh, R. K.; Singh, R.; Sivakumar, D.; Kondaveeti, S.; Kim, T.; Li, J.; Sung, B. H.; Cho, B.-K.; Kim, D. R.; Kim, S. C.; et al. Insights into Cell-Free conversion of CO2 to chemicals by a multienzyme cascade reaction. *ACS Catal.* **2018**, *8* (12), 11085−11093.
(70) Savvas, S.; Donnelly, J.; Patterson, T.; Chong, Z. S.; Esteves, S. R. Biological methanation of CO2 in a novel biofilm plug-flow reactor: A high rate and low parasitic energy process. *Appl. Energy* **2017**, *202*, 238−247.
(71) Efrati, A.; Lu, C.-H.; Michaeli, D.; Nechushtai, R.; Alsaoub, S.; Schuhmann, W.; Willner, I. Assembly of photo-bioelectrochemical cells using photosystem I-functionalized electrodes. *Nature Energy* **2016**, *1* (2), 15021.
(72) Wang, P.; Wang, S.; Wang, H.; Wu, Z.; Wang, L. Recent Progress on Photo-Electrocatalytic Reduction of Carbon Dioxide. *Particle & Particle Systems Characterization* **2018**, *35* (1), 1700371.
(73) Kang, M. J.; Kim, C. W.; Pawar, A. U.; Cha, H. G.; Ji, S.; Cai, W.-B.; Kang, Y. S. Selective Alcohol on Dark Cathode by Photoelectrochemical CO2 Valorization and Their in-situ Characterization. *ACS Energy Letters* **2019**, *4* (7), 1549−1555.
(74) DuChene, J. S.; Tagliabue, G.; Welch, A. J.; Cheng, W.-H.; Atwater, H. A. Hot hole collection and photoelectrochemical CO2 reduction with plasmonic Au/p-GaN photocathodes. *Nano Lett.* **2018**, *18* (4), 2545−2550.
(75) Ajmal, S.; Yang, Y.; Li, K.; Tahir, M. A.; Liu, Y.; Wang, T.; Bacha, A.-U.-R.; Feng, Y.; Deng, Y.; Zhang, L. Zinc Modified Copper Catalyst for Efficient (Photo-) Electrochemical CO2 Reduction with High Selectivity of HCOOH Production. *J. Phys. Chem. C* **2019**, *123* (18), 11555−11563.
(76) Sahara, G.; Kumagai, H.; Maeda, K.; Kaeffer, N.; Artero, V.; Higashi, M.; Abe, R.; Ishitani, O. Photoelectrochemical Reduction of CO2 Coupled to Water Oxidation Using a Photocathode with a Ru (II)−Re (I) Complex Photocatalyst and a CoO x/TaON Photoanode. *J. Am. Chem. Soc.* **2016**, *138* (42), 14152−14158.
(77) Song, J. T.; Ryoo, H.; Cho, M.; Kim, J.; Kim, J. G.; Chung, S. Y.; Oh, J. Nanoporous Au thin films on Si photoelectrodes for selective and efficient photoelectrochemical CO2 reduction. *Adv. Energy Mater.* **2017**, *7* (3), 1601103.
(78) Kuk, S. K.; Singh, R. K.; Nam, D. H.; Singh, R.; Lee, J. K.; Park, C. B. Photoelectrochemical reduction of carbon dioxide to methanol through a highly efficient enzyme cascade. *Angew. Chem., Int. Ed.* **2017**, *56* (14), 3827−3832.
(79) Chu, S.; Fan, S.; Wang, Y.; Rossouw, D.; Wang, Y.; Botton, G. A.; Mi, Z. Tunable syngas production from CO2 and H2O in an aqueous photoelectrochemical cell. *Angew. Chem., Int. Ed.* **2016**, *55* (46), 14262−14266.
(80) Kang, U.; Yoon, S. H.; Han, D. S.; Park, H. Synthesis of Aliphatic Acids from CO2 and Water at Efficiencies Close to the Photosynthesis Limit Using Mixed Copper and Iron Oxide Films. *ACS Energy Letters* **2019**, *4*, 2075−2080.
(81) Liu, C.; Colón, B. C.; Ziesack, M.; Silver, P. A.; Nocera, D. G. Water splitting−biosynthetic system with CO2 reduction efficiencies exceeding photosynthesis. *Science* **2016**, *352* (6290), 1210−1213.
(82) Yadav, R. K.; Baeg, J.-O.; Oh, G. H.; Park, N.-J.; Kong, K.-j.; Kim, J.; Hwang, D. W.; Biswas, S. K. A photocatalyst−enzyme coupled artificial photosynthesis system for solar energy in production of formic acid from CO2. *J. Am. Chem. Soc.* **2012**, *134* (28), 11455−11461.
(83) Kim, D.; Sakimoto, K. K.; Hong, D.; Yang, P. Artificial photosynthesis for sustainable fuel and chemical production. *Angew. Chem., Int. Ed.* **2015**, *54* (11), 3259−3266.
(84) Yang, C.-C.; Yu, Y.-H.; van der Linden, B.; Wu, J. C.; Mul, G. Artificial photosynthesis over crystalline TiO2-based catalysts: fact or fiction? *J. Am. Chem. Soc.* **2010**, *132* (24), 8398−8406.
(85) Ji, Y.; Luo, Y. Direct Donation of Protons from H2O to CO2 in Artificial Photosynthesis on the Anatase TiO2 (101) Surface. *J. Phys. Chem. C* **2019**, *123* (5), 3019−3023.
(86) Jang, Y. J.; Jeong, I.; Lee, J.; Lee, J.; Ko, M. J.; Lee, J. S. Unbiased sunlight-driven artificial photosynthesis of carbon monoxide from CO2 using a ZnTe-based photocathode and a perovskite solar cell in tandem. *ACS Nano* **2016**, *10* (7), 6980−6987.
(87) Sun, Z.; Ma, T.; Tao, H.; Fan, Q.; Han, B. Fundamentals and challenges of electrochemical CO2 reduction using two-dimensional materials. *Chem.* **2017**, *3* (4), 560−587.
(88) Wang, Y.; Liu, J.; Wang, Y.; Wang, Y.; Zheng, G. Efficient solar-driven electrocatalytic CO2 reduction in a redox-medium-assisted system. *Nat. Commun.* **2018**, *9* (1), 5003.
(89) Shan, B.; Vanka, S.; Li, T.-T.; Troian-Gautier, L.; Brennaman, M. K.; Mi, Z.; Meyer, T. J. Binary molecular-semiconductor p−n junctions for photoelectrocatalytic CO 2 reduction. *Nature Energy* **2019**, *4* (4), 290.
(90) Xu, S.; Carter, E. A. Theoretical insights into heterogeneous (Photo) electrochemical CO2 reduction. *Chem. Rev.* **2019**, *119* (11), 6631−6669.
(91) Zhou, X.; Liu, R.; Sun, K.; Chen, Y.; Verlage, E.; Francis, S. A.; Lewis, N. S.; Xiang, C. Solar-driven reduction of 1 atm of CO2 to formate at 10% energy-conversion efficiency by use of a TiO2-protected III−V tandem photoanode in conjunction with a bipolar membrane and a Pd/C cathode. *ACS Energy Letters* **2016**, *1* (4), 764−770.
(92) Zhang, N.; Long, R.; Gao, C.; Xiong, Y. Recent progress on advanced design for photoelectrochemical reduction of CO 2 to fuels. *Science China Materials* **2018**, *61* (6), 771−805.
(93) Ganesh, I. Conversion of carbon dioxide to methanol using solar energy-a brief review. *Mater. Sci. Appl.* **2011**, *02* (10), 1407.
(94) Wang, L.; Chen, W.; Zhang, D.; Du, Y.; Amal, R.; Qiao, S.; Wu, J.; Yin, Z. Surface strategies for catalytic CO 2 reduction: from two-dimensional materials to nanoclusters to single atoms. *Chem. Soc. Rev.* **2019**, *48* (21), 5310−5349.
(95) Xie, S.; Zhang, Q.; Liu, G.; Wang, Y. Photocatalytic and photoelectrocatalytic reduction of CO 2 using heterogeneous catalysts with controlled nanostructures. *Chem. Commun.* **2016**, *52* (1), 35−59.
(96) Taheri Najafabadi, A. CO2 chemical conversion to useful products: an engineering insight to the latest advances toward sustainability. *Int. J. Energy Res.* **2013**, *37* (6), 485−499.
(97) Pawar, A. U.; Kim, C. W.; Nguyen-Le, M.-T.; Kang, Y. S. General Review on the Components and Parameters of Photoelectrochemical System for CO2 Reduction with in Situ Analysis. *ACS Sustainable Chem. Eng.* **2019**, *7* (8), 7431−7455.
(98) Centi, G.; Perathoner, S. CO2-based energy vectors for the storage of solar energy. *Greenhouse Gases: Sci. Technol.* **2011**, *1* (1), 21−35.
(99) Lim, R. J.; Xie, M.; Sk, M. A.; Lee, J.-M.; Fisher, A.; Wang, X.; Lim, K. H. A review on the electrochemical reduction of CO2 in fuel cells, metal electrodes and molecular catalysts. *Catal. Today* **2014**, *233*, 169−180.
(100) Zhang, B.; Sun, L. Artificial photosynthesis: opportunities and challenges of molecular catalysts. *Chem. Soc. Rev.* **2019**, *48* (7), 2216−2264.

(101) Grills, D. C.; Ertem, M. Z.; McKinnon, M.; Ngo, K. T.; Rochford, J. Mechanistic aspects of CO2 reduction catalysis with manganese-based molecular catalysts. *Coord. Chem. Rev.* **2018**, *374*, 173−217.
(102) Kumar, B.; Llorente, M.; Froehlich, J.; Dang, T.; Sathrum, A.; Kubiak, C. P. Photochemical and photoelectrochemical reduction of CO2. *Annu. Rev. Phys. Chem.* **2012**, *63*, 541−569.
(103) Prasad, C.; Tang, H.; Liu, Q. Q.; Zulfiqar, S.; Shah, S.; Bahadur, I. An overview of semiconductors/layered double hydroxides composites: Properties, synthesis, photocatalytic and photoelectrochemical applications. *J. Mol. Liq.* **2019**, *289*, 111114.
(104) House, R. L.; Iha, N. Y. M.; Coppo, R. L.; Alibabaei, L.; Sherman, B. D.; Kang, P.; Brennaman, M. K.; Hoertz, P. G.; Meyer, T. J. Artificial Photosynthesis: Where are we now? Where can we Go? *J. Photochem. Photobiol., C* **2015**, *25*, 32−45.
(105) Vennekoetter, J.-B.; Sengpiel, R.; Wessling, M. Beyond the catalyst: How electrode and reactor design determine the product spectrum during electrochemical CO2 reduction. *Chem. Eng. J.* **2019**, *364*, 89−101.
(106) Lui, Y. H.; Zhang, B.; Hu, S. Rational design of photoelectrodes for photoelectrochemical water splitting and CO2 reduction. *Frontiers of Physics* **2019**, *14* (5), 53402.
(107) Pang, H.; Masuda, T.; Ye, J. Semiconductor-Based Photoelectrochemical Conversion of Carbon Dioxide: Stepping Towards Artificial Photosynthesis. *Chem. - Asian J.* **2018**, *13* (2), 127−142.
(108) Vennekötter, J.-B.; Scheuermann, T.; Sengpiel, R.; Wessling, M. The electrolyte matters: Stable systems for high rate electrochemical CO2 reduction. *Journal of CO2 Utilization* **2019**, *32*, 202−213.
(109) Chang, X.; Wang, T.; Gong, J. CO 2 photo-reduction: insights into CO 2 activation and reaction on surfaces of photocatalysts. *Energy Environ. Sci.* **2016**, *9* (7), 2177−2196.
(110) Tountas, A. A.; Peng, X.; Tavasoli, A. V.; Duchesne, P. N.; Dingle, T. L.; Dong, Y.; Hurtado, L.; Mohan, A.; Sun, W.; Ulmer, U.; et al. Towards Solar Methanol: Past, Present, and Future. *Adv. Sci.* **2019**, *6* (8), 1801903.
(111) Yang, Y.; Ajmal, S.; Zheng, X.; Zhang, L. Efficient nanomaterials for harvesting clean fuels from electrochemical and photoelectrochemical CO 2 reduction. *Sustainable Energy & Fuels* **2018**, *2* (3), 510−537.
(112) Bonomo, M.; Dini, D.; Decker, F. Electrochemical and photoelectrochemical properties of nickel oxide (NiO) with nanostructured morphology for photoconversion applications. *Front. Chem.* **2018**, *6*, 601.
(113) Ganesh, I. Electrochemical conversion of carbon dioxide into renewable fuel chemicals−The role of nanomaterials and the commercialization. *Renewable Sustainable Energy Rev.* **2016**, *59*, 1269−1297.
(114) Zheng, Y.; Zhang, W.; Li, Y.; Chen, J.; Yu, B.; Wang, J.; Zhang, L.; Zhang, J. Energy related CO2 conversion and utilization: advanced materials/nanomaterials, reaction mechanisms and technologies. *Nano Energy* **2017**, *40*, 512−539.
(115) Daiyan, R.; Lu, X.; Ng, Y. H.; Amal, R. Liquid Hydrocarbon Production from CO2: Recent Development in Metal-Based Electrocatalysis. *ChemSusChem* **2017**, *10* (22), 4342−4358.
(116) Maeda, K. Metal-Complex/Semiconductor Hybrid Photocatalysts and Photoelectrodes for CO2 Reduction Driven by Visible Light. *Adv. Mater.* **2019**, *31* (25), 1808205.
(117) Dey, A.; Maiti, D.; Lahiri, G. K. Photoelectrocatalytic Reduction of CO2 into C1 Products by Using Modified-Semiconductor-Based Catalyst Systems. *Asian J. Org. Chem.* **2017**, *6* (11), 1519−1530.
(118) Oh, Y.; Hu, X. Organic molecules as mediators and catalysts for photocatalytic and electrocatalytic CO 2 reduction. *Chem. Soc. Rev.* **2013**, *42* (6), 2253−2261.
(119) Remiro-Buenamañana, S.; García, H. Photoassisted CO2 conversion to fuels. *ChemCatChem* **2019**, *11* (1), 342−356.
(120) Wu, N. Plasmonic metal−semiconductor photocatalysts and photoelectrochemical cells: a review. *Nanoscale* **2018**, *10* (6), 2679−2696.
(121) Zhao, Y.; Waterhouse, G. I.; Chen, G.; Xiong, X.; Wu, L.-Z.; Tung, C.-H.; Zhang, T. Two-dimensional-related catalytic materials for solar-driven conversion of CO x into valuable chemical feedstocks. *Chem. Soc. Rev.* **2019**, *48* (7), 1972−2010.
(122) Zhu, X.; Li, Y. Review of two-dimensional materials for electrochemical CO2 reduction from a theoretical perspective. *Wiley Interdiscip. Rev.: Comput. Mol. Sci.* **2019**, *9* (6), No. e1416.
(123) Zhang, D.; Shi, J.; Zi, W.; Wang, P.; Liu, S. Recent Advances in Photoelectrochemical Applications of Silicon Materials for Solar-to-Chemicals Conversion. *ChemSusChem* **2017**, *10* (22), 4324−4341.
(124) Zhou, H.; Guo, J.; Li, P.; Fan, T.; Zhang, D.; Ye, J. Leaf-architectured 3D hierarchical artificial photosynthetic system of perovskite titanates towards CO2 photoreduction into hydrocarbon fuels. *Sci. Rep.* **2013**, *3*, 1667.
(125) Tu, W.; Zhou, Y.; Zou, Z. Photocatalytic conversion of CO2 into renewable hydrocarbon fuels: state-of-the-art accomplishment, challenges, and prospects. *Adv. Mater.* **2014**, *26* (27), 4607−4626.
(126) Chang, X.; Wang, T.; Yang, P.; Zhang, G.; Gong, J. The Development of Cocatalysts for Photoelectrochemical CO2 Reduction. *Adv. Mater.* **2019**, *31*, 1804710.
(127) Kim, C. W.; Kang, M. J.; Ji, S.; Kang, Y. S. Artificial photosynthesis for formaldehyde production with 85% of faradaic efficiency by tuning the reduction potential. *ACS Catal.* **2018**, *8* (2), 968−974.
(128) Kalamaras, E.; Maroto-Valer, M. M.; Shao, M.; Xuan, J.; Wang, H. Solar carbon fuel via photoelectrochemistry. *Catal. Today* **2018**, *317*, 56−75.
(129) Liu, L.-X.; Fu, J.; Jiang, L.-P.; Zhang, J.-r.; Zhu, W.; Lin, Y. Highly Efficient Photoelectrochemical Reduction of CO2 at Low Applied Voltage Using 3D Co-Pi/BiVO4/SnO2 Nanosheet Array Photoanode. *ACS Appl. Mater. Interfaces* **2019**, *11* (29), 26024−26031.
(130) Kalamaras, E.; Maroto-Valer, M. M.; Andresen, J. M.; Wang, H.; Xuan, J. Thermodynamic Analysis of the Efficiency of Photoelectrochemical CO2 Reduction to Ethanol. *Energy Procedia* **2019**, *158*, 767−772.
(131) Lee, W.-H.; Liao, C.-H.; Tsai, M.-F.; Huang, C.-W.; Wu, J. C. A novel twin reactor for CO2 photoreduction to mimic artificial photosynthesis. *Appl. Catal., B* **2013**, *132*, 445−451.
(132) Varghese, O. K.; Grimes, C. A. Appropriate strategies for determining the photoconversion efficiency of water photoelectrolysis cells: a review with examples using titania nanotube array photoanodes. *Sol. Energy Mater. Sol. Cells* **2008**, *92* (4), 374−384.
(133) Nguyen, V.-H.; Wu, J. C. Recent developments in the design of photoreactors for solar energy conversion from water splitting and CO2 reduction. *Appl. Catal., A* **2018**, *550*, 122−141.
(134) Bevilacqua, M.; Filippi, J.; Miller, H. A.; Vizza, F. Recent technological progress in CO2 electroreduction to fuels and energy carriers in aqueous environments. *Energy Technol.* **2015**, *3* (3), 197−210.
(135) Zhao, J.; Wang, X.; Xu, Z.; Loo, J. S. Hybrid catalysts for photoelectrochemical reduction of carbon dioxide: a prospective review on semiconductor/metal complex co-catalyst systems. *J. Mater. Chem. A* **2014**, *2* (37), 15228−15233.
(136) Peng, Y.-P.; Yeh, Y.-T.; Shah, S. I.; Huang, C. Concurrent photoelectrochemical reduction of CO2 and oxidation of methyl orange using nitrogen-doped TiO2. *Appl. Catal., B* **2012**, *123*, 414−423.
(137) Yin, G.; Abe, H.; Kodiyath, R.; Ueda, S.; Srinivasan, N.; Yamaguchi, A.; Miyauchi, M. Selective electro-or photo-reduction of carbon dioxide to formic acid using a Cu−Zn alloy catalyst. *J. Mater. Chem. A* **2017**, *5* (24), 12113−12119.
(138) Alenezi, K.; Ibrahim, S. K.; Li, P.; Pickett, C. J. Solar Fuels: Photoelectrosynthesis of CO from CO2 at p-Type Si using Fe Porphyrin Electrocatalysts. *Chem. - Eur. J.* **2013**, *19* (40), 13522−13527.

(139) Sekimoto, T.; Hashiba, H.; Shinagawa, S.; Uetake, Y.; Deguchi, M.; Yotsuhashi, S.; Ohkawa, K. Analysis of Products from Photoelectrochemical Reduction of 13CO2 by GaN-Si Based Tandem Photoelectrode. *J. Phys. Chem. C* **2016**, *120* (26), 13970−13975.
(140) Castro, S.; Albo, J.; Irabien, A. Photoelectrochemical reactors for CO2 utilization. *ACS Sustainable Chem. Eng.* **2018**, *6* (12), 15877−15894.
(141) Ola, O.; Maroto-Valer, M. M. Review of material design and reactor engineering on TiO2 photocatalysis for CO2 reduction. *J. Photochem. Photobiol., C* **2015**, *24*, 16−42.
(142) Wang, Q.; Tao, L.; Jiang, X.; Wang, M.; Shen, Y. Graphene oxide wrapped CH3NH3PbBr3 perovskite quantum dots hybrid for photoelectrochemical CO2 reduction in organic solvents. *Appl. Surf. Sci.* **2019**, *465*, 607−613.
(143) Wang, J.; Wei, Y.; Yang, B.; Wang, B.; Chen, J.; Jing, H. In situ grown heterojunction of Bi2WO6/BiOCl for efficient photoelectrocatalytic CO2 reduction. *J. Catal.* **2019**, *377*, 209−217.
(144) Wang, Y.; Wang, H.; Woldu, A. R.; Zhang, X.; He, T. Optimization of charge behavior in nanoporous CuBi2O4 photocathode for photoelectrochemical reduction of CO2. *Catal. Today* **2019**, *335*, 388−394.
(145) Li, K.; Han, J.; Yang, Y.; Wang, T.; Feng, Y.; Ajmal, S.; Liu, Y.; Deng, Y.; Tahir, M. A.; Zhang, L. Simultaneous SO2 removal and CO2 reduction in a nano-BiVO4| Cu-In nanoalloy photoelectrochemical cell. *Chem. Eng. J.* **2019**, *355*, 11−21.
(146) Jiang, Z.; Sun, H.; Wang, T.; Wang, B.; Wei, W.; Li, H.; Yuan, S.; An, T.; Zhao, H.; Yu, J.; et al. Nature-based catalyst for visible-light-driven photocatalytic CO2 reduction. *Energy Environ. Sci.* **2018**, *11* (9), 2382−2389.
(147) Wei, L.; Lin, J.; Xie, S.; Ma, W.; Zhang, Q.; Shen, Z.; Wang, Y. Photoelectrocatalytic reduction of CO2 to syngas over Ag nanoparticle modified p-Si nanowire arrays. *Nanoscale* **2019**, *11*, 12530−12536.
(148) Chu, S.; Ou, P.; Ghamari, P.; Vanka, S.; Zhou, B.; Shih, I.; Song, J.; Mi, Z. Photoelectrochemical CO2 reduction into syngas with the metal/oxide interface. *J. Am. Chem. Soc.* **2018**, *140* (25), 7869−7877.
(149) Kim, Y.; Creel, E. B.; Corson, E. R.; McCloskey, B. D.; Urban, J. J.; Kostecki, R. Surface-Plasmon-Assisted Photoelectrochemical Reduction of CO2 and NO3− on Nanostructured Silver Electrodes. *Adv. Energy Mater.* **2018**, *8* (22), 1800363.
(150) Iqbal, M.; Wang, Y.; Hu, H.; He, M.; Shah, A. H.; Lin, L.; Li, P.; Shao, K.; Woldu, A. R.; He, T. Cu2O-tipped ZnO nanorods with enhanced photoelectrochemical performance for CO2 photoreduction. *Appl. Surf. Sci.* **2018**, *443*, 209−216.
(151) Ong, W.-J.; Putri, L. K.; Tan, Y.-C.; Tan, L.-L.; Li, N.; Ng, Y. H.; Wen, X.; Chai, S.-P. Unravelling charge carrier dynamics in protonated gC 3 N 4 interfaced with carbon nanodots as co-catalysts toward enhanced photocatalytic CO 2 reduction: a combined experimental and first-principles DFT study. *Nano Res.* **2017**, *10* (5), 1673−1696.
(152) Merino-Garcia, I.; Alvarez-Guerra, E.; Albo, J.; Irabien, A. Electrochemical membrane reactors for the utilisation of carbon dioxide. *Chem. Eng. J.* **2016**, *305*, 104−120.
(153) Schreier, M.; Héroguel, F.; Steier, L.; Ahmad, S.; Luterbacher, J. S.; Mayer, M. T.; Luo, J.; Grätzel, M. Solar conversion of CO2 to CO using Earth-abundant electrocatalysts prepared by atomic layer modification of CuO. *Nature Energy* **2017**, *2* (7), 17087.
(154) Ramdin, M.; Morrison, A. R.; de Groen, M.; van Haperen, R.; De Kler, R.; van den Broeke, L. J.; Trusler, J. M.; de Jong, W.; Vlugt, T. J. High Pressure Electrochemical Reduction of CO2 to Formic Acid/Formate: A Comparison between Bipolar Membranes and Cation Exchange Membranes. *Ind. Eng. Chem. Res.* **2019**, *58* (5), 1834−1847.
(155) Li, Y. C.; Zhou, D.; Yan, Z.; Gonçalves, R. H.; Salvatore, D. A.; Berlinguette, C. P.; Mallouk, T. E. Electrolysis of CO2 to syngas in bipolar membrane-based electrochemical cells. *ACS Energy Letters* **2016**, *1* (6), 1149−1153.
(156) Vermaas, D. A.; Smith, W. A. Synergistic electrochemical CO2 reduction and water oxidation with a bipolar membrane. *ACS Energy Letters* **2016**, *1* (6), 1143−1148.
(157) Salvatore, D. A.; Weekes, D. M.; He, J.; Dettelbach, K. E.; Li, Y. C.; Mallouk, T. E.; Berlinguette, C. P. Electrolysis of Gaseous CO2 to CO in a Flow Cell with a Bipolar Membrane. *ACS Energy Letters* **2018**, *3* (1), 149−154.
(158) Singh, M. R.; Clark, E. L.; Bell, A. T. Effects of electrolyte, catalyst, and membrane composition and operating conditions on the performance of solar-driven electrochemical reduction of carbon dioxide. *Phys. Chem. Chem. Phys.* **2015**, *17* (29), 18924−18936.
(159) Kondratenko, E. V.; Mul, G.; Baltrusaitis, J.; Larrazábal, G. O.; Pérez-Ramírez, J. Status and perspectives of CO 2 conversion into fuels and chemicals by catalytic, photocatalytic and electrocatalytic processes. *Energy Environ. Sci.* **2013**, *6* (11), 3112−3135.
(160) Wang, R.; Haspel, H.; Pustovarenko, A.; Dikhtiarenko, A.; Russkikh, A.; Shterk, G.; Osadchii, D.; Ould-Chikh, S.; Ma, M.; Smith, W. A.; et al. Maximizing Ag Utilization in High-Rate CO2 Electrochemical Reduction with a Coordination Polymer-Mediated Gas Diffusion Electrode. *ACS Energy Lett.* **2019**, *4*, 2024−2031.
(161) Han, L.; Zhou, W.; Xiang, C. High-rate electrochemical reduction of carbon monoxide to ethylene using Cu-nanoparticle-based gas diffusion electrodes. *ACS Energy Letters* **2018**, *3* (4), 855−860.
(162) Wang, M.; Chen, L.; Lau, T. C.; Robert, M. A Hybrid Co Quaterpyridine Complex/Carbon Nanotube Catalytic Material for CO2 Reduction in Water. *Angew. Chem., Int. Ed.* **2018**, *57* (26), 7769−7773.
(163) Li, Q.; Rao, X.; Sheng, J.; Xu, J.; Yi, J.; Liu, Y.; Zhang, J. Energy storage through CO2 electroreduction: A brief review of advanced Sn-based electrocatalysts and electrodes. *Journal of CO2 Utilization* **2018**, *27*, 48−59.
(164) Albo, J.; Perfecto-Irigaray, M.; Beobide, G.; Irabien, A. Cu/Bi metal-organic framework-based systems for an enhanced electrochemical transformation of CO2 to alcohols. *Journal of CO2 Utilization* **2019**, *33*, 157−165.
(165) Lee, W.; Kim, Y. E.; Youn, M. H.; Jeong, S. K.; Park, K. T. Catholyte-Free Electrocatalytic CO2 Reduction to Formate. *Angew. Chem., Int. Ed.* **2018**, *57* (23), 6883−6887.
(166) Kim, B.; Hillman, F.; Ariyoshi, M.; Fujikawa, S.; Kenis, P. J. Effects of composition of the micro porous layer and the substrate on performance in the electrochemical reduction of CO2 to CO. *J. Power Sources* **2016**, *312*, 192−198.
(167) Irtem, E.; Hernández-Alonso, M. D.; Parra, A.; Fàbrega, C.; Penelas-Pérez, G.; Morante, J. R.; Andreu, T. A photoelectrochemical flow cell design for the efficient CO2 conversion to fuels. *Electrochim. Acta* **2017**, *240*, 225−230.
(168) Zhou, X.; Xiang, C. Comparative Analysis of Solar-to-Fuel Conversion Efficiency: A Direct, One-Step Electrochemical CO2 Reduction Reactor versus a Two-Step, Cascade Electrochemical CO2 Reduction Reactor. *ACS Energy Letters* **2018**, *3* (8), 1892−1897.
(169) Endrődi, B.; Kecsenovity, E.; Samu, A.; Darvas, F.; Jones, R. V.; Török, V.; Danyi, A.; Janáky, C. Multilayer Electrolyzer Stack Converts Carbon Dioxide to Gas Products at High Pressure with High Efficiency. *ACS energy letters* **2019**, *4* (7), 1770−1777.
(170) Zhang, H.; Ming, J.; Zhao, J.; Gu, Q.; Xu, C.; Ding, Z.; Yuan, R.; Zhang, Z.; Lin, H.; Wang, X.; et al. High-rate, tunable syngas production with artificial photosynthetic cells. *Angew. Chem., Int. Ed.* **2019**, *58* (23), 7718−7722.
(171) Kalamaras, E.; Belekoukia, M.; Tan, J. Z.; Xuan, J.; Maroto-Valer, M. M.; Andresen, J. M. A microfluidic photoelectrochemical cell for solar-driven CO2 conversion into liquid fuels with CuO-based photocathodes. *Faraday Discuss.* **2019**, *215*, 329−344.
(172) Luc, W.; Jouny, M.; Rosen, J.; Jiao, F. Carbon dioxide splitting using an electro-thermochemical hybrid looping strategy. *Energy Environ. Sci.* **2018**, *11* (10), 2928−2934.
(173) Banerjee, S.; Han, X.; Thoi, V. S. Modulating the Electrode-Electrolyte Interface with Cationic Surfactants in Carbon Dioxide Reduction. *ACS Catal.* **2019**, *9* (6), 5631−5637.

https://dx.doi.org/10.1021/acsenergylett.9b02585
ACS Energy Lett. 2020, 5, 486−519

(174) Zhu, W.; Kattel, S.; Jiao, F.; Chen, J. G. Shape-Controlled CO2 Electrochemical Reduction on Nanosized Pd Hydride Cubes and Octahedra. *Adv. Energy Mater.* **2019**, *9* (9), 1802840.
(175) Lee, J. H.; Kattel, S.; Xie, Z.; Tackett, B. M.; Wang, J.; Liu, C. J.; Chen, J. G. Understanding the role of functional groups in polymeric binder for electrochemical carbon dioxide reduction on gold nanoparticles. *Adv. Funct. Mater.* **2018**, *28* (45), 1804762.
(176) Dunwell, M.; Yang, X.; Setzler, B. P.; Anibal, J.; Yan, Y.; Xu, B. Examination of near-electrode concentration gradients and kinetic impacts on the electrochemical reduction of CO2 using surface-enhanced infrared spectroscopy. *ACS Catal.* **2018**, *8* (5), 3999−4008.
(177) Lee, W.-H.; Kang, J.; Park, H. S.; Nam, K. M.; Cho, S. K. Photoelectrochemical response of Au-decorated CuBi2O4 photocathode in bicarbonate solution. *J. Electroanal. Chem.* **2019**, *838*, 172−177.
(178) Zhong, H.; Fujii, K.; Nakano, Y. Effect of KHCO3 concentration on electrochemical reduction of CO2 on copper electrode. *J. Electrochem. Soc.* **2017**, *164* (9), F923−F927.
(179) Kim, J. H.; Magesh, G.; Kang, H. J.; Banu, M.; Kim, J. H.; Lee, J.; Lee, J. S. Carbonate-coordinated cobalt co-catalyzed BiVO4/WO3 composite photoanode tailored for CO2 reduction to fuels. *Nano Energy* **2015**, *15*, 153−163.
(180) Xia, Z.; Freeman, M.; Zhang, D.; Yang, B.; Lei, L.; Li, Z.; Hou, Y. Highly selective electrochemical conversion of CO2 to HCOOH on dendritic indium foams. *ChemElectroChem* **2018**, *5* (2), 253−259.
(181) Singh, M. R.; Goodpaster, J. D.; Weber, A. Z.; Head-Gordon, M.; Bell, A. T. Mechanistic insights into electrochemical reduction of CO2 over Ag using density functional theory and transport models. *Proc. Natl. Acad. Sci. U. S. A.* **2017**, *114* (42), E8812−E8821.
(182) Rohmann, K.; Kothe, J.; Haenel, M. W.; Englert, U.; Hölscher, M.; Leitner, W. Hydrogenation of CO2 to formic acid with a highly active ruthenium acriphos complex in DMSO and DMSO/water. *Angew. Chem., Int. Ed.* **2016**, *55* (31), 8966−8969.
(183) Angamuthu, R.; Byers, P.; Lutz, M.; Spek, A. L.; Bouwman, E. Electrocatalytic CO2 conversion to oxalate by a copper complex. *Science* **2010**, *327* (5963), 313−315.
(184) Figueiredo, M. C.; Ledezma-Yanez, I.; Koper, M. T. In situ spectroscopic study of CO2 electroreduction at copper electrodes in acetonitrile. *ACS Catal.* **2016**, *6* (4), 2382−2392.
(185) Rudnev, A. V.; Zhumaev, U. E.; Kuzume, A.; Vesztergom, S.; Furrer, J.; Broekmann, P.; Wandlowski, T. The promoting effect of water on the electroreduction of CO2 in acetonitrile. *Electrochim. Acta* **2016**, *189*, 38−44.
(186) Tamura, M.; Honda, M.; Nakagawa, Y.; Tomishige, K. Direct conversion of CO2 with diols, aminoalcohols and diamines to cyclic carbonates, cyclic carbamates and cyclic ureas using heterogeneous catalysts. *J. Chem. Technol. Biotechnol.* **2014**, *89* (1), 19−33.
(187) Rosen, B. A.; Salehi-Khojin, A.; Thorson, M. R.; Zhu, W.; Whipple, D. T.; Kenis, P. J.; Masel, R. I. Ionic liquid−mediated selective conversion of CO2 to CO at low overpotentials. *Science* **2011**, *334* (6056), 643−644.
(188) DiMeglio, J. L.; Rosenthal, J. Selective conversion of CO2 to CO with high efficiency using an inexpensive bismuth-based electrocatalyst. *J. Am. Chem. Soc.* **2013**, *135* (24), 8798−8801.
(189) Sun, L.; Ramesha, G. K.; Kamat, P. V.; Brennecke, J. F. Switching the reaction course of electrochemical CO2 reduction with ionic liquids. *Langmuir* **2014**, *30* (21), 6302−6308.
(190) Zhao, H.; Lu, B.; Li, X.; Zhang, W.; Zhao, J.; Cai, Q. Hydroxyl-functionalized ionic liquid for activation and conversion of CO2 and methanol into dimethyl carbonate. *Journal of CO2 Utilization* **2015**, *12*, 49−53.
(191) Hu, B.; Guild, C.; Suib, S. L. Thermal, electrochemical, and photochemical conversion of CO2 to fuels and value-added products. *Journal of CO2 Utilization* **2013**, *1*, 18−27.
(192) Zhou, Y.; Zhou, Z.; Song, Y.; Zhang, X.; Guan, F.; Lv, H.; Liu, Q.; Miao, S.; Wang, G.; Bao, X. Enhancing CO2 electrolysis performance with vanadium-doped perovskite cathode in solid oxide electrolysis cell. *Nano Energy* **2018**, *50*, 43−51.
(193) Yu, S.-B.; Lee, S.-H.; Mehran, M. T.; Hong, J.-E.; Lee, J.-W.; Lee, S.-B.; Park, S.-J.; Song, R.-H.; Shim, J.-H.; Shul, Y.-G.; et al. Syngas production in high performing tubular solid oxide cells by using high-temperature H2O/CO2 co-electrolysis. *Chem. Eng. J.* **2018**, *335*, 41−51.
(194) Mendieta-Reyes, N. s. E.; Cheuquepán, W.; Rodes, A.; Gómez, R. Spectroelectrochemical Study of CO2 Reduction on TiO2 Electrodes in Acetonitrile. *ACS Catal.* **2020**, *10*, 103−113.
(195) Chae, S. Y.; Choi, J. Y.; Kim, Y.; Nguyen, D. L. T.; Joo, O.-S. Photoelectrochemical CO2 reduction with a rhenium organometallic redox mediator at semiconductor/aqueous liquid junction interfaces. *Angew. Chem.* **2019**, *131* (46), 16547−16551.
(196) Jang, Y. J.; Jang, J.-W.; Lee, J.; Kim, J. H.; Kumagai, H.; Lee, J.; Minegishi, T.; Kubota, J.; Domen, K.; Lee, J. S. Selective CO production by Au coupled ZnTe/ZnO in the photoelectrochemical CO2 reduction system. *Energy Environ. Sci.* **2015**, *8* (12), 3597−3604.
(197) Zhang, M.; Cheng, J.; Xuan, X.; Zhou, J.; Cen, K. Pt/graphene aerogel deposited in Cu foam as a 3D binder-free cathode for CO2 reduction into liquid chemicals in a TiO2 photoanode-driven photoelectrochemical cell. *Chem. Eng. J.* **2017**, *322*, 22−32.
(198) de Brito, J. F.; Hudari, F. F.; Zanoni, M. V. B. Photoelectrocatalytic performance of nanostructured pn junction NtTiO2/NsCuO electrode in the selective conversion of CO2 to methanol at low bias potentials. *Journal of CO2 Utilization* **2018**, *24*, 81−88.
(199) Şahin, N. E.; Comminges, C.; Le Valant, A.; Kiener, J.; Parmentier, J.; Napporn, T. W.; Melinte, G.; Ersen, O.; Kokoh, K. B. One-Pot Soft-Template Synthesis of Nanostructured Copper-Supported Mesoporous Carbon FDU-15 Electrocatalysts for Efficient CO2 Reduction. *ChemPhysChem* **2018**, *19* (11), 1371−1381.
(200) Zhang, B.; Zhao, T.-J.; Feng, W.-J.; Liu, Y.-X.; Wang, H.-H.; Su, H.; Lv, L.-B.; Li, X.-H.; Chen, J.-S. Polarized few-layer gC 3 N 4 as metal-free electrocatalyst for highly efficient reduction of CO 2. *Nano Res.* **2018**, *11* (5), 2450−2459.
(201) Jang, J.; Jeon, B. W.; Kim, Y. H. Bioelectrochemical conversion of CO2 to value added product formate using engineered Methylobacterium extorquens. *Sci. Rep.* **2018**, *8* (1), 7211.
(202) Zheng, X.; Han, J.; Fu, Y.; Deng, Y.; Liu, Y.; Yang, Y.; Wang, T.; Zhang, L. Highly efficient CO2 reduction on ordered porous Cu electrode derived from Cu2O inverse opals. *Nano Energy* **2018**, *48*, 93−100.
(203) Kar, P.; Zeng, S.; Zhang, Y.; Vahidzadeh, E.; Manuel, A.; Kisslinger, R.; Alam, K. M.; Thakur, U. K.; Mahdi, N.; Kumar, P.; et al. High rate CO2 photoreduction using flame annealed TiO2 nanotubes. *Appl. Catal., B* **2019**, *243*, 522−536.
(204) Kormányos, A.; Ondok, R.; Janáky, C. Electrosynthesis and photoelectrochemical properties of polyaniline/SiC nanohybrid electrodes. *Electrochim. Acta* **2017**, *256*, 73−80.
(205) Jia, Y.; Xu, Y.; Nie, R.; Chen, F.; Zhu, Z.; Wang, J.; Jing, H. Artificial photosynthesis of methanol from carbon dioxide and water via a Nile red-embedded TiO 2 photocathode. *J. Mater. Chem. A* **2017**, *5* (11), 5495−5501.
(206) Liu, S.-S.; Xing, Q.-J.; Chen, Y.; Zhu, M.; Jiang, X.-H.; Wu, S.-H.; Dai, W.; Zou, J.-P. Photoelectrochemical Degradation of Organic Pollutants Using BiOBr Anode Coupled with Simultaneous CO2 Reduction to Liquid Fuels via CuO Cathode. *ACS Sustainable Chem. Eng.* **2019**, *7* (1), 1250−1259.
(207) Kang, U.; Choi, S. K.; Ham, D. J.; Ji, S. M.; Choi, W.; Han, D. S.; Abdel-Wahab, A.; Park, H. Photosynthesis of formate from CO 2 and water at 1% energy efficiency via copper iron oxide catalysis. *Energy Environ. Sci.* **2015**, *8* (9), 2638−2643.
(208) Xiong, J.; Di, J.; Li, H. Atomically Thin 2D Multinary Nanosheets for Energy-Related Photo, Electrocatalysis. *Advanced Science* **2018**, *5* (7), 1800244.
(209) Hori, Y.; Wakebe, H.; Tsukamoto, T.; Koga, O. Electrocatalytic process of CO selectivity in electrochemical reduction of CO2 at metal electrodes in aqueous media. *Electrochim. Acta* **1994**, *39* (11−12), 1833−1839.
(210) Kortlever, R.; Shen, J.; Schouten, K. J. P.; Calle-Vallejo, F.; Koper, M. T. M. Catalysts and reaction pathways for the

electrochemical reduction of carbon dioxide. *J. Phys. Chem. Lett.* **2015**, *6* (20), 4073−4082.
(211) de Brito, J. F.; Araujo, A. R.; Rajeshwar, K.; Zanoni, M. V. B. Photoelectrochemical reduction of CO2 on Cu/Cu2O films: Product distribution and pH effects. *Chem. Eng. J.* **2015**, *264*, 302−309.
(212) Dunwell, M.; Lu, Q.; Heyes, J. M.; Rosen, J.; Chen, J. G.; Yan, Y.; Jiao, F.; Xu, B. The central role of bicarbonate in the electrochemical reduction of carbon dioxide on gold. *J. Am. Chem. Soc.* **2017**, *139* (10), 3774−3783.
(213) Luo, X.; Xuan, J.; Fernandez, E. S.; Maroto-Valer, M. M. Modeling and simulation for photoelectrochemical CO2 utilization. *Energy Procedia* **2019**, *158*, 809−815.
(214) Bernadet, S.; Tavernier, E.; Ta, D. M.; Vallée, R. A.; Ravaine, S.; Fécant, A.; Backov, R. Bulk Photodriven CO2 Conversion through TiO2@ Si (HIPE) Monolithic Macrocellular Foams. *Adv. Funct. Mater.* **2019**, *29* (9), 1807767.
(215) Durst, J.; Siebel, A.; Simon, C.; Hasche, F.; Herranz, J.; Gasteiger, H. New insights into the electrochemical hydrogen oxidation and evolution reaction mechanism. *Energy Environ. Sci.* **2014**, *7* (7), 2255−2260.
(216) Li, C. W.; Kanan, M. W. CO2 reduction at low overpotential on Cu electrodes resulting from the reduction of thick Cu2O films. *J. Am. Chem. Soc.* **2012**, *134* (17), 7231−7234.
(217) Wang, Q.; Wang, X.; Yu, Z.; Jiang, X.; Chen, J.; Tao, L.; Wang, M.; Shen, Y. Artificial photosynthesis of ethanol using type-II g-C3N4/ZnTe heterojunction in photoelectrochemical CO2 reduction system. *Nano Energy* **2019**, *60*, 827−835.
(218) Zheng, J.; Li, X.; Qin, Y.; Zhang, S.; Sun, M.; Duan, X.; Sun, H.; Li, P.; Wang, S. Zn phthalocyanine/carbon nitride heterojunction for visible light photoelectrocatalytic conversion of CO2 to methanol. *J. Catal.* **2019**, *371*, 214−223.
(219) Lee, K.; Lee, S.; Cho, H.; Jeong, S.; Kim, W. D.; Lee, S.; Lee, D. C. Cu+-incorporated TiO2 overlayer on Cu2O nanowire photocathodes for enhanced photoelectrochemical conversion of CO2 to methanol. *J. Energy Chem.* **2018**, *27* (1), 264−270.
(220) Cheng, J.; Xuan, X.; Yang, X.; Zhou, J.; Cen, K. Selective reduction of CO2 to alcohol products on octahedral catalyst of carbonized Cu (BTC) doped with Pd nanoparticles in a photo-electrochemical cell. *Chem. Eng. J.* **2019**, *358*, 860−868.
(221) Zhang, C.; Hwang, S. Y.; Trout, A.; Peng, Z. Solid-state chemistry-enabled scalable production of octahedral Pt−Ni alloy electrocatalyst for oxygen reduction reaction. *J. Am. Chem. Soc.* **2014**, *136* (22), 7805−7808.
(222) Cai, C.; Xu, Y.-F.; Chen, H.-Y.; Wang, X.-D.; Kuang, D.-B. Porous ZnO@ ZnSe nanosheet array for photoelectrochemical reduction of CO2. *Electrochim. Acta* **2018**, *274*, 298−305.
(223) Cho, H.; Kim, W. D.; Lee, K.; Lee, S.; Kang, G.-S.; Joh, H.-I.; Lee, D. C. Selectivity of photoelectrochemical CO2 reduction modulated with electron transfer from size-tunable quantized energy states of CdSe nanocrystals. *Appl. Surf. Sci.* **2018**, *429*, 2−8.
(224) Zhu, H.; Yang, Y.; Hyeon-Deuk, K.; Califano, M.; Song, N.; Wang, Y.; Zhang, W.; Prezhdo, O. V.; Lian, T. Auger-assisted electron transfer from photoexcited semiconductor quantum dots. *Nano Lett.* **2014**, *14* (3), 1263−1269.
(225) Kamata, R.; Kumagai, H.; Yamazaki, Y.; Sahara, G.; Ishitani, O. Photoelectrochemical CO2 Reduction Using a Ru (II)−Re (I) Supramolecular Photocatalyst Connected to a Vinyl Polymer on a NiO Electrode. *ACS Appl. Mater. Interfaces* **2019**, *11* (6), 5632−5641.
(226) Fu, Q.; Xiao, S.; Li, Z.; Li, Y.; Kobayashi, H.; Li, J.; Yang, Y.; Liao, Q.; Zhu, X.; He, X.; et al. Hybrid solar-to-methane conversion system with a Faradaic efficiency of up to 96%. *Nano Energy* **2018**, *53*, 232−239.
(227) Kuk, S. K.; Ham, Y.; Gopinath, K.; Boonmongkolras, P.; Lee, Y.; Lee, Y. W.; Kondaveeti, S.; Ahn, C.; Shin, B.; Lee, J. K.; et al. Continuous 3D Titanium Nitride Nanoshell Structure for Solar-Driven Unbiased Biocatalytic CO2 Reduction. *Adv. Energy Mater.* **2019**, *9* (25), 1900029.
(228) Lee, S. Y.; Lim, S. Y.; Seo, D.; Lee, J. Y.; Chung, T. D. Light-Driven Highly Selective Conversion of CO2 to Formate by Electrosynthesized Enzyme/Cofactor Thin Film Electrode. *Adv. Energy Mater.* **2016**, *6* (11), 1502207.
(229) Jin, H.; Guo, C.; Liu, X.; Liu, J.; Vasileff, A.; Jiao, Y.; Zheng, Y.; Qiao, S.-Z. Emerging two-dimensional nanomaterials for electrocatalysis. *Chem. Rev.* **2018**, *118* (13), 6337−6408.
(230) Gurudayal, G.; Beeman, J. W.; Bullock, J.; Wang, H.; Eichhorn, J.; Towle, C.; Javey, A.; Toma, F. M.; Mathews, N.; Ager, J. W. Si photocathode with Ag-supported dendritic Cu catalyst for CO2 reduction. *Energy Environ. Sci.* **2019**, *12* (3), 1068−1077.
(231) Hasani, A.; Tekalgne, M.; Van Le, Q.; Jang, H. W.; Kim, S. Y. Two-dimensional materials as catalysts for solar fuels: hydrogen evolution reaction and CO2 reduction. *J. Mater. Chem. A* **2019**, *7* (2), 430−454.
(232) Tian, Y.; Wang, Y.; Yan, L.; Zhao, J.; Su, Z. Electrochemical reduction of carbon dioxide on the two−dimensional M3 (Hexaiminotriphenylene) 2 sheet: A computational study. *Appl. Surf. Sci.* **2019**, *467*, 98−103.
(233) Yang, X.; Wang, D. Photocatalysis: from fundamental principles to materials and applications. *ACS Applied Energy Materials* **2018**, *1* (12), 6657−6693.
(234) Chia, X.; Pumera, M. Characteristics and performance of two-dimensional materials for electrocatalysis. *Nature Catalysis* **2018**, *1*, 909−921.
(235) Bi, W.; Wu, C.; Xie, Y. Atomically thin two-dimensional solids: an emerging platform for CO2 electroreduction. *ACS Energy Letters* **2018**, *3* (3), 624−633.
(236) Zhang, J.; Zhang, Y.; Li, L.; Guo, S.-X.; Zhang, X.; Li, F.; Bond, A. M. Two-Dimensional Electrocatalysts for Efficient Reduction of CO2. *ChemSusChem* **2020**, *13*, 59.
(237) Medina-Ramos, J.; Pupillo, R. C.; Keane, T. P.; DiMeglio, J. L.; Rosenthal, J. Efficient conversion of CO2 to CO using tin and other inexpensive and easily prepared post-transition metal catalysts. *J. Am. Chem. Soc.* **2015**, *137* (15), 5021−5027.
(238) Detweiler, Z. M.; White, J. L.; Bernasek, S. L.; Bocarsly, A. B. Anodized indium metal electrodes for enhanced carbon dioxide reduction in aqueous electrolyte. *Langmuir* **2014**, *30* (25), 7593−7600.
(239) Liu, S.; Tao, H.; Zeng, L.; Liu, Q.; Xu, Z.; Liu, Q.; Luo, J.-L. Shape-dependent electrocatalytic reduction of CO2 to CO on triangular silver nanoplates. *J. Am. Chem. Soc.* **2017**, *139* (6), 2160−2163.
(240) Urbain, F. l.; Tang, P.; Carretero, N. M.; Andreu, T.; Arbiol, J.; Morante, J. R. Tailoring Copper Foam with Silver Dendrite Catalysts for Highly Selective Carbon Dioxide Conversion into Carbon Monoxide. *ACS Appl. Mater. Interfaces* **2018**, *10* (50), 43650−43660.
(241) Zhao, S.; Jin, R.; Jin, R. Opportunities and challenges in CO2 reduction by gold-and silver-based electrocatalysts: from bulk metals to nanoparticles and atomically precise nanoclusters. *ACS Energy Letters* **2018**, *3* (2), 452−462.
(242) Luc, W.; Fu, X.; Shi, J.; Lv, J.-J.; Jouny, M.; Ko, B. H.; Xu, Y.; Tu, Q.; Hu, X.; Wu, J.; et al. Two-dimensional copper nanosheets for electrochemical reduction of carbon monoxide to acetate. *Nature Catalysis* **2019**, *2* (5), 423.
(243) Xiong, J.; Di, J.; Xia, J.; Zhu, W.; Li, H. Surface defect engineering in 2D nanomaterials for photocatalysis. *Adv. Funct. Mater.* **2018**, *28* (39), 1801983.
(244) Voiry, D.; Shin, H.; Loh, K.; Chhowalla, M. Low-dimensional catalysts for hydrogen evolution and CO2 reduction. *Nature Reviews Chemistry* **2018**, *2*, 0105.
(245) Li, F.; Chen, L.; Knowles, G. P.; MacFarlane, D. R.; Zhang, J. Hierarchical mesoporous SnO2 nanosheets on carbon cloth: a robust and flexible electrocatalyst for CO2 reduction with high efficiency and selectivity. *Angew. Chem., Int. Ed.* **2017**, *56* (2), 505−509.
(246) An, X.; Li, K.; Tang, J. Cu2O/reduced graphene oxide composites for the photocatalytic conversion of CO2. *ChemSusChem* **2014**, *7* (4), 1086−1093.

(247) Sun, Y.; Lei, F.; Gao, S.; Pan, B.; Zhou, J.; Xie, Y. Atomically thin tin dioxide sheets for efficient catalytic oxidation of carbon monoxide. *Angew. Chem., Int. Ed.* **2013**, *52* (40), 10569−10572.
(248) Wang, L.; Wang, L.; Zhang, J.; Liu, X.; Wang, H.; Zhang, W.; Yang, Q.; Ma, J.; Dong, X.; Yoo, S. J.; et al. Selective hydrogenation of CO2 to ethanol over cobalt catalysts. *Angew. Chem., Int. Ed.* **2018**, *57* (21), 6104−6108.
(249) Hussein, A.; Burra, K.; Bassioni, G.; Hammouda, R.; Gupta, A. Production of CO from CO2 over mixed-metal oxides derived from layered-double-hydroxides. *Appl. Energy* **2019**, *235*, 1183−1191.
(250) Iguchi, S.; Kikkawa, S.; Teramura, K.; Hosokawa, S.; Tanaka, T. Investigation of the electrochemical and photoelectrochemical properties of Ni−Al LDH photocatalysts. *Phys. Chem. Chem. Phys.* **2016**, *18* (20), 13811−13819.
(251) Yoshitomi, F.; Sekizawa, K.; Maeda, K.; Ishitani, O. Selective formic acid production via CO2 reduction with visible light using a hybrid of a perovskite tantalum oxynitride and a binuclear ruthenium (II) complex. *ACS Appl. Mater. Interfaces* **2015**, *7* (23), 13092−13097.
(252) Hafez, A. M.; Zedan, A. F.; AlQaradawi, S. Y.; Salem, N. M.; Allam, N. K. Computational study on oxynitride perovskites for CO2 photoreduction. *Energy Convers. Manage.* **2016**, *122*, 207−214.
(253) Hou, J.; Cao, S.; Wu, Y.; Gao, Z.; Liang, F.; Sun, Y.; Lin, Z.; Sun, L. Inorganic colloidal perovskite quantum dots for robust solar CO2 reduction. *Chem. - Eur. J.* **2017**, *23* (40), 9481−9485.
(254) Kang, S.; Han, S.; Kang, Y. Unveiling Electrochemical Reaction Pathways of CO2 Reduction to CN Species at S-Vacancies of MoS2. *ChemSusChem* **2019**, *12* (12), 2671−2678.
(255) Lv, K.; Teng, C.; Shi, M.; Yuan, Y.; Zhu, Y.; Wang, J.; Kong, Z.; Lu, X.; et al. Hydrophobic and Electronic Properties of the E-MoS2 Nanosheets Induced by FAS for the CO2 Electroreduction to Syngas with a Wide Range of CO/H2 Ratios. *Adv. Funct. Mater.* **2018**, *28* (49), 1802339.
(256) Lv, K.; Suo, W.; Shao, M.; Zhu, Y.; Wang, X.; Feng, J.; Fang, M.; et al. Nitrogen doped MoS2 and nitrogen doped carbon dots composite catalyst for electroreduction CO2 to CO with high Faradaic efficiency. *Nano Energy* **2019**, *63*, 103834.
(257) Hu, X.; Yang, H.; Gao, M.; Tian, H.; Li, Y.; Liang, Z.; Jian, X. Insights into the Photoassisted Electrocatalytic Reduction of CO2 over a Two-dimensional MoS2 Nanostructure Loaded on SnO2 Nanoparticles. *ChemElectroChem* **2019**, *6* (12), 3077−3084.
(258) Handoko, A. D.; Khoo, K. H.; Tan, T. L.; Jin, H.; Seh, Z. W. Establishing new scaling relations on two-dimensional MXenes for CO 2 electroreduction. *J. Mater. Chem. A* **2018**, *6* (44), 21885−21890.
(259) Li, N.; Chen, X.; Ong, W.-J.; MacFarlane, D. R.; Zhao, X.; Cheetham, A. K.; Sun, C. Understanding of electrochemical mechanisms for CO2 capture and conversion into hydrocarbon fuels in transition-metal carbides (MXenes). *ACS Nano* **2017**, *11* (11), 10825−10833.
(260) Zhang, C.; Yang, S.; Wu, J.; Liu, M.; Yazdi, S.; Ren, M.; Sha, J.; Zhong, J.; Nie, K.; Jalilov, A. S.; et al. Electrochemical CO2 Reduction with Atomic Iron-Dispersed on Nitrogen-Doped Graphene. *Adv. Energy Mater.* **2018**, *8* (19), 1703487.
(261) Xu, Y.; Wang, S.; Yang, J.; Han, B.; Nie, R.; Wang, J.; Dong, Y.; Yu, X.; Wang, J.; Jing, H. Highly efficient photoelectrocatalytic reduction of CO 2 on the Ti 3 C 2/gC 3 N 4 heterojunction with rich Ti 3+ and pyri-N species. *J. Mater. Chem. A* **2018**, *6* (31), 15213−15220.
(262) Hu, X.-M.; Hval, H. H.; Bjerglund, E. T.; Dalgaard, K. J.; Madsen, M. R.; Pohl, M.-M.; Welter, E.; Lamagni, P.; Buhl, K. B.; Bremholm, M. Selective CO2 Reduction to CO in water using earth-abundant metal and nitrogen-doped carbon electrocatalysts. *ACS Catal.* **2018**, *8* (7), 6255−6264.
(263) Cardoso, J.; Stulp, S.; de Brito, J.; Flor, J.; Frem, R.; Zanoni, M. MOFs based on ZIF-8 deposited on TiO2 nanotubes increase the surface adsorption of CO2 and its photoelectrocatalytic reduction to alcohols in aqueous media. *Appl. Catal., B* **2018**, *225*, 563−573.
(264) Maina, J. W.; Pozo-Gonzalo, C.; Schütz, J. A.; Wang, J.; Dumée, L. F. Tuning CO2 conversion product selectivity of metal organic frameworks derived hybrid carbon photoelectrocatalytic reactors. *Carbon* **2019**, *148*, 80−90.
(265) Cheng, J.; Xuan, X.; Yang, X.; Zhou, J.; Cen, K. Preparation of a Cu (BTC)-rGO catalyst loaded on a Pt deposited Cu foam cathode to reduce CO 2 in a photoelectrochemical cell. *RSC Adv.* **2018**, *8* (56), 32296−32303.
(266) Rosen, B. A.; Hod, I. Tunable Molecular-Scale Materials for Catalyzing the Low-Overpotential Electrochemical Conversion of CO2. *Adv. Mater.* **2018**, *30* (41), 1706238.
(267) Gu, J.; Hsu, C.-S.; Bai, L.; Chen, H. M.; Hu, X. Atomically dispersed Fe3+ sites catalyze efficient CO2 electroreduction to CO. *Science* **2019**, *364* (6445), 1091−1094.
(268) Cho, M.; Song, J. T.; Back, S.; Jung, Y.; Oh, J. The Role of Adsorbed CN and Cl on an Au Electrode for Electrochemical CO2 Reduction. *ACS Catal.* **2018**, *8* (2), 1178−1185.
(269) Han, Y.; Xu, H.; Su, Y.; Xu, Z.-l.; Wang, K.; Wang, W. Noble metal (Pt, Au@ Pd) nanoparticles supported on metal organic framework (MOF-74) nanoshuttles as high-selectivity CO2 conversion catalysts. *J. Catal.* **2019**, *370*, 70−78.
(270) Garza, A. J.; Bell, A. T.; Head-Gordon, M. Mechanism of CO2 reduction at copper surfaces: Pathways to C2 products. *ACS Catal.* **2018**, *8* (2), 1490−1499.
(271) Rasul, S.; Anjum, D. H.; Jedidi, A.; Minenkov, Y.; Cavallo, L.; Takanabe, K. A highly selective copper−indium bimetallic electrocatalyst for the electrochemical reduction of aqueous CO2 to CO. *Angew. Chem., Int. Ed.* **2015**, *54* (7), 2146−2150.
(272) Zhu, W.; Michalsky, R.; Metin, O. n.; Lv, H.; Guo, S.; Wright, C. J.; Sun, X.; Peterson, A. A.; Sun, S. Monodisperse Au nanoparticles for selective electrocatalytic reduction of CO2 to CO. *J. Am. Chem. Soc.* **2013**, *135* (45), 16833−16836.
(273) Sarfraz, S.; Garcia-Esparza, A. T.; Jedidi, A.; Cavallo, L.; Takanabe, K. Cu−Sn bimetallic catalyst for selective aqueous electroreduction of CO2 to CO. *ACS Catal.* **2016**, *6* (5), 2842−2851.
(274) Tao, H.; Gao, Y.; Talreja, N.; Guo, F.; Texter, J.; Yan, C.; Sun, Z. Two-dimensional nanosheets for electrocatalysis in energy generation and conversion. *J. Mater. Chem. A* **2017**, *5* (16), 7257−7284.
(275) García de Arquer, F. P.; Bushuyev, O. S.; De Luna, P.; Dinh, C. T.; Seifitokaldani, A.; Saidaminov, M. I.; Tan, C. S.; Quan, L. N.; Proppe, A.; Kibria, M. G.; et al. 2D Metal Oxyhalide-Derived Catalysts for Efficient CO2 Electroreduction. *Adv. Mater.* **2018**, *30* (38), 1802858.
(276) Hu, G.; Wu, Z.; Dai, S.; Jiang, D.-e. Interface Engineering of Earth-Abundant Transition Metals Using Boron Nitride for Selective Electroreduction of CO2. *ACS Appl. Mater. Interfaces* **2018**, *10* (7), 6694−6700.
(277) Laskowski, R.; Blaha, P.; Schwarz, K. Bonding of hexagonal BN to transition metal surfaces: An ab initio density-functional theory study. *Phys. Rev. B: Condens. Matter Mater. Phys.* **2008**, *78* (4), 045409.
(278) Gomez Diaz, J.; Ding, Y.; Koitz, R.; Seitsonen, A. P.; Iannuzzi, M.; Hutter, J. Hexagonal boron nitride on transition metal surfaces. *Theor. Chem. Acc.* **2013**, *132* (4), 1350.
(279) Legrand, U.; Boudreault, R.; Meunier, J. Decoration of N-functionalized graphene nanoflakes with copper-based nanoparticles for high selectivity CO2 electroreduction towards formate. *Electrochim. Acta* **2019**, *318*, 142−150.
(280) Geioushy, R.; Khaled, M. M.; Alhooshani, K.; Hakeem, A. S.; Rinaldi, A. Graphene/ZnO/Cu2O electrocatalyst for selective conversion of CO2 into n-propanol. *Electrochim. Acta* **2017**, *245*, 456−462.
(281) Hu, C.; Mu, Y.; Bai, S.; Yang, J.; Gao, L.; Cheng, S.-D.; Mi, S.-B.; Qiu, J. Polyvinyl pyrrolidone mediated fabrication of Fe, N-codoped porous carbon sheets for efficient electrocatalytic CO2 reduction. *Carbon* **2019**, *153*, 609−616.
(282) Xu, Y.; Wang, S.; Yang, J.; Han, B.; Nie, R.; Wang, J.; Wang, J.; Jing, H. In-situ grown nanocrystal TiO2 on 2D Ti3C2 nanosheets for

artificial photosynthesis of chemical fuels. *Nano Energy* **2018**, *51*, 442−450.
(283) Pan, Y.; Lin, R.; Chen, Y.; Liu, S.; Zhu, W.; Cao, X.; Chen, W.; Wu, K.; Cheong, W.-C.; Wang, Y.; et al. Design of single-atom Co−N5 catalytic site: a robust electrocatalyst for CO2 reduction with nearly 100% CO selectivity and remarkable stability. *J. Am. Chem. Soc.* **2018**, *140* (12), 4218−4221.
(284) Liu, J.; Qiao, S. Z.; Liu, H.; Chen, J.; Orpe, A.; Zhao, D.; Lu, G. Q. Extension of the Stöber method to the preparation of monodisperse resorcinol−formaldehyde resin polymer and carbon spheres. *Angew. Chem., Int. Ed.* **2011**, *50* (26), 5947−5951.
(285) Nørskov, J. K.; Rossmeisl, J.; Logadottir, A.; Lindqvist, L.; Kitchin, J. R.; Bligaard, T.; Jonsson, H. Origin of the overpotential for oxygen reduction at a fuel-cell cathode. *J. Phys. Chem. B* **2004**, *108* (46), 17886−17892.
(286) Hammer, B.; Norskov, J. K. Why gold is the noblest of all the metals. *Nature* **1995**, *376* (6537), 238.
(287) Wu, J.; Liu, M.; Sharma, P. P.; Yadav, R. M.; Ma, L.; Yang, Y.; Zou, X.; Zhou, X.-D.; Vajtai, R.; Yakobson, B. I.; et al. Incorporation of nitrogen defects for efficient reduction of CO2 via two-electron pathway on three-dimensional graphene foam. *Nano Lett.* **2016**, *16* (1), 466−470.
(288) Shinde, D. V.; Lim, I.; Lee, J.-K.; Sung, M. M.; Mane, R. S.; Han, S.-H. Photoelectrochemical cells by design: 3D nanoporous CdO−CdSe architectures on ITO. *J. Mater. Chem. A* **2013**, *1* (35), 10436−10441.
(289) Khatavkar, S. N.; Ukale, D. U.; Haram, S. K. Development of self-supported 3D microporous solder alloy electrodes for scalable CO 2 electroreduction to formate. *New J. Chem.* **2019**, *43* (17), 6587−6596.
(290) Luo, W.; Xie, W.; Li, M.; Zhang, J.; Züttel, A. 3D hierarchical porous indium catalyst for highly efficient electroreduction of CO 2. *J. Mater. Chem. A* **2019**, *7* (9), 4505−4515.
(291) Zou, J.-P.; Chen, Y.; Liu, S.-S.; Xing, Q.-J.; Dong, W.-H.; Luo, X.-B.; Dai, W.-L.; Xiao, X.; Luo, J.-M.; Crittenden, J. Electrochemical oxidation and advanced oxidation processes using a 3D hexagonal Co3O4 array anode for 4-nitrophenol decomposition coupled with simultaneous CO2 conversion to liquid fuels via a flower-like CuO cathode. *Water Res.* **2019**, *150*, 330−339.
(292) Jung, H.; Cho, K. M.; Kim, K. H.; Yoo, H.-W.; Al-Saggaf, A.; Gereige, I.; Jung, H.-T. Highly efficient and stable CO2 reduction photocatalyst with a hierarchical structure of mesoporous TiO2 on 3D graphene with few-layered MoS2. *ACS Sustainable Chem. Eng.* **2018**, *6* (5), 5718−5724.
(293) Raciti, D.; Wang, Y.; Park, J. H.; Wang, C. Three-Dimensional Hierarchical Copper-Based Nanostructures as Advanced Electrocatalysts for CO2 Reduction. *ACS Applied Energy Materials* **2018**, *1* (6), 2392−2398.
(294) Chen, L.; Tang, X.; Xie, P.; Xu, J.; Chen, Z.; Cai, Z.; He, P.; Zhou, H.; Zhang, D.; Fan, T. 3D printing of artificial leaf with tunable hierarchical porosity for CO2 photoreduction. *Chem. Mater.* **2018**, *30* (3), 799−806.
(295) Zhu, C.; Qi, Z.; Beck, V. A.; Luneau, M.; Lattimer, J.; Chen, W.; Worsley, M. A.; Ye, J.; Duoss, E. B.; Spadaccini, C. M.; et al. Toward digitally controlled catalyst architectures: Hierarchical nanoporous gold via 3D printing. *Science advances* **2018**, *4* (8), No. eaas9459.
(296) Lai, J.; Nsabimana, A.; Luque, R.; Xu, G. 3D porous carbonaceous electrodes for electrocatalytic applications. *Joule* **2018**, *2* (1), 76−93.
(297) Yousefi, N.; Lu, X.; Elimelech, M.; Tufenkji, N. Environmental performance of graphene-based 3D macrostructures. *Nat. Nanotechnol.* **2019**, *14*, 107−119.
(298) Cheng, Y.; Zhao, S.; Li, H.; He, S.; Veder, J.-P.; Johannessen, B.; Xiao, J.; Lu, S.; Pan, J.; Chisholm, M. F. Unsaturated edge-anchored Ni single atoms on porous microwave exfoliated graphene oxide for electrochemical CO2. *Appl. Catal., B* **2019**, *243*, 294−303.
(299) Hou, X.; Cai, Y.; Zhang, D.; Li, L.; Zhang, X.; Zhu, Z.; Peng, L.; Liu, Y.; Qiao, J. 3D core−shell porous-structured Cu@ Sn hybrid electrodes with unprecedented selective CO 2-into-formate electroreduction achieving 100%. *J. Mater. Chem. A* **2019**, *7* (7), 3197−3205.
(300) Kas, R.; Ayemoba, O.; Firet, N. J.; Middelkoop, J.; Smith, W. A.; Cuesta, A. In-situ infrared spectroscopy applied to the study of the electrocatalytic reduction of CO2: Theory, practice and challenges. *ChemPhysChem* **2019**, *20* (22), 2904−2925.
(301) Bushuyev, O. S.; De Luna, P.; Dinh, C. T.; Tao, L.; Saur, G.; van de Lagemaat, J.; Kelley, S. O.; Sargent, E. H. What should we make with CO2 and how can we make it? *Joule* **2018**, *2* (5), 825−832.
(302) Herron, J. A.; Kim, J.; Upadhye, A. A.; Huber, G. W.; Maravelias, C. T. A general framework for the assessment of solar fuel technologies. *Energy Environ. Sci.* **2015**, *8* (1), 126−157.
(303) Ulmer, U.; Dingle, T.; Duchesne, P. N.; Morris, R. H.; Tavasoli, A.; Wood, T.; Ozin, G. A. Fundamentals and applications of photocatalytic CO2 methanation. *Nat. Commun.* **2019**, *10* (1), 1−12.
(304) Pettinau, A.; Mureddu, M.; Ferrara, F. Carbon dioxide conversion into liquid fuels by hydrogenation and photoelectrochemical reduction: Project description and preliminary experimental results. *Energy Procedia* **2017**, *114*, 6893−6904.

https://dx.doi.org/10.1021/acsenergylett.9b02585
ACS Energy Lett. 2020, 5, 486−519